PROBING THE INTERACTION BETWEEN NANOPARTICLES AND LIPID VESICLES

by

ANUPAMA BHAT

A DISSERTATION

Submitted in partial fulfillment of the requirements
for the degree of Doctor of Philosophy in the
Optics Graduate Program of
Delaware State University

DOVER, DELAWARE

May 2018

This dissertation is approved by the following members of the Final Oral Review Committee:

Dr. Qi Lu, Committee Chairperson, Department of Physics & Engineering, Delaware State University
Dr. Hacene Boukari, Committee Member, Department of Physics & Engineering, Delaware State University
Dr. Jun Ren, Committee Member, Department of Physics & Engineering, Delaware State University
Dr. Murali Temburni, Committee Member, Department of Biological Sciences, Delaware State University
Dr. Robin Helburn, External Committee Member, Department of Physics & Chemistry, St. Francis College, Brooklyn Heights, NY

DEDICATION

The process of scientific discovery is, in effect, a continual flight from wonder

- ***Albert Einstein***

I dedicate this dissertation to my beloved parents

Madhukar Bhat and Rupa Bhat

ACKNOWLEDGEMENTS

First, I wish to thank my advisor, Dr. Qi Lu for the valuable guidance, scholarly inputs and consistent encouragement I received throughout the research work. It has been an honor to be her first Ph.D. student. I appreciate all her contributions of time, ideas and funding to make my Ph.D. experience productive and stimulating. The joy and enthusiasm she has for her research was contagious and motivational for me. She helped me come up with the dissertation topic and guided me over almost a year of development. Moreover, during the most difficult times when writing this dissertation, she gave me the moral support and the freedom I needed to move on. Despite her busy schedule, her door was always open for discussion. I learned how to be an effective and independent researcher from our regular meetings. I am also thankful for the excellent example she has provided as a successful professor in biophysics.

I would like to thank my committee members, Dr. Hacene Boukari, Dr. Jun Ren, Dr. Murali Temburni and Dr. Robin Helburn for their time, attention, and insightful comments regarding my dissertation.

I consider myself very fortunate to have been a part of the bio-nano research group, and would like to thank all of my past and current lab members for the encouraging discussions while working together. Thank you May Hnin Hlaing, your unconditional constant support has been essential all these years.

The time I spent at Delaware State University was enriched in large part by the academic staff, postdocs, graduates, and undergraduates in the Physics and Engineering department. I would like to extend my sincere gratitude to all the professors of the Optics program at Delaware State University who provided me with the necessary background in physics and optics.

I would like to thank my family for all their love and encouragement. Thank you, Ajay, for your support and encouragement during the final stages of this Ph.D. A special thanks to my son Abhishek for cheering me on throughout the doctorate degree.

I gratefully acknowledge the funding sources that made my Ph.D. work possible. I was funded by grants from the National Institute of General Medical Sciences (2P20 GM103446-14) from the National Institutes of Health and CREST grant #1242067 from National Science Foundation.

I also acknowledge the OSCAR Imaging Facility at Delaware State University, which is part of the Delaware Core Facilities Network, for the access of instruments.

Probing the Interaction between Nanoparticles and Lipid Vesicles

Anupama Bhat

Faculty Advisor: Dr. Qi Lu

ABSTRACT

Ability to grow nanomaterials in different sizes, shapes and functionalities with exceptional control has catalyzed significant advances in nanomedicine, diagnosis and treatment of diseases. The interaction of nanoparticles (NPs) with cell membranes effectively alters certain physical properties such as fluidity, elasticity, flexibility, and permeability of cell membranes. Herein, we constructed various vesicle systems using dimyristoyl phosphatidylcholine (DMPC), a zwitterionic phospholipid molecule widely used for model cell membranes. In some experiments, DMPC vesicles were doped with cholesterol to modulate the membrane integrity. Vesicles were then treated with colloidal gold or silver nanoparticles (AuNPs/AgNPs) at various sizes and concentrations for further examination and analysis with fluorescence spectroscopy, fluorescence microscopy, atomic force microscopy (AFM), as well as hyperspectral dark-field microscopy. Our data suggest that AuNPs cause localized stiffening in the membranes whereas fluidization in the long range. AuNPs were found to interact with vesicles in a different way than AgNPs do. What we learned in this work provides better understanding on the mechanisms of AuNP/AgNP and membrane interactions for their respective future applications in nanomedicine and nanotechnology.

Table of Contents

LIST OF TABLES

LIST OF FIGURES AND ILLUSTRATIONS

LIST OF ACRONYMS

Acronyms	Definition
AFM	Atomic Force Microscopy
AgNP	Silver Nanoparticle
AuNP	Gold nanoparticle
BSA	Bovine Serum Albumin
CCD	Charge coupled device
DMPC	1,2-dimyristoyl-sn-glycero-3-phosphocholine
ENVI	Environment for Visualizing Images
FCS	Fluorescence Correlation Spectroscopy
FRET	Forster Resonance Energy Transfer
FWHM	Full-Width at Half Maximum
GP	Generalized Polarization
GUV	Giant Unilamellar Vesicles
HSI	Hyperspectral imaging
IR	Infra-red
ISC	Inter System Crossing
ITO	Indium Tin Oxide
LMV	Large Multilamellar Vesicles
LUV	Large Unilamellar Vesicles
NIR	Near infra-red
NP	Nanoparticle
PBS	Phosphate buffered saline

(Continued)

PC	Protein Corona
PF-QNM	Peak Force Quantitative Nanomechanical
PMT	Photon multiplier tube
PSPD	Position-sensitive photo diode
SNR	Signal-to-Noise ratio
SPR	Surface Plasmon Resonance
SS	Steady-state
SUV	Small Unilamellar Vesicles
SWIR	Short wave infrared
UV	Ultra-violet
VIS	Visible
VNIR	Visible near infrared

CHAPTER I

INTRODUCTION

1.1 Overview of interactions between nanoparticles and cell membrane

Nanoparticles (NPs) have been increasingly integrated in biological systems, making it imperative to understand their interactions with cell membranes, the first barriers to be crossed to enter cells [1]. The size resemblance of nanoparticles to biological macromolecules coupled with the NPs' high surface energy leads to intricate interactions between the two entities. Myriads of study have been conducted to gain insights into the bio-nano interface for biomedical applications such as cancer therapy, targeted drug delivery and bio imaging [2]. The interaction with nanosized materials effectively alters membrane properties such as structural, dynamic and elastic properties. This alteration in the properties can produce changes in the normal functioning of the membrane [3]. Nanoparticles are characterized by high surface area to volume ratio hence they interact strongly with biological membranes which makes them particularly interesting for technological applications requiring the delivery of natural or synthetic particles to cells. Meanwhile, undesired delivery could be potentially dangerous to the cells [4]. It has been reported that the toxicity of NPs strongly depends on their physicochemical properties, such as particle size, shape, chemical composition, surface chemistry, and porosity. In addition, there has been growing interest in the investigation of the effect of surface properties of the NPs on their interaction with cells. The greatest challenge is probably to design nanoparticles that are able to enter cell membranes passively without disrupting the membrane [5]. It is equally important to understand the mechanism of cell membrane entrance and/or damage by nanoparticle so that

safer nanoparticles could be designed that would be biocompatible and nontoxic [6-7]. Hence, it becomes necessary to understand the interactions between nanoparticles and membranes.

The interaction of NPs with cell membranes can result in different cases as illustrated in Fig 1.1. Membranes may be deformed in response to external force of the NPs, and above a critical force, pores can be induced in the membrane, which enable the transport of solvent through the system [8]. It is possible that NPs do not bind with membranes at all. This can be the case if negatively charged particles are exposed to negatively charged membranes, where the electrostatic repulsion might result in no binding between the two. In another case, NPs deposit on the membrane without affecting the membrane properties or its integrity. If NP membrane interaction is stronger, NPs can attach to the membrane and induce leakage of solvent without formation of any pores in the membrane [9]. NPs can also cause reversible hole formation, where the induced pore or hole is sealed. When the NP is transported within the membrane, the latter process results in the leakage of solvent causing the diameter of the membrane to diminish [10].

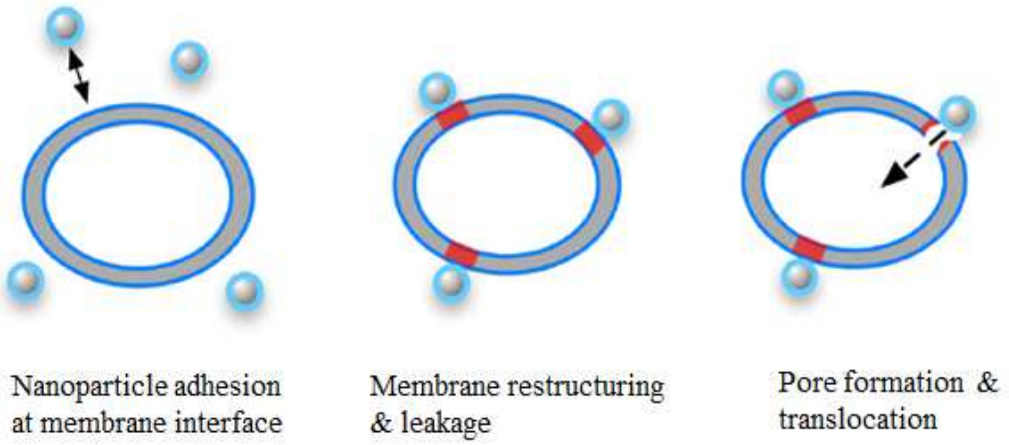

Figure 1.1: Various scenarios of interaction of NPs with the cell membrane [8]

The overall objective of my research is to understand the mechanism of interaction of nanoparticles with model cell membranes. In particular, we investigated how the size and amount of NPs affect the lipid packing, fluidity and circularity changes of cell membranes. The extent of lipid packing is one of the key physicochemical features of biological membranes and plays an important role in providing an anchorage platform for the orchestrated function of receptors and enzymes in cell signaling. We probed the formation of pores in lipid bilayers caused by the nanoparticles and attempted to determine the critical particle sizes and morphology. Lipid composition and the nature of nanoparticle affect the loading of nanoparticles and thus form important parameters for the mechanism of interaction. We characterized the lipid vesicles in samples prepared with different molar concentrations of cholesterol to vary the lipid composition and the interaction of lipid vesicles with nanoparticles was investigated. In addition, the interaction of protein-coated nanoparticles with lipid vesicles was also probed.

1.2 Probing the interactions: A Literature Survey

1.2.1 Cell membrane and lipid bilayer

All cells are surrounded by a cell membrane as was discovered by Swiss botanist Carl Nägeli and C. Cramer in 1855 [11]. The cell membrane keeps the components of the cell isolated from the external environment, while allowing the entrance of nutrients and exit of waste materials. It also serves as a communication interface between the cell and its environment [12-13]. The diverse structures and functions of the cell membrane have been defined by nearly a century of research using biochemical, physiological, cellular and molecular techniques. The cell membrane is involved in a multitude of functions such as regulating the flow of materials into and out of the cell, mediating intercellular communication and adhesion, trapping or releasing energy, cell motility and cell division [14]. The lipid bilayer model of the cell membrane was

proposed by Gorter and Grendel (1925) post Irving Langmuir's (1917) monolayer model of phospholipids [15]. Davson and Danielli (1935) proposed the sandwich model of phospholipid bilayer between two layers of proteins, which was advanced by the fluid mosaic model devised by Singer, and Nicolson (1972) [16]. Data from microscopy and calorimetry experiments have provided evidence supporting the fluid mosaic model; therefore, this model is accepted, generally, for describing how the membranes are arranged [17]. The fluid mosaic model (Figure 1.2) describes the structure of the cell membrane as a mosaic of components including lipids, carbohydrates and proteins, which give the membrane a two-dimensional fluid character.

Membrane lipids contain a hydrophilic/polar headgroup as well as two hydrophobic, long hydrocarbon chains, each of which most commonly contain 14–24 carbon atoms. The membrane bilayer is composed of two lipid monolayers (leaflets). In each monolayer, the lipids are oriented so that their polar head groups interact with water, while the hydrocarbon chains from each monolayer form the core of the membrane [18]. The lipid bilayer spans 5-7 nm in thickness.

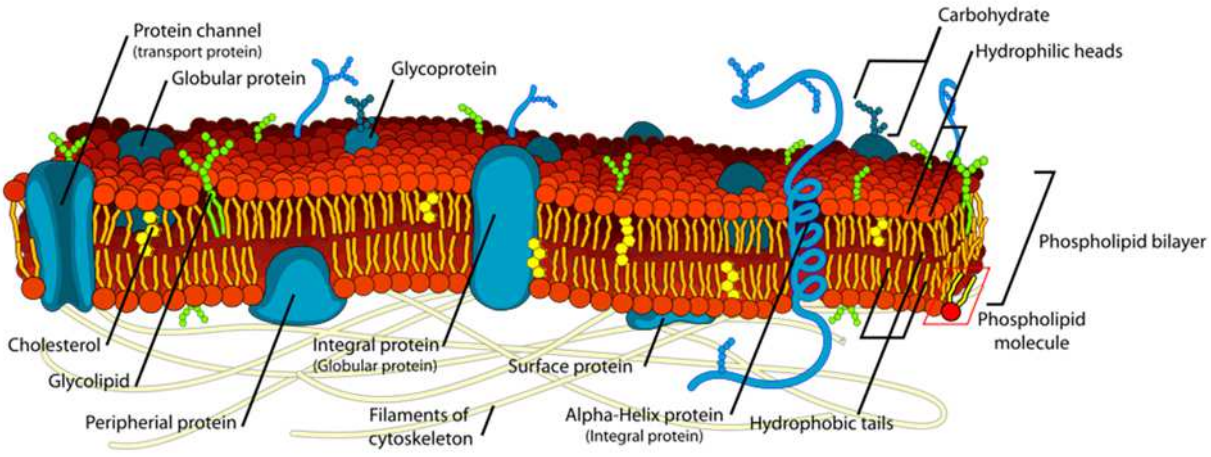

Figure 1.2: Fluid mosaic model of a cell membrane illustrating the lipid bilayer with embedded proteins. Each phospholipid molecule has a head group and two tails. The tails from each monolayer face each other to form the core of the bilayer. The glycoproteins and glycolipids are oriented towards the external environment [17].

Carbohydrates bind covalently with proteins and lipid molecules to form glycoproteins and glycolipids. The sugar groups are always oriented towards the external environment of the cell membrane as shown in Figure 1.2 [19-20]. Glycolipids form hydrogen bonds with the water molecules and so help to stabilize the membrane structure. Glycolipids also function as fuel storage for cellular tasks but most prominently, it serves as a marker for cellular recognition [21]. They also act as receptor molecules, binding with particular substances such as hormones and neurotransmitters. Glycoproteins play an important role in allowing cells to recognize each other. Proteins are embedded in the lipid bilayer. There are two types of membrane proteins: integral and peripheral membrane proteins. Integral membrane proteins interact extensively by non-polar interactions with the hydrophobic region of the lipid bilayer. Peripheral membrane proteins are usually attached to the surfaces of integral proteins therefore they are found on both faces of the lipid bilayer. Peripheral membrane proteins bind through electrostatic interactions and hydrogen bond with the hydrophilic polar head groups of the lipid molecule. This arrangement of proteins in the lipid bilayer gives rise to lipid asymmetry. The proteins of the lipid bilayer function as pumps, channels, energy transducers, receptors and enzymes [22].

Membrane lipids are generally classified as phospholipids, cholesterol and sphingolipids [23]. Phospholipid molecule is composed of a hydrophilic head and two hydrophobic tails. The hydrophilic head group consists of a phosphorous–containing group attached to a glycerol molecule. The hydrophobic tails, each containing either a saturated or an unsaturated fatty acid are long hydrocarbon chains. Phospholipids function as a reservoir of intracellular protein messengers, anchoring protein to cells, cell signaling and regulating cellular shape. Cholesterol is a sterol lipid. It is a major constituent of animal plasma membranes but it is absent in bacteria.

Almost 25% of membrane lipids in certain nerve cells are made of cholesterol although it is nonexistent from some intracellular membranes [24].

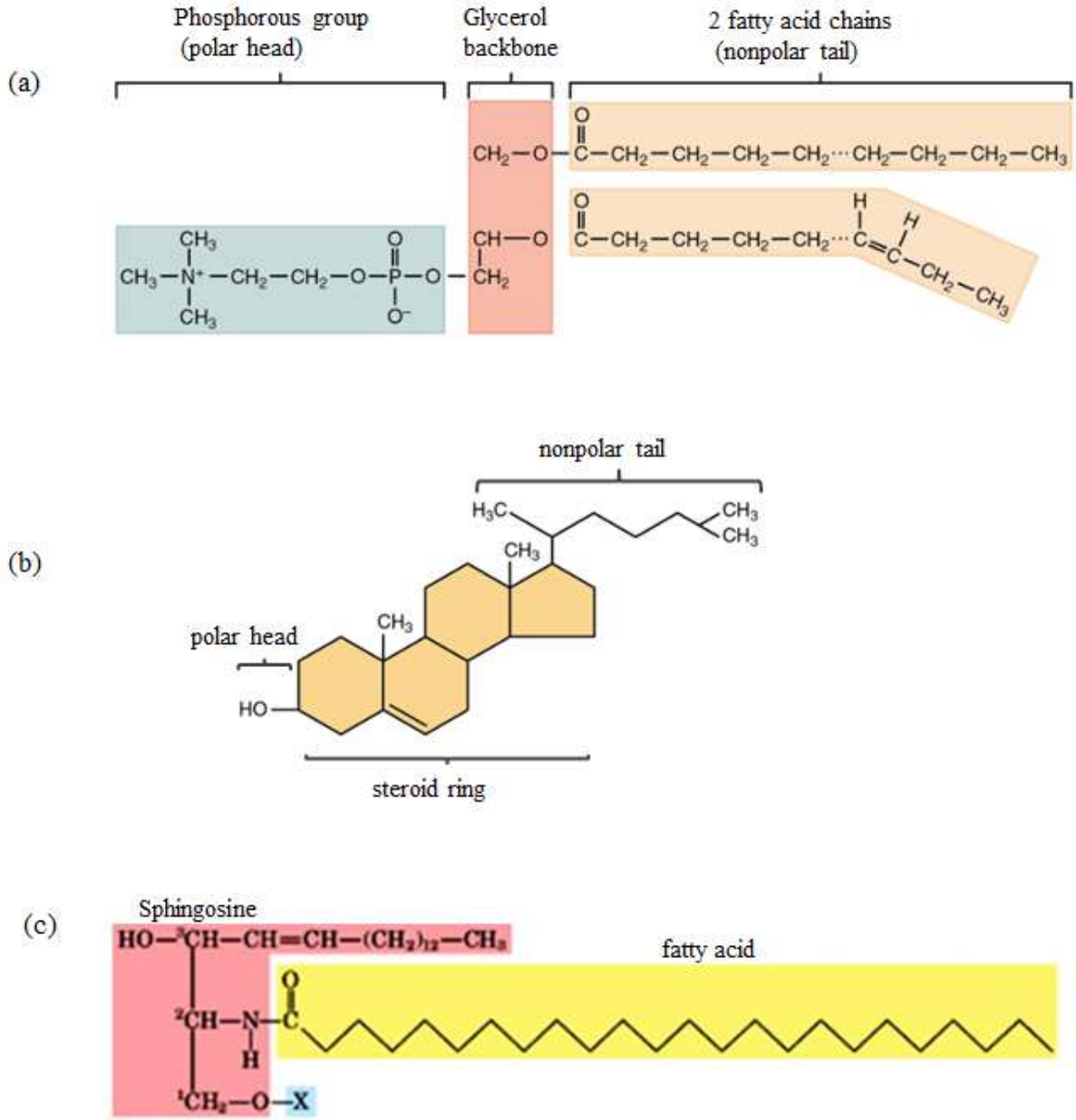

Figure 1.3: Molecular structure of (a) phospholipid (b) cholesterol and (c) sphingolipid [25]

Alike phospholipids, cholesterol molecules have hydrophilic heads and hydrophobic tails, so they can interdigitate between phospholipid molecules and regulate the fluidity of the membrane. It is built from 4 linked hydrocarbon ring. The fused ring system makes cholesterol more rigid than other membrane lipids. Cholesterol can provide mechanical stability to the membrane, supply the body with fat and provides precursors for hormone synthesis. Sphingolipids are a class of lipids with a polar head group and two nonpolar tails. The core of a sphingolipid is an amino alcohol called sphingosine. Complex sphingolipids located in the plasma membrane of animal nerve cells have a structural function and are believed to protect the cell surface from harmful environmental factors. They also serve as adhesion sites for extracellular proteins and play important roles in signal transmission and cell recognition.

It is evident that lipid composition typically includes hundreds to thousands of different lipid species [26], and is specific for each organism and for each tissue and organelle within an organism. Properties such as electrostatic charge, structural, elastic, and dynamic properties of lipid membranes depend on lipid composition, which in turn affect membrane functioning and interaction with entities such as proteins, lipids and organelles [27]. Thus the functions of lipids follows a long line from providing the structural framework for cell membrane, to serving as energy storage reservoirs, principally in lipid droplets, to more complicated operations such as delivery vehicles in signal transduction and molecular recognition processes.

One property of lipids that has fascinated scientists is its phase behavior. In cells, lipids can adopt various fluid and solid phases, which are characterized by a different spatial arrangement and motional freedom of each lipid with respect to its neighbors. The phase behavior of model lipid bilayers devised by Marieke Kranenburg and Berend Smit [28] suggests that lipids undergo structural phase transition as a function of temperature, pressure and

hydration. To a certain extent, the phase of lipid bilayers also depends on the structural properties of the lipids such as the length of the hydrocarbon chains, the composition of the head group and the positional order of either the acyl chains or the head group with in the bilayer. For example, sphingomyelin has long, saturated hydrocarbon chains; hence, bilayers rich in sphingomyelin tend to adopt solid-like phases. Most biomembranes are enriched in unsaturated hydrocarbon chains, so they tend to adopt liquid phases. Sterols by themselves do not form bilayer structure, but when integrated into lipid bilayers, they form the liquid-ordered phase. Cholesterol has been connected to the possible formation of ordered lipid domains (rafts) in mammalian cell membranes. The filling of cholesterol in between the lipids in rafts makes it a spacer molecule enabling tight packing [29].

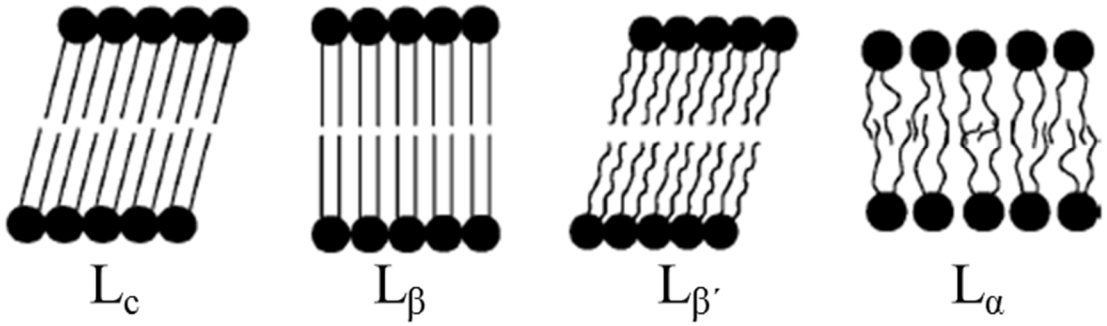

Figure 1.4: Schematic drawings of the various bilayer phases [28]

Most common phospholipids exhibit a subgel phase L_c at low temperature in which the hydrocarbon chains are highly ordered and show a tilt with respect to the bilayer normal. At elevated temperature, the subgel transforms to a lamellar gel phase. The lamellar gel phase is marked as L_β phase for phosphatidylethanolamine head group lipids and $L_{\beta'}$ phase for lipids with phosphatidylcholine head group. In the lamellar gel phase, the bilayer is more hydrated than in

the L_c phase and the hydrocarbon chains still show a high order but less than in the L_c phase. In the L_β phase the chains are ordered parallel to the normal while in the $L_{\beta'}$ phase the chains show a tilt angle with respect to the bilayer normal. At higher temperature, there is absence of any positional order in the chains and this leads to the liquid crystalline or fluid or L_α phase. [30-31].

Early pioneers in membrane physics vindicated that the biological functions of the cell membrane are linked to the physical properties, such as flexibility, fluidity and permeability, of the lipid self-assembly [32-33]. It is nearly impossible to study the physics of membrane using living cells because cells are complex entities wherein numerous phenomena are inextricably entwined in a dynamic environment. One approach is to first disentangle the physicochemical aspects of the cell membrane from the biological ones and engage in a synthetic lipid vesicle made up of minimal components as a model system. Such model systems provide a simple repeatable platform for well-controlled experiments through which it is possible to analyze how the cell membrane exploits or counteracts the fundamental physical laws [34].

Lipid vesicles, also known as liposomes are spherical constructs of the lipid bilayer, which provide a simple and stable model system for cell membranes. Lipid vesicles are important for studying membrane permeability and they can be used to deliver ions or molecules inside cells. The lipid bilayer membrane of a lipid vesicle separates the outer aqueous environment from an inner aqueous compartment through self-assembly process driven by hydrophilic heads and hydrophobic tails (Figure 1.5). Lipid vesicles retain many of the characteristics of natural cell membrane such as lateral fluidity, phase separation and in-plane diffusion [35]. Typically, unilamellar vesicles are classified according to their size as small unilamellar vesicles (SUVs, diameter < 100 nm), large unilamellar vesicles (LUVs, diameter between 100 nm and 1 μm) and giant unilamellar vesicles (GUVs) with diameter > 1 μm. GUVs

are important model membranes for microscopic study as their sizes are optimum for observation under optical microscopes [36]. The study of GUVs offers insight into the characteristic behavior of vesicles interacting with nanoparticles, and will be covered in detail in the later chapter. In this research, a phospholipid DMPC (1,2-dimyristoyl-sn-glycero-3-phosphocholine) was chosen as the major component of the synthetic lipid model membranes. The process of lipid vesicles formation involves preparing a thin lipid film, which is then hydrated, and the layers of the film separated by some sort of agitation. Each layer of the lipid film is made up of a bilayer of lipid molecules attached at the tails. The bilayer arranges in the form of a vesicle in the presence of external agitation. The small vesicles fuse to form large vesicles. Giant unilamellar vesicles (GUV) need an alternate technique involving application of electric field for its formation, owing to the size of the vesicle, which could be tens of micrometers.

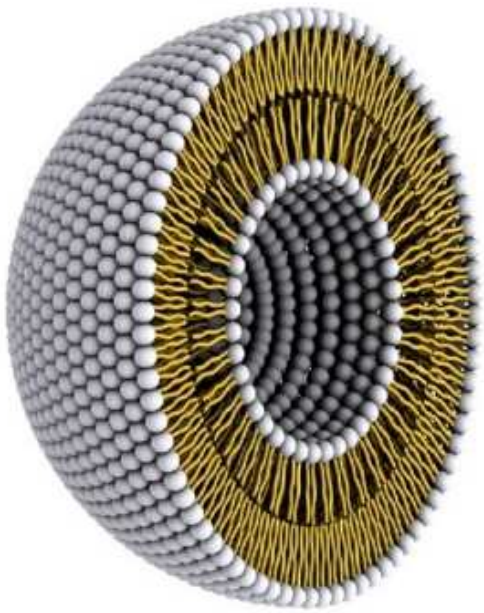

Figure 1.5: Structure of a lipid vesicle as a spherical construct of a lipid bilayer [37]

1.2.2 Nanoparticles

Nanoparticles are clusters of atoms that are between one and 100 nanometers in size and consist of a core of atoms surrounded by surface-protecting molecules. They are complex many-electron-systems where quantum confinement effects arising from size play a crucial role for their applications in nanotechnology [38]. They have high surface to volume ratio, which results in different physicochemical properties from their larger counterparts. The nanoscale size of these particles facilitates various communications with the biomolecules on the cell surfaces and within the cells in such a way that the interactions can be decoded and designated to numerous biochemical and physicochemical properties of the cell [39]. Today, these materials can be synthesized and modified with various chemical functional groups, which allow them to be conjugated with antibodies, ligands and drugs of interest. Nanoparticles offer a wide range of potential applications in biotechnology [40], such as magnetic separation, therapeutic delivery vehicles for gene and drug delivery [41], biological labeling and sensors, catalysis, diagnostic imaging [42] and more importantly cancer therapy [43]. Usually Au (Gold), Ag (Silver), Cu(Copper), Pt (Platinum), Pd (Palladium), Ru (Ruthenium) are commonly used metal nanoparticles whereas Al_2O_3, MgO, ZrO_2, CeO_2, TiO_2, ZnO, Fe_2O_3 and SnO are categorized as metal oxide nanoparticles [44].

Among the different existing nanoparticles, the most widely used nanoparticle is the gold nanoparticle (AuNP). AuNPs have attracted attention because of their shape-dependent and size-dependent physical and chemical properties. They are biocompatible, highly size tunable, have high surface energy which facilitates ligand formation and its fabrication techniques have been well developed [45, 50]. AuNPs absorb light in the visible range of the spectrum due to surface

plasmon resonance (SPR) which makes it relatively simple to apply optical and spectroscopic methods for its detection.

1.3 Dissertation structure

Experimental techniques such as spectrofluorometry, fluorescence microscopy, and darkfield microscopy were utilized to investigate the interaction between nanoparticles and lipid vesicles. This dissertation research has been divided into six chapters. A short description of the contents of each chapter is given below to aid the reader in navigating this dissertation.

Chapter I provides an overview of cell membranes with focus on the lipid bilayer and its properties. A brief description of nanoparticles and the interaction between the nanoparticles and lipid bilayers is mentioned. The fundamental problem is clearly stated and the scope of our work defined.

Chapter II discusses the fluidity changes of the lipid vesicles induced by gold nanoparticles. This experiment was conducted with laurdan as a fluorescent probe in spectrofluometry analysis. The chapter provides a detailed description of the experimental methodology and results of the experiment.

Chapter III presents the circularity changes in the lipid vesicles induced by gold nanoparticles. The fluidity changes of vesicles can be translated into the changes in circularity of the vesicles, which are studied with a fluorescence microscope and imaging program ImageJ.

Chapter IV provides a report on AFM studies, which were carried out to study the elasticity changes, deformation and formation of pores on the lipid vesicles when gold nanoparticles were introduced.

Chapter V discusses dark field microscopy and hyperspectral imaging for visualizing GUVs and determining the effect of the composition of GUVs when altered with the addition of cholesterol,

on nanoparticle loading. AuNPs were coated with a protein corona of 10% bovine serum albumin (BSA) to form a complex AuNP_PC. A hyperspectral analysis based on dark-field microscopy was then utilized to assess how AuNPs, AgNPs, AuNP_PC and BSA influence membrane modifications and responses of GUVs characterized by different molar concentration of cholesterol.

Chapter VI gives a summary of our investigations. Suggestions for future experimental and computational work are also discussed.

CHAPTER II

FLUIDITY CHANGES OF LIPID VESICLES INDUCED BY GOLD NANOPARTICLES

Biological membranes are fluid in nature. Membrane fluidity is a measure of the viscosity of the lipid bilayer, which affects the rotation and diffusion of membrane proteins and thereby the functions of these molecules. One determinant factor for membrane fluidity is lipid composition, which in turn determines the packing of lipid molecules. The incorporation of NPs is expected to influence the fluidity of lipid bilayers by causing structural reorganizations or changes in dynamic and elastic properties of lipid bilayers. The generalized polarization (GP) of laurdan, in combination with fluorescence spectroscopy was used for measuring membrane phase or lipid packing in model membrane vesicles composed of DMPC. Higher GP values indicate a membrane in a more ordered structure, whereas lower GP values point to a membrane in a less ordered fluid phase.

2.1 Fluorescence

Fluorescence is the spontaneous emission of light during transition of a molecule from its lowest vibrational energy level of an excited singlet state S_1 back to the ground state S_0. It is one form of a quantum process called photoluminescence, which becomes visible as optical radiation during the relaxation of a molecule from an excited (higher energy) state to its (lower energy) ground state accompanied by the emission of a photon [51]. When an electron in a molecule with a singlet ground state is excited via absorption of radiation to a higher energy level, either an excited singlet state or an excited triplet state will form. A singlet state is a molecular electronic state such that the spin of the excited electron is paired with the ground state electron spin. In a

triplet state, the spin of the excited electron is no longer paired with the spin of the ground state electron, which means the spins are parallel. Since excitation to a triplet state involves an additional "forbidden" spin transition, it is less probable that a triplet state will form when the molecule absorbs radiation. The emission of light through the fluorescence process is nearly simultaneous with the absorption of the excitation light due to a relatively short time delay between photon absorption and emission, ranging usually less than a microsecond in duration. British scientist Sir George G. Stokes first described fluorescence in 1852 and was responsible for coining the term when he observed that the mineral fluorspar emitted red light when it was illuminated by ultraviolet excitation. Stokes noted that the fluorescence emission always occurred at a longer wavelength than that of the excitation light. As a result of the energy loss, the emission spectrum of an excited fluorophore is usually shifted to longer wavelengths when compared to the absorption or excitation spectrum. This shift is known as Stokes' Law or Stokes' shift**.** The greater the Stokes shift, the easier it is to separate excitation light from emission light. The emission intensity peak is usually lower than the excitation peak, and the emission curve is often a mirror image of the excitation curve, but shifted to longer wavelengths. In order to achieve maximum fluorescence intensity, the fluorophore is usually excited at the wavelength at the peak of the excitation curve, and the emission detection is selected at the peak wavelength of the emission curve. The time scale of fluorescence is 10^{-9} to 10^{-6}s. The process of quenching can decrease fluorescence intensity. A variety of processes can result in quenching, such as excited state reactions, energy transfer, complex-formation and collision quenching. Quenching upon interaction with a specific molecular target is the basis for optical contrast agents for molecular imaging and for Forster resonance energy transfer (FRET) assays [52].

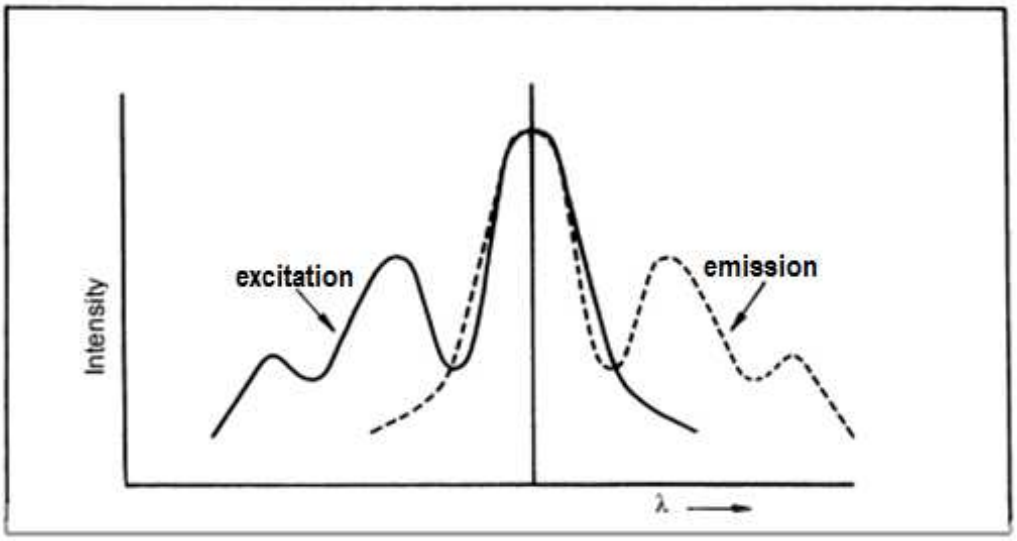

Figure 2.1: Idealized excitation and emission spectra [51]

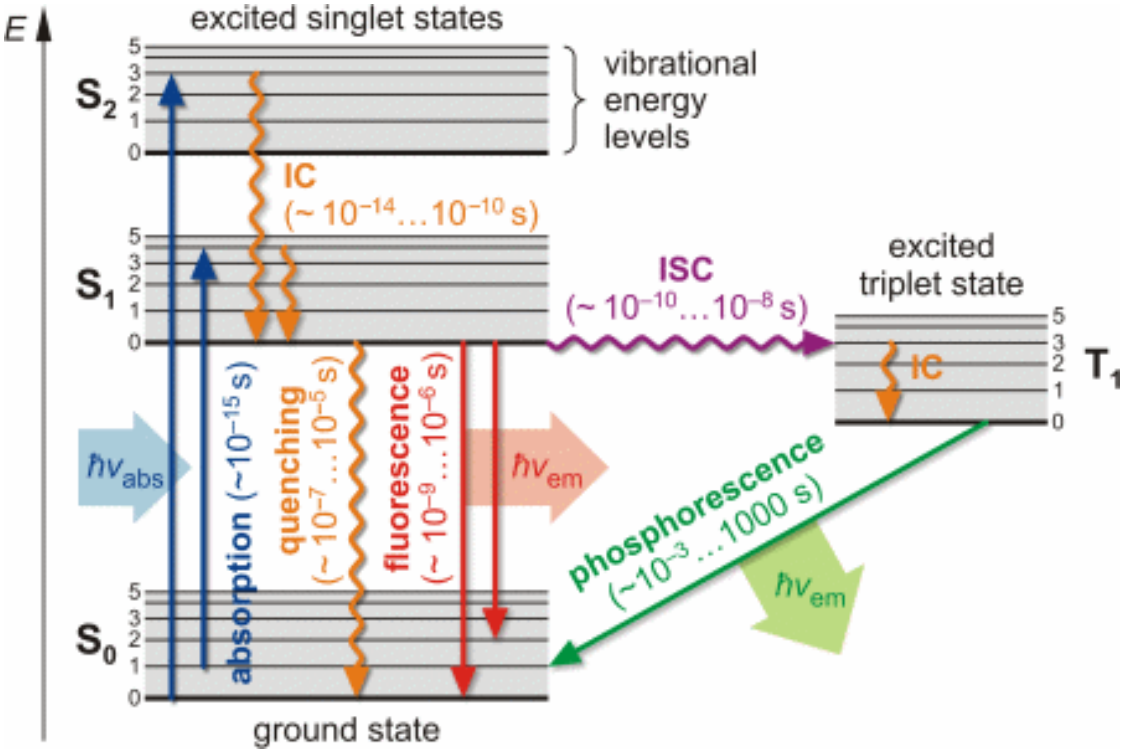

Figure 2.2: Jablonski energy diagram illustrating the transitions between electronic states of a molecule for the quantum mechanical processes of fluorescence and phosphorescence. Wavy lines mark non-radiative transitions, namely internal conversion (IC), intersystem crossing (ISC) and quenching [52].

Figure 2.2 illustrates a Jablonski energy diagram representing fluorescence. The blue arrows represent the absorption of photons. The orange wavy lines represent vibrational relaxation within or between singlet excited states. This process is a non-radiative relaxation in which the excitation energy is dispersed as vibrations or heat to the solvent and no photon is emitted. Intersystem crossing (ISC) shown by violet wavy line, is a radiationless process involving a transition between two electronic states with different spin multiplicity. In essence, the spin of the excited electron is reversed. The probability of ISC occurring is favorable when the vibrational levels of the two excited states overlap, since little or no energy must be gained or lost in the transition. Radiative decay from an excited triplet state back to a singlet state is known as phosphorescence. Phosphorescence is a manifestation of ISC since a transition in spin multiplicity occurs. The time scale of phosphorescence is 10^{-3} to 10^{3}s, which is one of the slowest forms of relaxation. The red arrows represent fluorescence to the singlet ground state, S_o. The fluorescence spectrum is determined by the spacing of its energy levels and the probabilities of transitions between them. The fluorophore's environment influences its lifetime (transitions kinetic constants) and its spectrum (spacing of levels) [53-54].

Fluorescence follows the Franck-Condon Principle, which states that the redistribution of electron density caused by an electron transition happens at a much faster scale than reorientation of nuclei [55]. When a fluorophore is placed in a solvent, the dipole moment of the fluorophore interacts with the molecules of the solvent through dipole–dipole interactions. The dipole moment of the fluorophore is shown in Figure 2.3 with a blue arrow across solid blue circles and the red arrows indicate the molecules of the polar solvent. The molecules of the polar solvent are oriented in a way such that their dipole moments compensate for the dipole moment of the fluorophore in order to minimize the total energy of the system (fluorophore + solvation

envelope). The dipole moment of the fluorophore increases upon excitation and may reorient with respect to the solvent dipoles. Reorientation of the fluorophore's dipole moment upon excitation leads to an energetically unfavorable Franck-Condon state from which the system relaxes through reorientation of fluorophore's solvation envelope to a state of lower energy. The solvent relaxation introduces an additional red shift to the Stokes shift of the fluorophore [56].

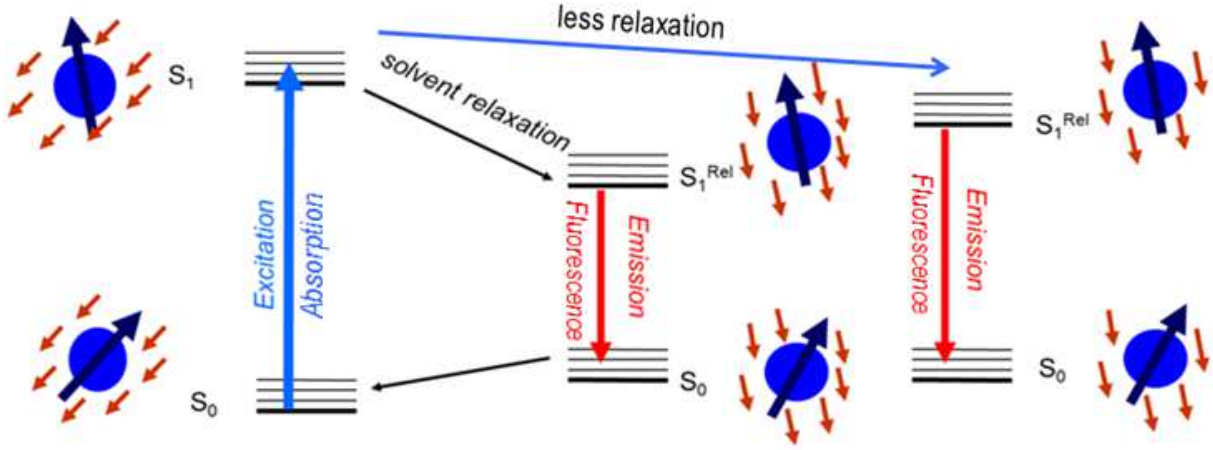

Figure 2.3: Dipolar relaxation of solvent molecules and its effect on fluorescence spectrum [55]

2.2 Laurdan

Laurdan (6-dodecanoyl-2-dimethylamino-naphthalene) is a commonly used polarity sensitive fluorescent probe which was first designed and synthesized by Gregorio Weber [56] to study the phenomenon of dipolar relaxation. It is widely used in phospholipid membrane studies to assess membrane physical properties. A great advantage of laurdan among other fluorescent probes is that it partitions into the lipid phase and its solubility in water is negligible. It is made of a dimethylamino electron-donating group, a carbonyl electron acceptor and a fluorescent naphthalene moiety. Laurdan is incorporated into the membrane with the fluorescent naphthalene

moiety situated at the level of the interface (glycerol backbone) region, and the lauric acid tail anchored in the hydrophobic core of the lipid bilayer [57]. The fluorescent naphthalene moiety of laurdan possesses a dipole moment due to a partial charge separation between the 2-dimethylamino and the 6-carbonyl residues. Upon excitation in the UV-region (340 nm), the dipole moment of laurdan increases and water molecules in the vicinity of the probe will adapt to this new dipole [58]. In tightly packed gel phase membranes with reduced molecular mobility in the hydrophobic region, the dipolar relaxation of the water molecules is too slow to change the properties of fluorescent emission, thus the emission spectra have only one peak at 440 nm. However, in loosely packed fluid phase membranes, where the interior is fluid allowing the lipid molecules to move around, dipolar relaxation of water molecules occurs, and it is apparent as a 50 nm red-shift fluorescence at 490 nm, in the emission spectra of laurdan [59-60].

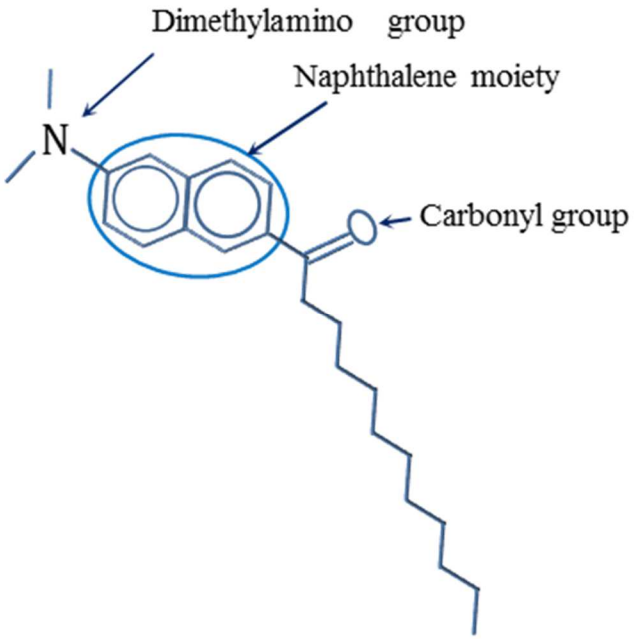

Figure 2.4: Structural formula of a laurdan molecule illustrating the dimethylamino group, naphthalene moiety and the carbonyl groups. The partial charge separation between the dimethylamino and the carbonyl groups gives rise to a dipole in the naphthalene moiety

This phase dependent red shift in the steady-state emission spectrum of laurdan reflects the excitation energy spent for relaxation of water molecules in the surroundings of the probe, and at the same time reports on the molecular dynamics in the membrane interface region. The population of solvent molecules, such as water, affects the relaxation process of laurdan. Higher number of solvent molecules allows more relaxation of laurdan thus a red shift in the fluorescence spectrum as compared to that from lower number of solvent molecules. Therefore, laurdan can be used to probe the polarity of the solvent environment through its emission spectrum. The emission maxima of laurdan in the gel phase of the lipid membrane is at 440 nm and in the fluid phase the emission maxima is at 490 nm as shown in Figure 2.5

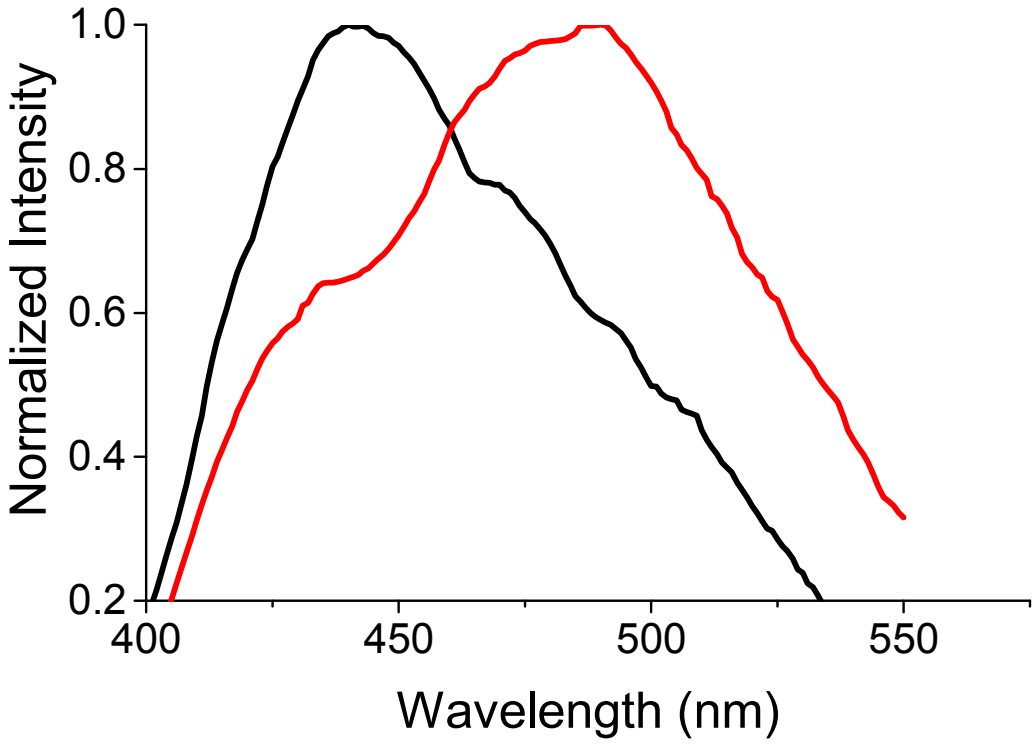

Figure 2.5: Fluorescence red shift of laurdan. The emission maxima of laurdan in the gel phase (black- Control) of the lipid membrane is at 440 nm and in the fluid phase (red- 10nm 100uL AuNP treated DMPC vesicles) the emission maxima is at 490 nm

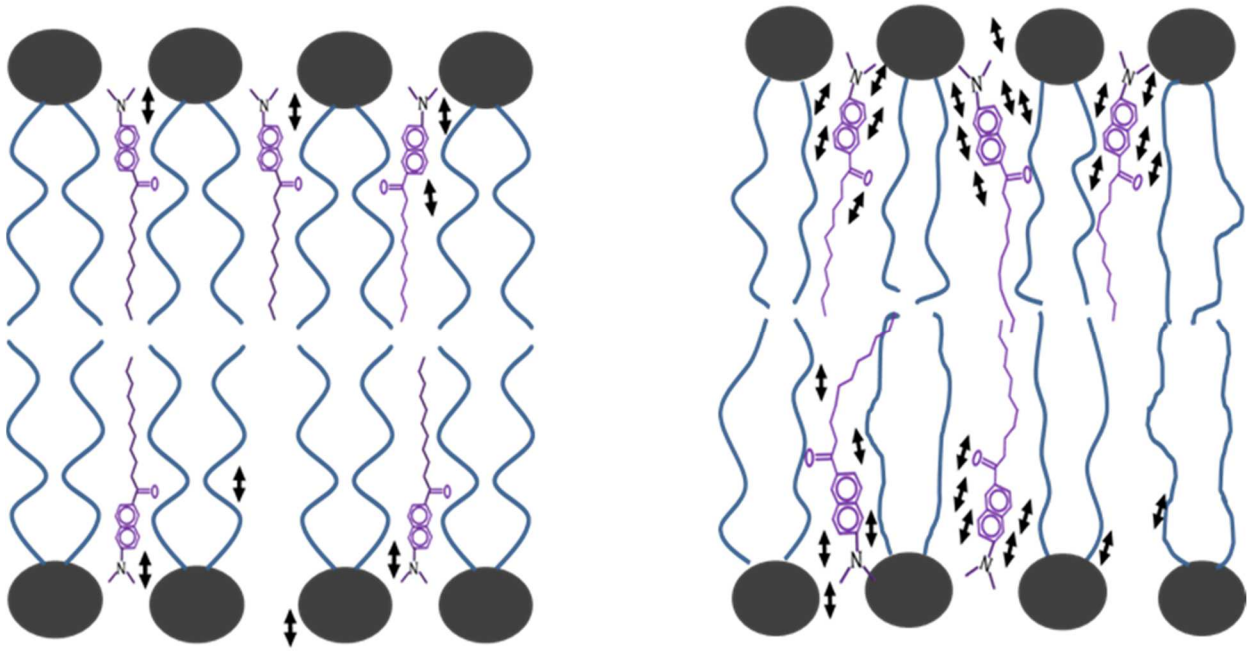

Figure 2.6: Laurdan probing the gel and fluid phases of lipids. The double-headed arrows represent the water molecules. In the gel phase, the lodging of water molecules is inhibited whereas in the fluid or disordered phase there is an increased amount of water molecules surrounding the naphthalene moiety of laurdan.

Illustrated in Figure 2.6, the laurdan naphthalene moiety resides at the level of glycerol backbone of a lipid membrane and the double headed arrows represent the water molecules in the surrounding. In the ordered or gel phase , the tight packing of the lipid molecules prevents lodging of water molecules in the hydrophobic region of the bilayer. Whereas in the disordered or fluid phase, the laurdan naphthalene moiety is surrounded by an increased amount of water molecules, since the packing is not as tight as in the gel phase [61]. Because of the difference in the surrounding water molecules, the emission maximum of laurdan is violet at 440 nm in the gel phase and blue at 490 nm in the fluid phase (Figure 2.5). The red shift of emission depends only on the phase state of the lipid bilayer and is independent of the polar head or its charge.

The dual emission of Laurdan is quantified by generalized polarization (GP) function as

$$\mathrm{GP} = \frac{I_{440} - I_{490}}{I_{440} + I_{490}} \qquad (2.1)$$

where, I_{440} and I_{490} are emission intensities at 440 nm and 490 nm respectively [62-66]. An increase in GP value from the control indicates a phase transition towards a gel phase whereas a decreased GP value represents fluidization.

2.3 Lipid vesicle

Lipids with phosphocholine head group are generally the most abundant lipids in animal cell membrane providing structural framework. Phosphocholine head group is common in the outer leaflet of the membrane where it functions as part of the permeability barrier. Vesicles prepared from DMPC (1,2-dimyristoyl-sn-glycero-3-phosphatidylcholine) were used as a model membrane in the research. DMPC is a zwitterionic phospholipid molecule, which means it is electrostatically neutral over a wide pH range. It has 14 carbons in the two saturated fatty acid tails. The structural formula of a DMPC molecule is shown in Figure 2.7. It has a glycerol backbone supporting the two saturated acyl chains which make up the hydrophobic tails of the lipid. The phosphate group is attached to a choline moiety and forms the hydrophilic head of the lipid molecule [67]. The zwitterionic nature of the phosphocholine head group is because of the presence of a choline moiety (quaternary ammonium group) and a phosphate moiety. The gel to fluid phase transition temperature of DMPC is T_m = 24° C. Between the gel phase and the high temperature L_α fluid phase, DMPC exhibits the ripple phase with static out-of-plane, sawtooth structure, breaking the statistically flat symmetry of adjacent phases. DMPC is soluble in chloroform/methanol solvents [68].

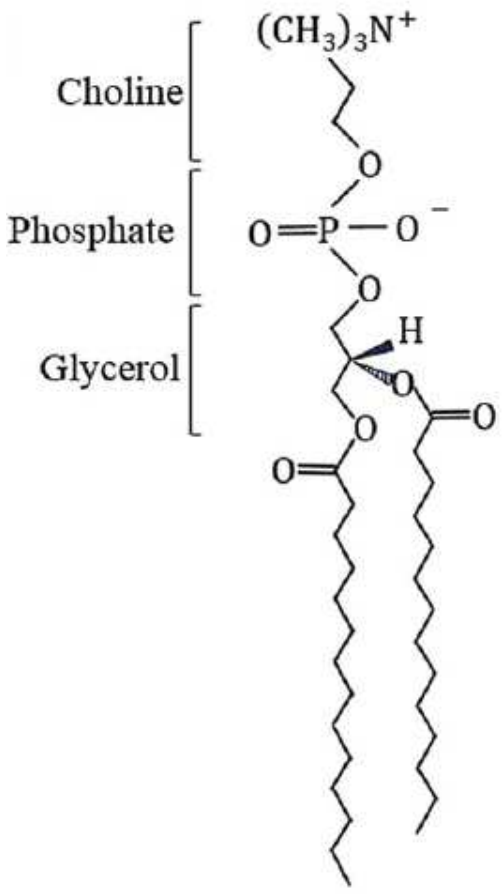

Figure 2.7: Structural formula of a DMPC molecule. The head group (PC) is zwitterionic due to anionic phosphate and cationic amine groups. PC is linked to 14 carbon atom hydrocarbon chains via the glycerol group

2.3.1 Preparation of lipid vesicles

Generally, liposomes (lipid vesicles) are formed when thin dried lipid films are hydrated and the stacks of liquid crystalline bilayers become fluid and swell [69-70]. The hydrated lipid sheets detach during agitation and self-close to form large, multilamellar vesicles (LMV) which prevents interaction of water with the hydrocarbon core of the bilayer at the edges. Disruption of LMV suspensions using sonic energy (sonication) usually produces small, unilamellar vesicles

(SUV) with radii in the range of 15-50nm. When allowed to stand overnight, SUV can fuse to form large, unilamellar vesicles (LUV) [71].

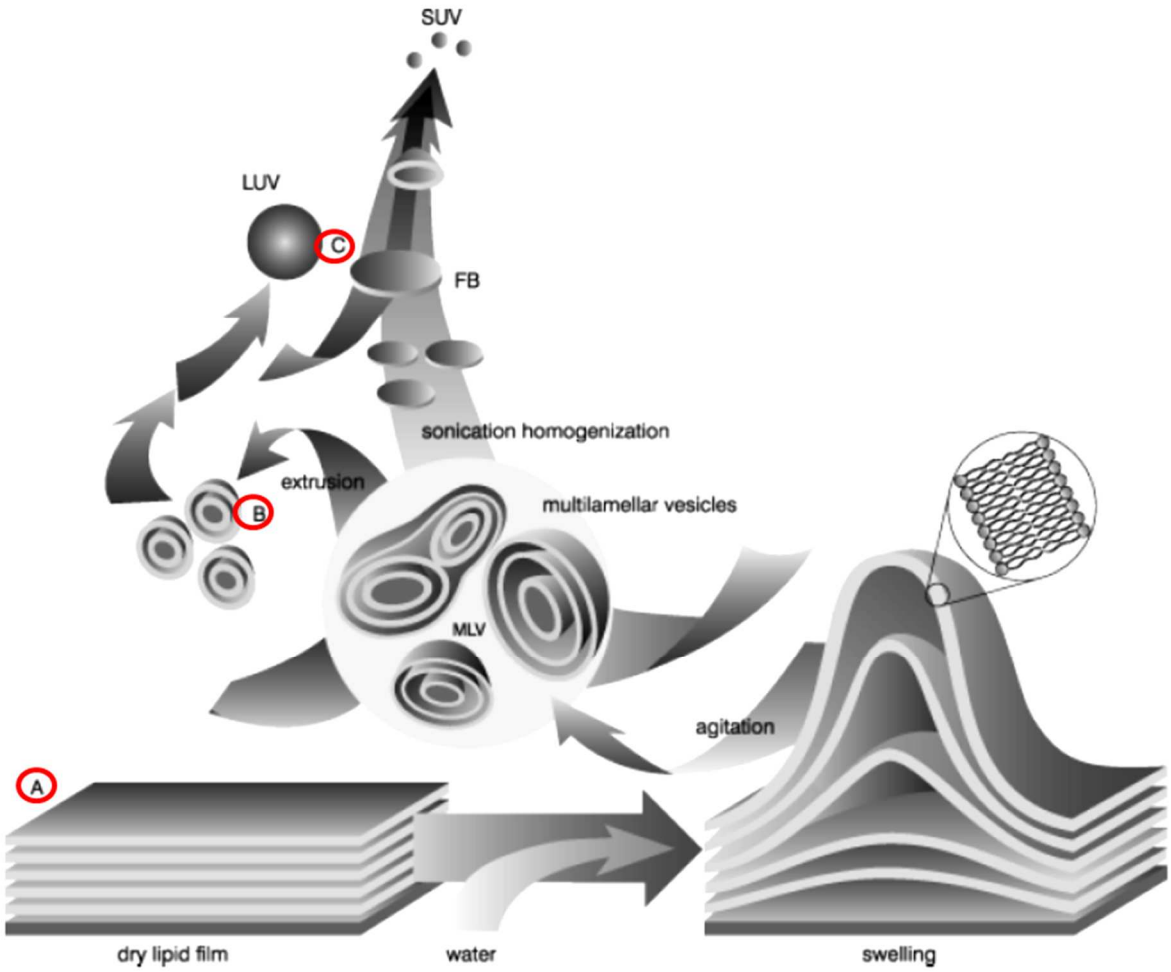

Figure 2.8: Mechanism of formation of SUVs and LUVs [71]

2.4 Spectrofluorometer

Spectrofluorometer is an instrument for measuring fluorescence signature of a fluorophore in a sample based on its specific excitation and emission wavelengths. It takes advantage of the fluorescent properties of fluorophore molecules to probe the chemical/physical environment in a sample. The essential components of a spectrofluorometer include a light source, an excitation monochromator, a sample cell/cuvette, an emission monochromator and a detector [72].

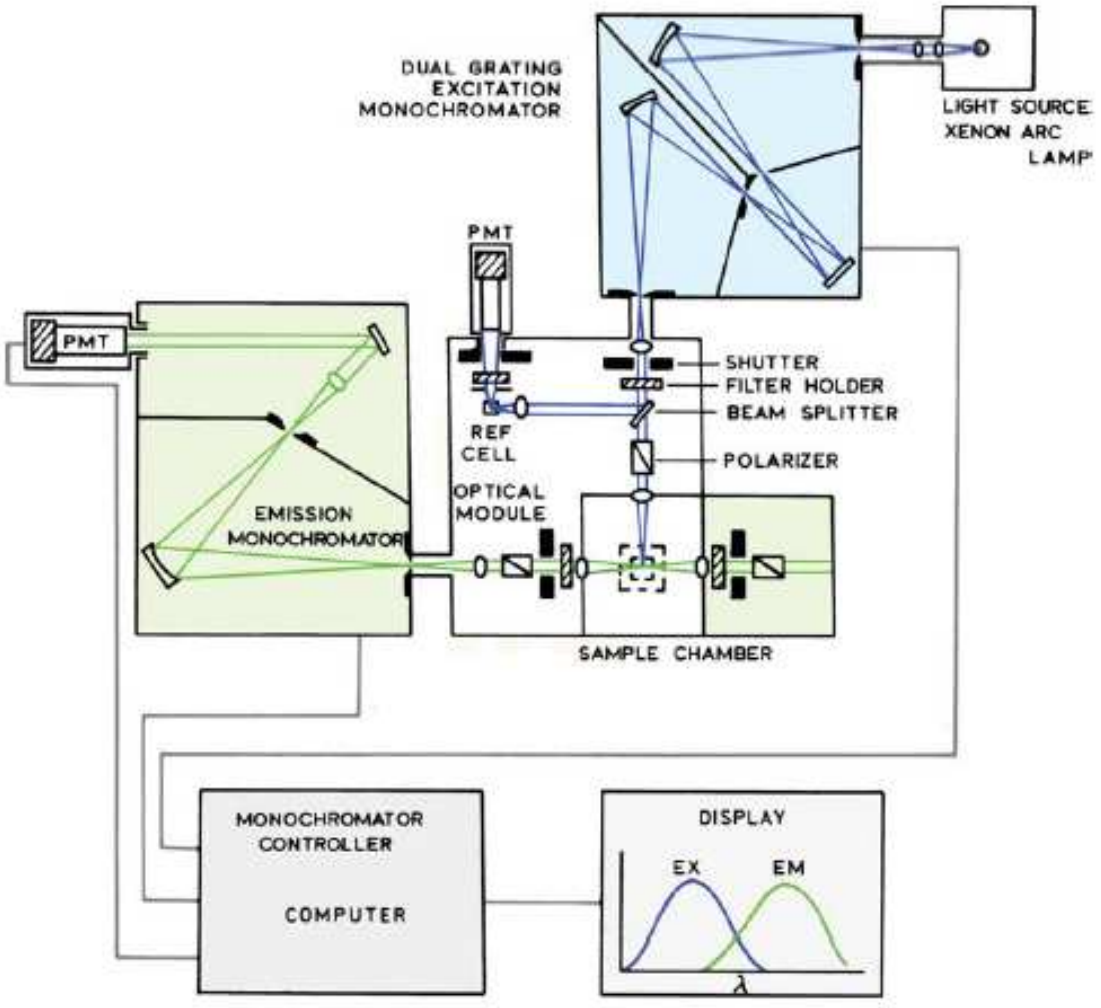

Figure 2.9: Schematic diagram of a spectrofluorometer showing the light source, excitation monochromator, sample chamber, emission monochromator and a detector [72]

The light from the source passes through the excitation monochromator, which transmits a wavelength specific to the excitation peak of the fluorophore while blocking other wavelengths. The excitation light then passes through the sample contained in the sample cell/cuvette holder and excites the sample. Following excitation, the fluorophore relaxes and emits light at an emission wavelength longer than the excitation wavelength. The emitted light passes through the emission monochromator positioned at a right angle to the excitation light

path. The emission monochromator minimizes light scatter and screens the emission light before it reaches the detector. The detector measures the emitted light and produces the fluorescence signature of the fluorophore. The fluorescence value is proportional to the concentration level of the fluorophore in the sample. Herein the effect of AuNPs on the lipid packing and the fluidity of the vesicles were studied using ISS K2 spectrofluorometer.

2.4.1 Main components of ISS K2 spectrofluorometer

The main components of the ISS K2 spectrofluorometer include excitation/emission monochromator, polarizers, beam splitter, quantum counter and photon multiplier tubes (PMT). The light source was a xenon lamp, which provides a relatively continuous light output from 250 to 700 nm. Excitation spectra are distorted primarily by the wavelength dependence of the intensity of the exciting light. This intensity can be converted to a signal proportional to the number of incident photons by the use of a quantum counter. A PMT is a detector, which responds to individual photons. Each photoelectron results in a burst of 10^5 to 10^6 electrons, which can be detected as individual pulses at the anode. PMTs can be operated as photon counters, or can be used in the analog mode in which the average photocurrent is measured. In photon-counting mode, the individual anode pulses due to each photon detected are counted. As a result, the detection system is operating at the theoretical limits of sensitivity. Data collection for the experiment was carried out in the photon-counting mode. The excitation wavelength during operation was set at 340 nm and the emitted fluorescence was recorded from 360 nm to 500 nm. The spectrofluorometer was utilized in the steady state (SS) fluorescence method which involves measurement of the long term average fluorescence of the sample when irradiated with UV, visible or near infrared (NIR) light [73].

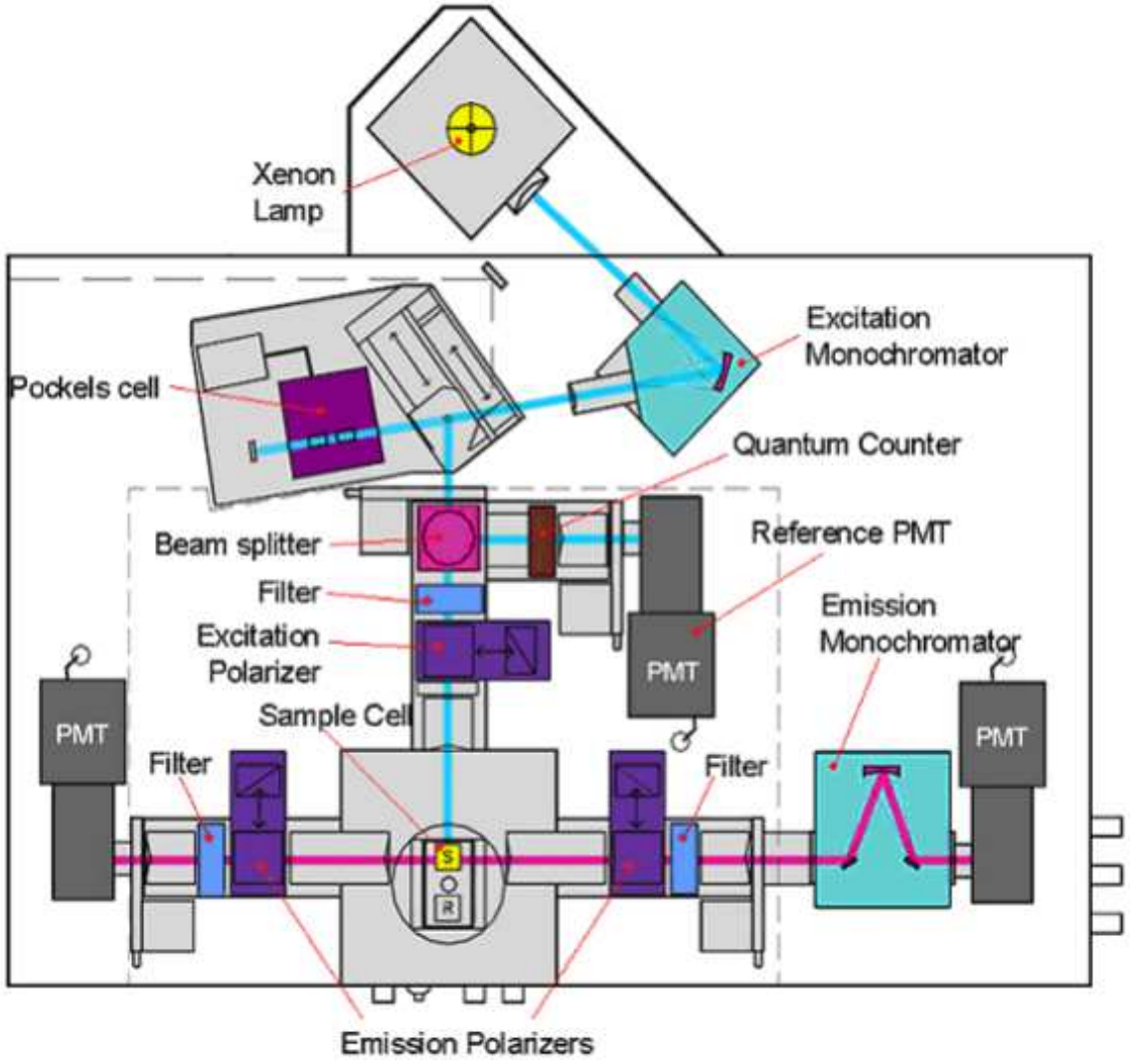

Figure 2.10: Main components of ISS K2 spectrofluorometer [73]

2.4.2 Calibration using Raman scatter peak of water

The presence of background fluorescence and/or scattered light is the most common error in fluorescence measurements. One of the methods commonly used for checking instrument sensitivity is the measurement of the Raman spectrum of water. Pure water has two scatter peaks: Rayleigh and Raman. Rayleigh scattering is due to elastic scattering of the incident light and therefore occurs at the same wavelength as the excitation. The Raman peak is a result of inelastic

scattering. A fraction of the incident photons loses energy to vibration in water molecules and the photon is then scattered at a higher wavelength than the incident light. Raman scatter always occurs at a constant wavenumber difference from the incident light, and can be identified by changing the excitation wavelength. For water, the Raman peak appears at a wavenumber 3400 cm^{-1} lower than the incident wavenumber. The spectral width of the Raman peak is determined by the resolution of the monochromator. As shown in Figure 2.11, the Raman spectrum of water has a maximum at 397 nm (the Raman peak of water is shifted 3400 cm^{-1} from the Rayleigh peak) upon excitation at 350 nm suggesting that the system is calibrated for optimum use. The intensity of the light and the width of the excitation and emission slits were unchanged for the rest of the experiment.

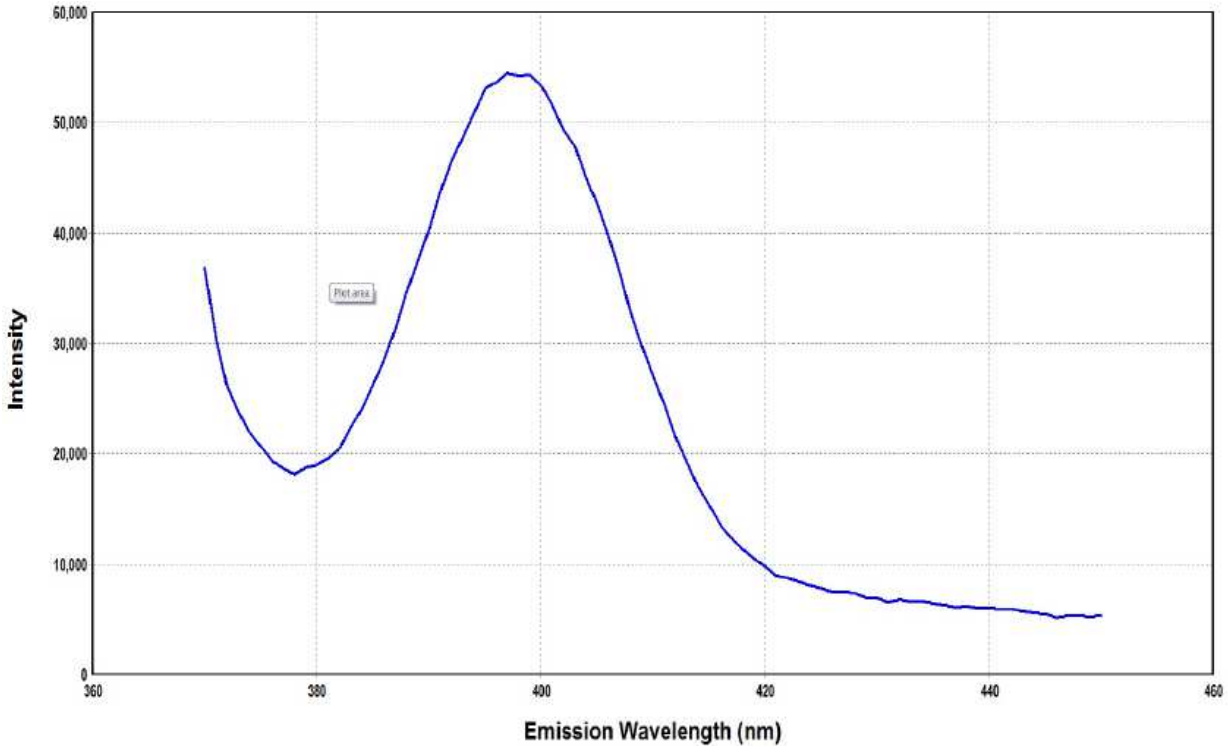

Figure 2.11: Raman spectrum of water with a maximum at 397nm

2.4.3 Vinci Software

Vinci is a comprehensive multidimensional fluorescence spectroscopy software program designed to enhance the capabilities and performance of ISS spectrofluorometer. It offers performance through three distinct features namely; instrument control, data acquisition and data analysis.

Vinci provides full control over all automated instrument components including shutter, polarizer, sample holder, monochromator, and enables integration of external devices such as stopped flow apparatus, titrator and temperature bath.

It offers a variety of data acquisition options (spectra, lifetime, kinetics, titrations) through built in routines and allows the user to generate, store and rerun custom designed data acquisition protocols. Data are stored in ASCII format for convenient access from other software packages.

Vinci's fast fitting routines allow obtaining time resolved spectra with picosecond resolution and to separate steady state spectra of up to 3-components in a mixture using phase and modulation resolved spectra measurement option. Other operations include smoothing, derivative, calculation of area and arithmetic between files. A graphical user interface generates and displays 2D and 3D plots that can be exported in internet- and presentation-ready formats. A report can be saved in Word or PDF format [73].

2.5 Experimentation

We prepared DMPC vesicles by thin lipid film extraction method [74]. First, a stock solution of 8 mg/mL of DMPC/$CHCl_3$ was made by dissolving DMPC (1,2-dimyristoyl-sn-glycero-3-phosphocholine, Sigma-Aldrich) in chloroform. We took 0.5 mL of the stock solution

and diluted it with 1.5 mL chloroform. 0.5 mg of fluorescent dye, Laurdan (6-dodecanoyl-2-dimethylamino-naphthalene, Invitrogen) was added to allow for partitioning in the lipid bilayer for spectrofluorometric study. The solution was allowed to stand until chloroform evaporated entirely to leave a residue of lipid film. The dried lipid film was hydrated in 2 mL of phosphate buffered saline (PBS, 10 mM) and incubated at 37^{o}C for 10 minutes followed by vigorous vortexing. The dried lipid film swell upon hydration and the agitation applied through vortexing results in formation of multilamellar vesicles from the swollen lipid layers. The incubation and vortexing was repeated three times to ensure a thorough conversion of the hydrated lipid film to vesicles. The sample was subsequently sonicated in a water bath for 10 minutes, which led to the formation of small unilamellar vesicles (SUVs). We let the suspension stand at room temperature for 36 to 48 hours to allow the SUVs to fuse into large unilamellar vesicles (LUVs).

We then mixed 25 μL of DMPC vesicles with AuNPs (prepared by citrate reduction and stabilized in 0.1 mM PBS, Sigma-Aldrich) of various sizes (5, 10, 20, 30 nm) and different amounts (25, 50, 75 and 100 μL) into 1 mL of PBS. The mixed solution was incubated at room temperature for 2 to 3 hours to ensure a sufficient AuNP- DMPC vesicle interaction and equilibration. To examine how AuNPs affect the lipid packing in DMPC vesicles, 500 μL of each sample was diluted with 2 mL PBS buffer for a spectrofluorometric analysis (K2 spectrofluorometer, ISS, Inc.). The fluorescence of laurdan was excited at 340 nm and the emission intensities were recorded from 360 to 500 nm.

We also conducted the experiment on extruded DMPC vesicles. The extrusion was performed on a mini-extruder (Avanti Polar Lipids, Inc.) by passing as-prepared LUVs through a polycarbonate membrane (pore size 100 nm, Whatman) 12 times. The resulting vesicles were

uniform in size and smaller in diameter. They were then added with AuNPs for spectrofluorometric studies as previously described for non-extruded DMPC vesicles.

AuNPs of sizes 5nm, 10nm, 20nm, and 30nm (stabilized in 0.1 mM phosphate buffered saline) were ordered from Sigma-Aldrich. The concentration of AuNPs for each size given as particles/mL (Table 2.1) was obtained from the specification sheet provided by Sigma Aldrich. X-ray crystallography experiments have shown that there are 4 gold atoms per unit cell for gold and the edge length of the unit cell is 0.408 nanometers. The volume of the unit cell is therefore 0.408^3= 0.0679 cubic nm. The mass per particle (g) of AuNPs of mentioned sizes was determined to be (4/3*pi*r^3/0.0679)*4, where r is the radius of the AuNP. The total concentration (g/mL) of different size AuNPs was calculated as the product of concentration given in particles/mL and mass per particle (g) of AuNPs. Tabulated in Table 2.1 are the specifications for concentrations of different sized AuNPs in particles/mL, mass per particle (g) and concentration (g/mL).

Table 2.1: Specifications for concentrations of different sized AuNPs in particles/mL, mass per particle (g) and concentration (g/mL)

Size of AuNP	particles/mL	mass per particle (g)	conc. (g/mL)
5 nm	5.50E+13	1.26E-18	6.93E-05
10 nm	6.00E+12	1.01E-17	6.06E-05
20 nm	6.54E+11	8.08E-17	5.28E-05
30 nm	1.80E+11	2.73E-16	4.91E-05

Following the protocol for preparation of DMPC vesicles, we used 0.5mL of 8mg/mL of DMPC/ $CHCl_3$ stock solution. After evaporation of CHCl3, 2mL of PBS was added to hydrate the layers of the dried lipid film. 25µL of solution containing DMPC vesicles was then used in each sample for the experiment. This amounts to 8mg/mL * 0.5mL /2mL * 0.025mL = 0.05mg of DMPC concentration in each sample. The molecular weight of DMPC is 677.93 g/mol. Thus the number of DMPC molecules present in the sample is calculated as 0.05mg * 6.02E+23 mol^{-1}/677.93 g mol^{-1} = 4.44 E+16. The number of DMPC pairs is calculated to 2.22E+16.

Shown in Table 2.2 is the calculated ratio of the number of DMPC pairs to the number of AuNPs (concentration in particles/mL) in a particular sample. The ratio is three to six orders higher than 1 establishing that the number of DMPC molecules is greater than the number of AuNPs.

Table 2.2: Ratio of number of DMPC pairs to number of AuNPs for mentioned size and concentration of AuNPs

Size/amount of AuNP	25 µL	50 µL	75 µL	100 µL
5 nm	1.6E+04	8.1E+03	5.4E+03	4.0E+03
10 nm	1.5E+05	7.4E+04	4.9E+04	3.7E+04
20 nm	1.4E+06	6.8E+05	4.5E+05	3.4E+05
30 nm	4.9E+06	2.5E+06	1.6E+06	1.2E+06

The data from the ISS K2 spectrofluorometer was analyzed with Vinci program. The operation mode of spectrofluorometer was photon-counting mode in steady state. The excitation wavelength was set at 340nm to excite laurdan and the emission intensities from the samples were recorded from 360nm to 500nm. Vinci program provides the data of Emission Intensity

(a.u.) and Emission Wavelength (nm) in a tabulated format. Figure 2.12 and Figure 2.13 represent the sample data plots of emission intensities vs. wavelength for various size and concentration AuNP treatments of extruded and non-extruded DMPC vesicles from Vinci program.

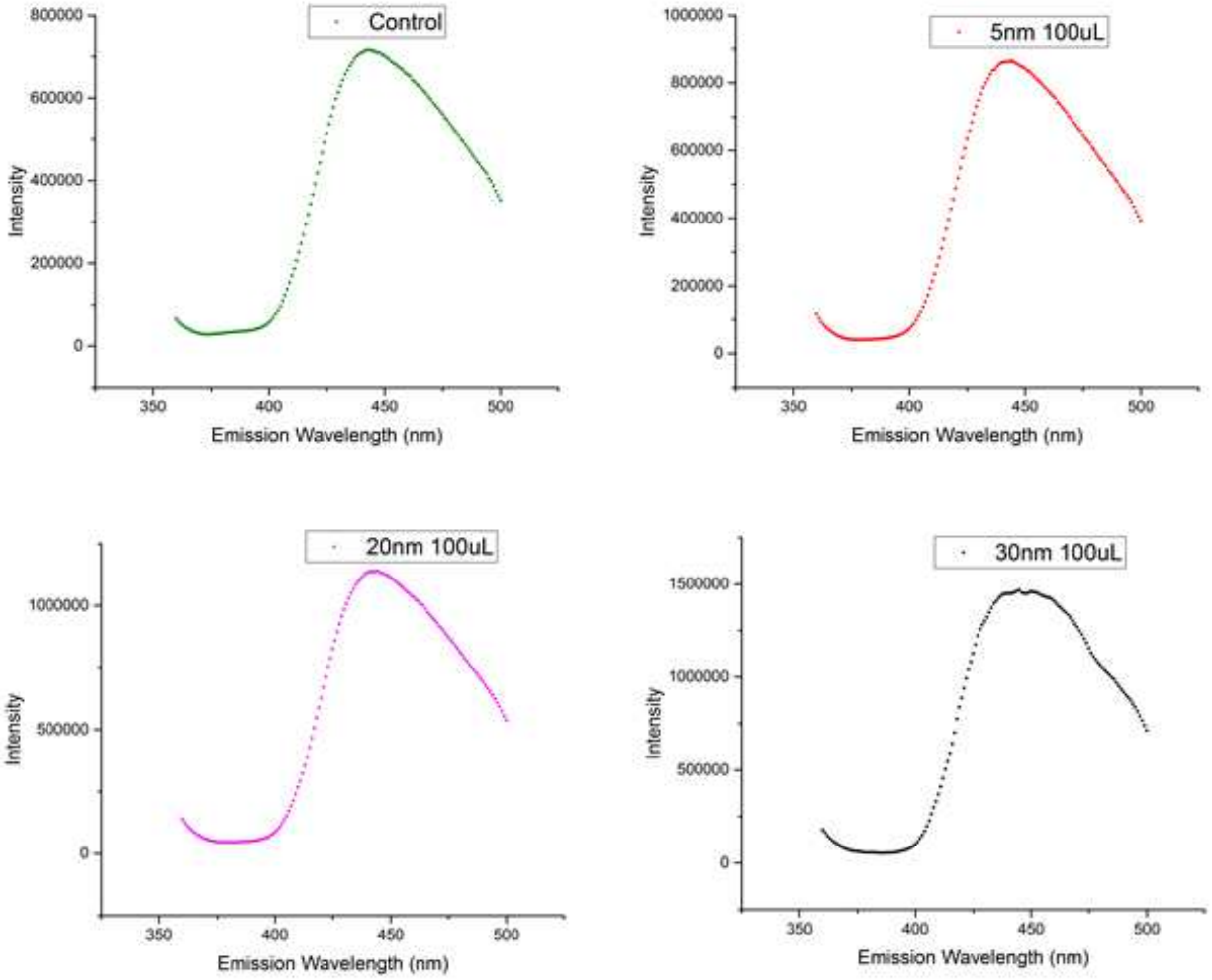

Figure 2.12: Sample raw data plots of emission intensities vs. wavelength for Control and AuNP treatment of extruded DMPC vesicles from Vinci program for spectrofluorometric analysis.

The intensity vs. emission wavelength plots for control and AuNP treated extruded DMPC vesicles in Figure 2.12 show a peak in the intensity at 440nm for each of the plots which trails off at 490 nm. Compared with Figure 2.13, which represents the intensity vs. emission wavelength plots for control and AuNP treated non-extruded DMPC vesicles, the trailing off in the intensities post 440nm is less steep giving the curves a raised shoulder kind of appearance. The peaks in the intensity vs. emission wavelength plots in Figure 2.13 occur around 440nm.

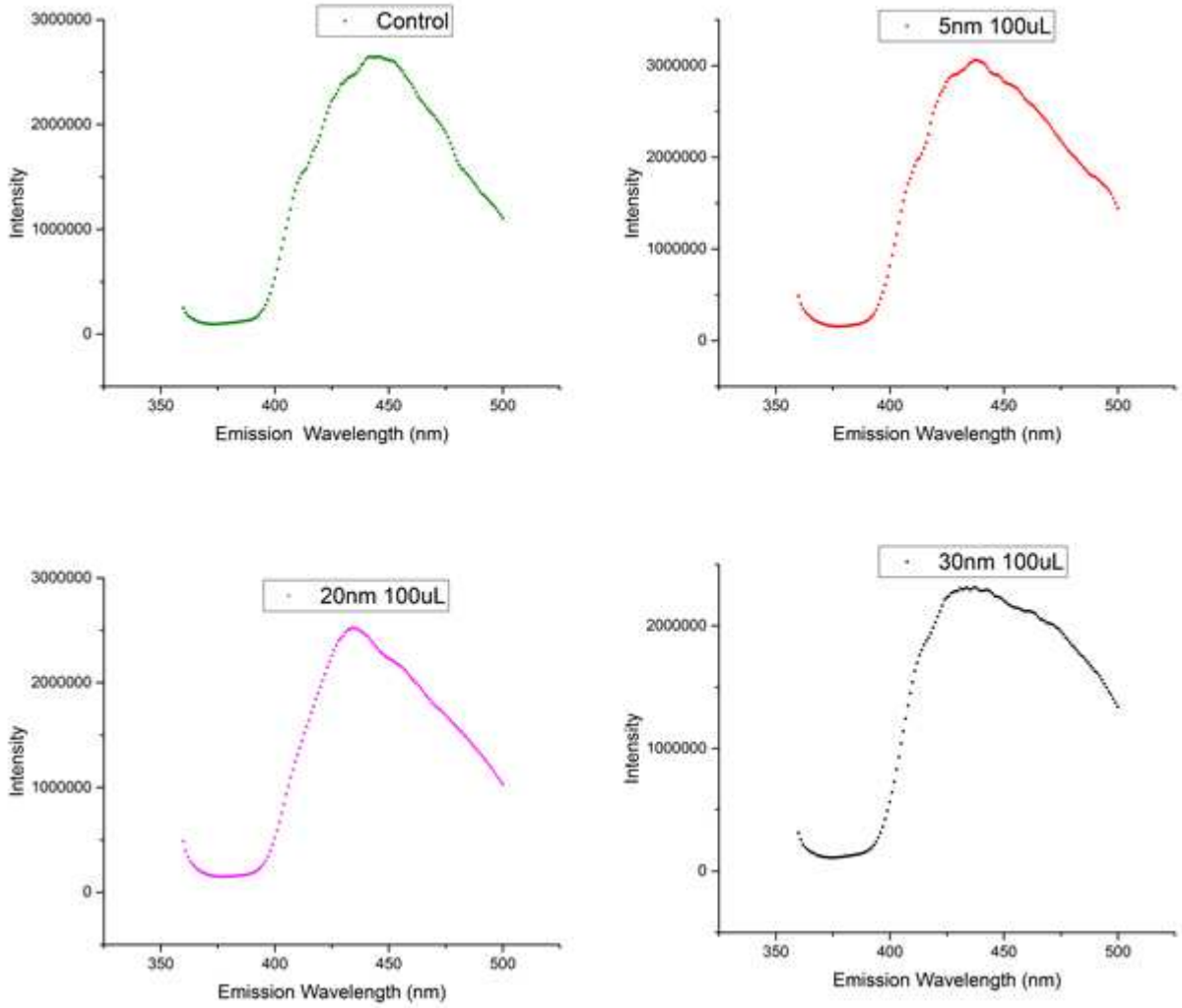

Figure 2.13: Sample data plots of emission intensities vs. wavelength for Control and AuNP treatment of non-extruded DMPC vesicles from Vinci program for spectrofluorometric analysis.

The GP value for each of Control and AuNP treated extruded (Figure 2.12)/ non-extruded (Figure 2.13) DMPC vesicle was calculated from the emission intensities obtained from spectrofluorometric analysis, using the formula (2.1):

$$\mathrm{GP} = \frac{I_{440} - I_{490}}{I_{440} + I_{490}}$$

The %GP changes with respect to the Control were then calculated for each of the AuNP treated DMPC vesicle GP values. Three to four sets of experimental data were collected and the averages of %GP values were calculated which are tabulated in Table 2.3 and Table 2.4.

2.6 Results

The plots of %GP values for AuNP treated DMPC vesicles are shown here.

Table 2.3: Average percent changes in generalized polarization (%GP) for extruded DMPC vesicles

	No AuNP	25 uL	50 uL	75 uL	100 uL
5-nm AuNPs	0	24	9	23	33
10-nm AuNPs	0	49	3	–12	4
20-nm AuNPs	0	12	–8	–8	20
30-nm AuNPs	0	50	18	55	49

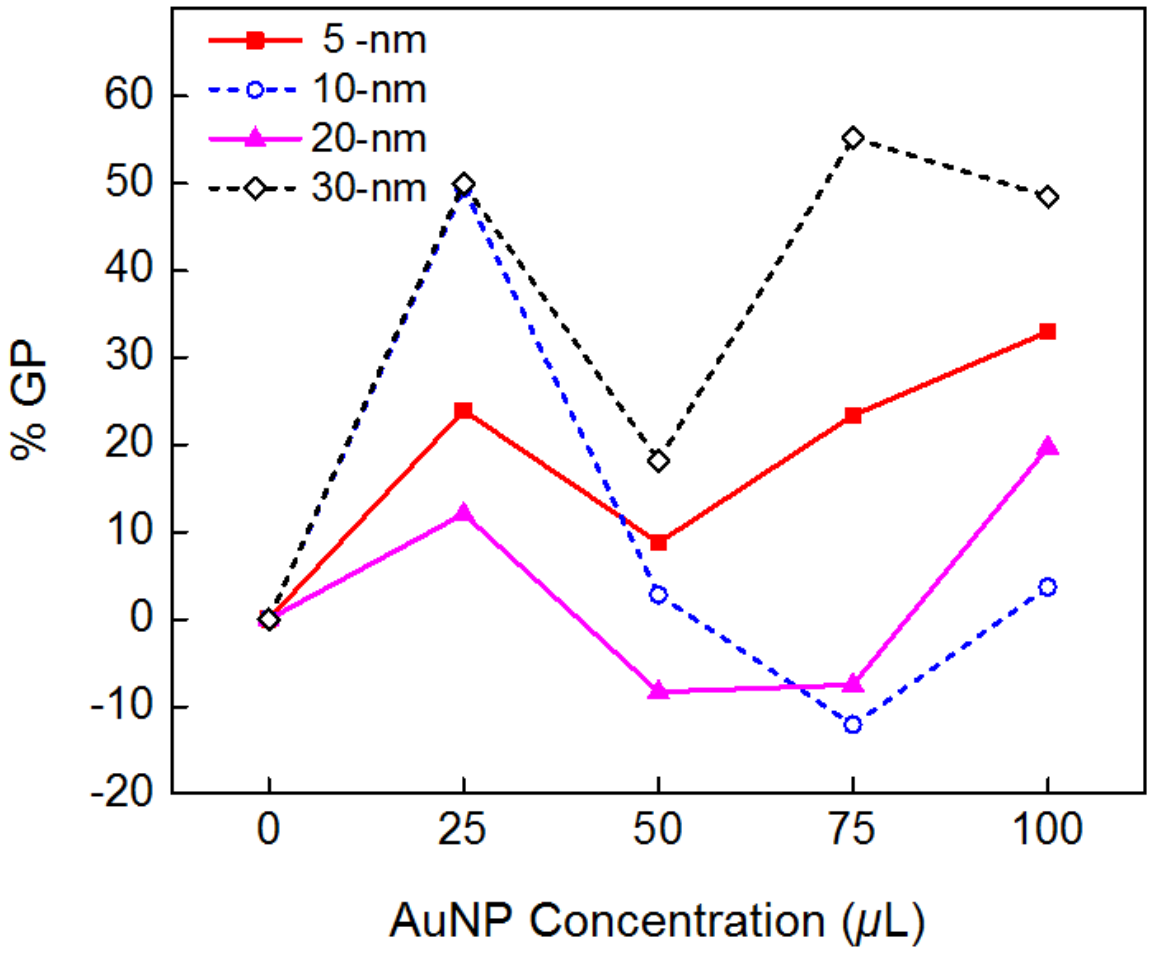

Figure 2.14: Percent changes in generalized polarization (%GP) of control lipid vesicles vs. treatment of various sizes and concentrations of AuNPs for extruded DMPC vesicles. The averages of three independent experiments for each size and concentration combination were plotted in the graphs.

Table 2.4: Average percent changes in generalized polarization (%GP) for non-extruded DMPC vesicles.

	No AuNP	25 uL	50 uL	75 uL	100 uL
5-nm AuNPs	0	–8	–1	14	–8
10-nm AuNPs	0	–21	–19	–9	–19
20-nm AuNPs	0	–9	–25	–16	–14
30-nm AuNPs	0	–16	–30	–20	–19

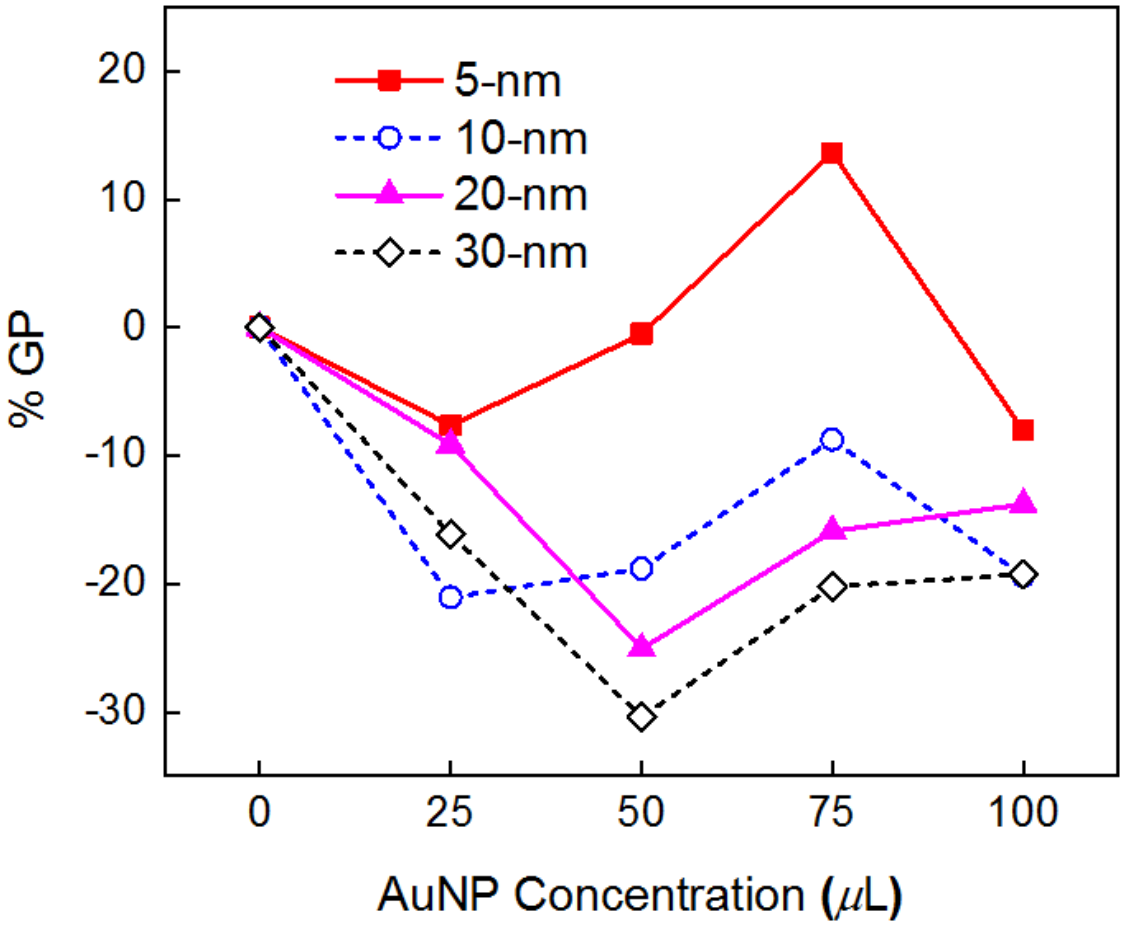

Figure 2.15: Percent changes in generalized polarization (%GP) of control DMPC vesicles vs. treatment of various sizes and concentrations of AuNPs for non-extruded DMPC vesicles. The averages of four independent experiments for each size and concentration combination were plotted in the graphs.

2.7 Discussions & conclusion

AuNPs affect the lipid packing which relates to the fluidity of the vesicles. Laurdan labeled vesicles were treated with different sized AuNPs and the %GP values were recorded.

The graphs of %GP changes of AuNP-treated extruded lipid vesicles from the control are shown in Figure 2.14. The averages of three independent experiments for each size and concentration combination were plotted in the graphs. Positive %GP changes are found for most cases except for 20-nm AuNPs at 50 μL and 75 μL and 10nm AuNP at 75 μL respectively. The highest %GP was recorded at 55% for 30nm AuNP at 75 μL concentration while the lowest %GP was at -12 for 75 μL of 10nm AuNP. A definite relation between the %GP values and size of AuNPs could not be established because of the variations in values. Positive %GP values indicate a transition towards gel phase, suggesting that AuNPs tend to make extruded vesicles more orderly packed.

The graphs of %GP changes of AuNP-treated non-extruded lipid vesicles from the control are shown in Figure 2.15. The averages of four independent experiments for each size and concentration combination were plotted in the graphs. Note that a negative %GP change suggests a transition toward fluid phase. Negative %GP changes are found for almost all cases except for 5-nm AuNPs at 75 μL, suggesting that AuNPs tend to make as-prepared lipid vesicles more fluidic or disorderly packed. In particular, the most pronounced GP change of −30% occurred with 30-nm AuNPs at 50 μL and the highest positive %GP change of +14% was found with 5-nm AuNPs at 75μL. Given the variability in size distribution of lipid vesicles among different batch of preparations, conclusions can be drawn here that AuNPs from 5 to 30 nm tend to make as-prepared lipid vesicles more fluidic and larger AuNPs (greater than 5 nm) impact the lipid packing more effectively than 5-nm AuNPs as seen in the data. The fluidization increases lipid

vesicle surface area because the head groups of lipids lose the triangular lattice order and adopt a more disordered arrangement with increased inter-molecular spacing [75] as shown in Figure 2.16.

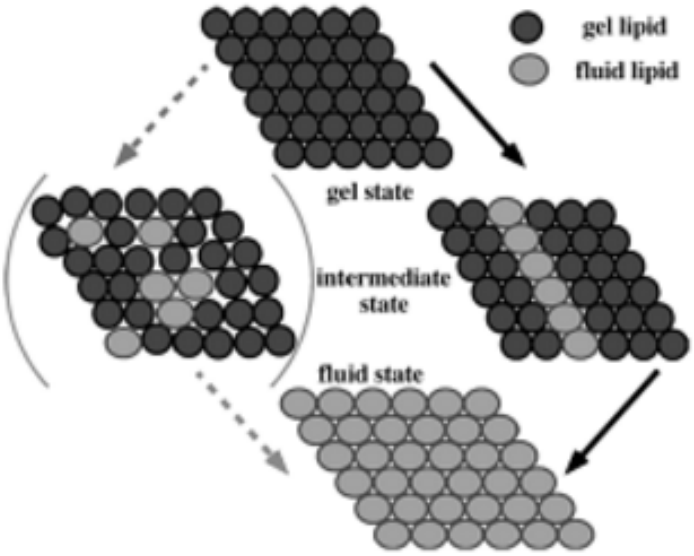

Figure 2.16: Lipids in the gel phase adopt a crystalline triangular packing. Fluidization increases lipid vesicle surface area and the head group of lipids lose the triangular lattice order and adopt a disordered arrangement with increased inter-molecular spacing [77]

An increased surface area with a given volume should undergo a shape change from sphere to oblong because volume-to-surface ratio decreases [76-77]. An example is provided with an ellipsoid in Figure 2.17 and the volume and surface area of the ellipsoid in Table 2.5

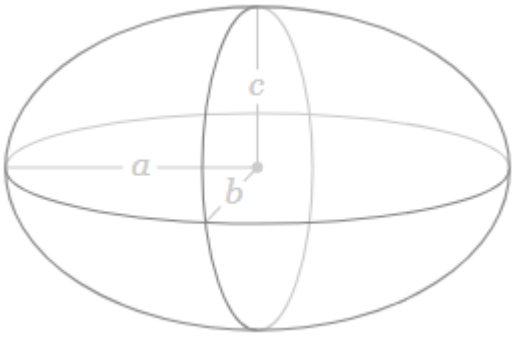

Figure 2.17: Ellipsoid with dimensions a, b and c

Volume of the ellipsoid is calculated as

$$V = \frac{4}{3}\,\pi\, abc$$

The Surface area can be calculated from

$$S = 4\pi \left(\frac{(ab)^{1.6} + (ac)^{1.6} + (bc)^{1.6}}{3}\right)^{1/1.6}$$

Table 2.5: Effect of variation in dimensions of an ellipsoid on its shape with a fixed volume

a	b	c	Volume (V)	Surface Area (S)	V/S
1	1	1	4.19	12.57	0.33
2	1	0.5	4.19	15.88	0.26
3	1	0.33	4.19	21.28	0.2
4	1	0.25	4.19	27.16	0.15

The calculations of volume and surface area provided in Table 2.5 indicate that a sphere has a maximum volume to surface area ratio. Keeping volume fixed at 4.19 cubic units, as the surface area is increased, the volume to surface area ratio decreases and the ellipsoid develops elongated or oblong shape.

To test the hypothesis of fluidization-led-to shape changes, DMPC vesicle circularity analysis was conducted at 100 μL AuNP treatment for different sizes, which will be discussed in the next chapter.

CHAPTER III

CIRCULARITY CHANGES OF LIPID VESICLES INDUCED BY GOLD NANOPARTICLES

As seen earlier, the citrate stabilized AuNPs from 5 to 30 nm generally increase the fluidity of non-extruded DMPC vesicles as found in fluorescence shifts of laurdan. The increased fluidity leads to an increased surface area, which results in lipid vesicle shape changes from circular to less circular shapes in order to accommodate the increased inter-molecular spacing in lipids. The study discussed in this chapter involves the use of a fluorescence microscope Olympus IX-71 to record the images and analysis of the images with ImageJ software.

3.1 Fluorescence microscopy

Fluorescence is a type of luminescence, which occurs in gas, liquid or solid chemical systems when an atom or molecule relaxes through vibrational relaxation to its ground state. It is brought about by absorption of photons in the singlet ground state promoted to a singlet-excited state. As the excited molecule returns to the ground state, it involves the emission of a photon of lower energy, which corresponds to a longer wavelength than the absorbed photon. Early investigations in the 19th century showed that many substances, organic and inorganic compounds, fluoresced when irradiated with ultraviolet light [78-81]. However, it was not until the 1930s that the use of fluorophore was initiated in biological investigations to stain tissue components, bacteria, and other pathogens. Fluorescence microscopy was developed by August Köhler and Henry Siedentopf at Carl Zeiss AG in Jena, Germany around 1908. The sample or individual structures for use in a fluorescent microscope are labeled with a fluorescent dye (fluorophore) and this dye is excited by irradiating light of a certain wavelength matching its

absorption peak. Then it emits light of defined spectral distribution as according to its molecular structure and the environment. The amount of fluorescence emitted by a stained specimen is influenced by a number of factors. These include 1) the fluorophore concentration within stained sections of the specimen, and the thickness of the specimen; 2) the extinction coefficient of the fluorophore; 3) the quantum efficiency of the fluorophore; 4) mean luminous intensity of the light source; 5) fluorescence lifetime; and6) the amount of stained material actually present within the field of view of the microscope. The efficiency with which the fluorophore absorbs the excitation light is known as the extinction coefficient. A greater extinction coefficient increases the possibility of light absorption in a given wavelength region which is a prerequisite to ensuing fluorescence emission. Although many of the fluorophores have high extinction coefficients at peak excitation wavelengths, practical sample preparation techniques often limit the maximum concentration allowed in the sample, thus reducing the overall amount of light actually absorbed by the stained specimen. The quantum efficiency, which is the ratio of emitted fluorescence to light energy absorbed, determines how much of this absorbed light energy will be converted to fluorescence. Usually fluorophores have quantum efficiency between 0.1 and 0.9, but the actual value can be reduced by quenching processes such as photobleaching. The localized environment surrounding the fluorophore plays a paramount role in determining the characteristics of fluorescence emission. Variables such as solvent viscosity, ionic concentrations, pH, and hydrophobicity in the environment can have profound effects on both the fluorescence intensity and the lifetime of the excited state. The combination of these factors, in addition to the fact that many specimens have very small amounts of stained material in the observed field of view, gives a ratio of emitted fluorescence intensity to excitation light intensity in a typical application of between 10^{-4} (for highly fluorescent samples) and 10^{-6}. It is important,

in view of low emission intensities, that the light source chosen for excitation is of sufficient brightness so that the relatively weak emission light can be maximized and that fluorophores of satisfactory absorption and quantum efficiency be chosen.

The basic function of a fluorescence microscope is to irradiate the specimen with a desired and specific band of wavelengths, and then to separate the much weaker emitted fluorescence from the excitation light. The separation of excitation and emission wavelengths is achieved by the proper selection of filters to block or pass specific wavelengths of the spectrum. The design of fluorescence illuminators is based on control of excitation light and emission light by readily changeable filter insertions into the light path on the way toward the specimen and then emanating from the specimen. In a well configured microscope, only the emission light should reach the eye or detector so that the resulting fluorescent structures are superimposed with high contrast against a very dark (or black) background. The limits of detection are generally governed by the darkness of the background, and the excitation light is typically several hundred thousand to a million times brighter than the emitted fluorescence. Illustrated in Figure 3.1, is a simplified diagram of a modern fluorescence microscope equipped for both transmitted and reflected fluorescence microscopy. The illuminator has the light source positioned at one end and the filter cube turret at the other. Usually mercury vapor lamp is used because it emits very bright light at several discrete wavelengths. The design consists of a basic reflected light microscope in which the wavelength of the reflected light is longer than that of the excitation. In a fluorescence microscope, light of a specific wavelength (or defined band of wavelengths), often in the ultraviolet, blue or green regions of the visible spectrum, is produced by passing multispectral light from an arc-discharge lamp or other source through a wavelength selective excitation filter.

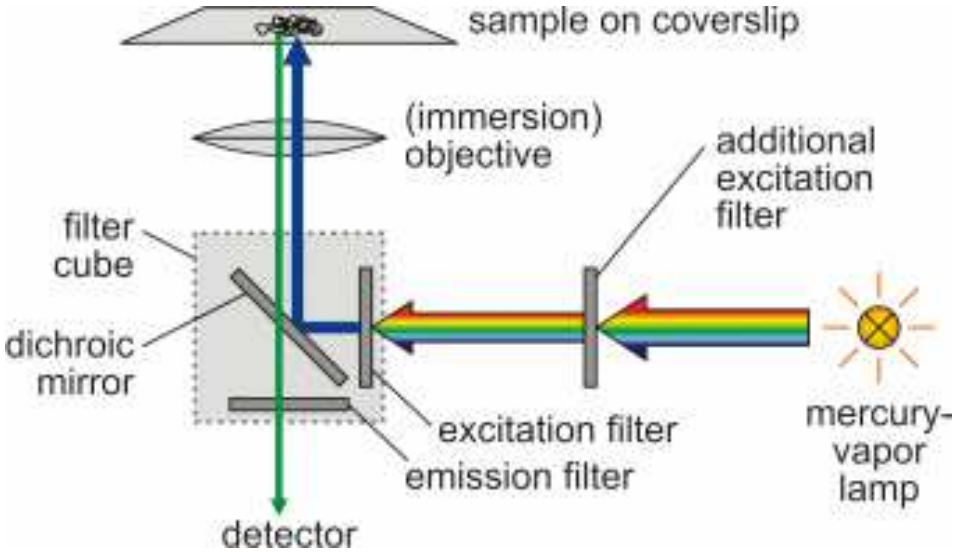

Figure 3.1: Basic schematic of a fluorescence microscope

Wavelengths passed by the excitation filter reflect from the surface of a dichromatic (also termed a dichroic) mirror or beam splitter, through the microscope objective to bath the specimen with intense light. If the specimen fluoresces, the emission light gathered by the objective passes back through the dichromatic mirror and is subsequently filtered by a barrier (or emission) filter, which blocks the unwanted excitation wavelengths. It is important to note that fluorescence is the only mode in optical microscopy where the specimen, subsequent to excitation, produces its own light. The emitted light re-radiates spherically in all directions, regardless of the excitation light source direction. An oil immersion objective is normally included for higher magnification. Olympus IX71 inverted microscope was employed for this study. It was setup for brightfield imaging with fluorescence. The microscope was provided with a mercury lamp illuminator and motorized stage and zoom. Since the excitation wavelength of laurdan is 340nm and its emission range is 360-500nm, the DAPI channel was utilized for observation of images. MetaMorph software was used for acquiring and processing images and graphic functions as well as archiving and retrieving images.

3.2 ImageJ software

ImageJ is an open source program developed at National Institutes of Health. It is designed as a scientific multidimensional image processing tool with a wide range of functionalities. ImageJ can acquire, display, edit, enhance, analyze, process, save, and print 8-bit color and grayscale, 16-bit integer and 32-bit floating point images. It can read many image file formats, including TIFF, PNG, GIF, JPEG, BMP, DICOM and FITS, as well as raw formats. ImageJ supports image stacks, a series of images that share a single window, and it is multithreaded, so time-consuming operations can be performed in parallel on multi-CPU hardware. Spatial calibration is supported to provide real world area and length measurements. Density calibration can be done against radiation or optical density standards using user specified units. ImageJ can calculate area, mean, perimeter, circularity and pixel value statistics of user-defined selections of objects based on intensity threshold. It also performs automated particle analysis and provides tools for measuring path lengths and angles. It can create density histograms and line profile plots. It supports standard image processing functions such as logical and arithmetical operations between images, contrast manipulation, density profiling, convolution, Fourier analysis, sharpening, smoothing, edge detection and median filtering. A tool palette supports editing of color and gray scale images, including the ability to draw lines, rectangles and text. All editing, filtering, and measurement functions operate at any level of magnification and are undoable. It does geometric transformations such as scaling, rotation, inversion and flips. The program supports any number of images simultaneously, limited only by available memory [82-85].

3.3 Experimentation

Laurdan-labeled DMPC vesicles were prepared using the protocol mentioned in section 2.5. We then mixed 25 μL of DMPC vesicles with 100 μL AuNPs (prepared by citrate reduction

and stabilized in 0.1 mM PBS, Sigma-Aldrich) of various sizes (5, 10, 20, 30 nm) and incubated the samples for 2 hours. About 1-2µL of each incubated sample was dropped on a glass slide and covered with a coverslip. Thereafter the slide was mounted on the stage of the Olympus IX-71 inverted fluorescence microscope. Multiple fluorescence images of laurdan-labeled DMPC vesicles were recorded in the DAPI channel to match the excitation and emission spectra for laurdan. The size and circularity analysis were performed on the recorded images with ImageJ program (NIH). Circularity, calculated as $\frac{4\pi(Area)}{(Perimeter)^2}$, is two-dimensional tolerance which controls the overall form of the circle ensuring that it is not too oblong or out of round. It is a measure of how circular each particle is. Particles in ImageJ are modelled as ellipses. An ellipse with a circularity of 0 is a straight line, while a circularity of 1 represents a perfect circle.

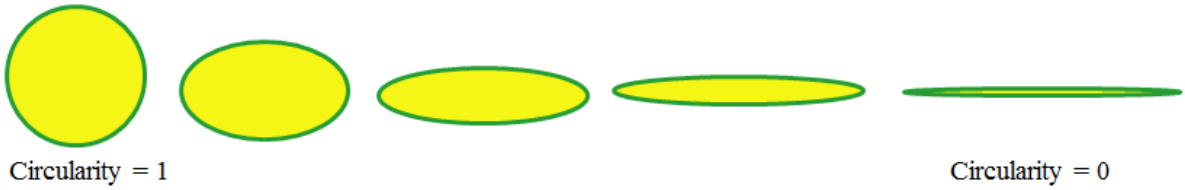

Following instructions were followed for the particle analysis in ImageJ.

i) Laurdan labeled DMPC vesicles with AuNPs image was opened in ImageJ and the brightness, contrast and sharpness was adjusted.

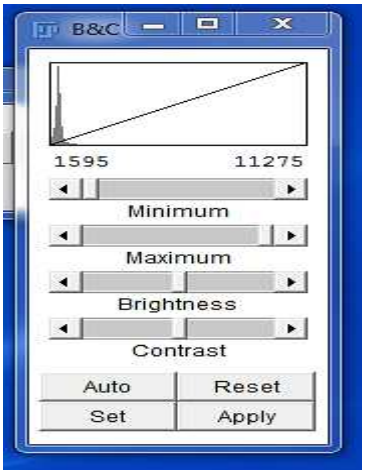

ii) The image scale was adjusted with respect to the magnification of the microscope Olympus IX-71. The pixel aspect ratio was selected to 1

Magnification	**Pixel**	***μ*m**
20X	1	0.8
40X	1	0.4
60X	1	0.26
100X	1	0.16

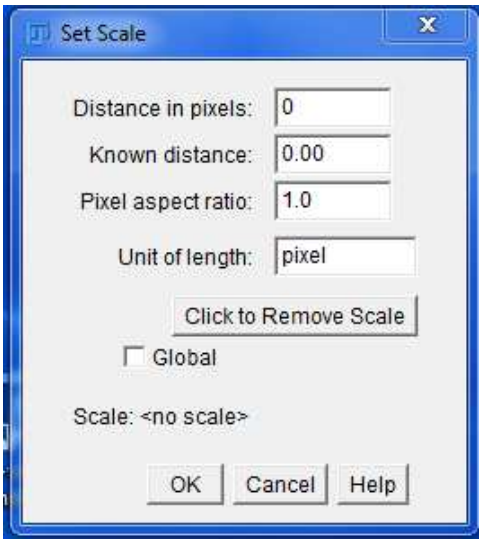

iii) Threshold levels of the image were set to isolate the particles from the background illumination.

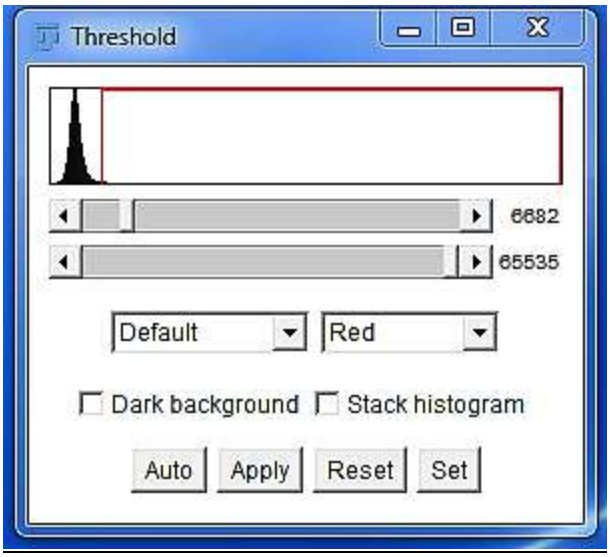

iv) Particles in the image were analyzed with the preset conditions of size (μm^2) and circularity. The pixel range for area included in the analysis is 6 to 500, which corresponds to particle diameter range from 1µm to 10 µm. Pixel area beyond the range was discarded in the analysis

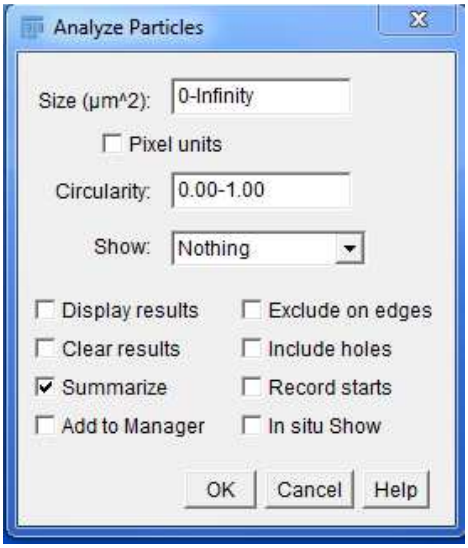

v) ImageJ summarizes the results of the particle analysis in terms of the particle count, the total area, the average size of the particles, % area, mean circularity and mean roundness.

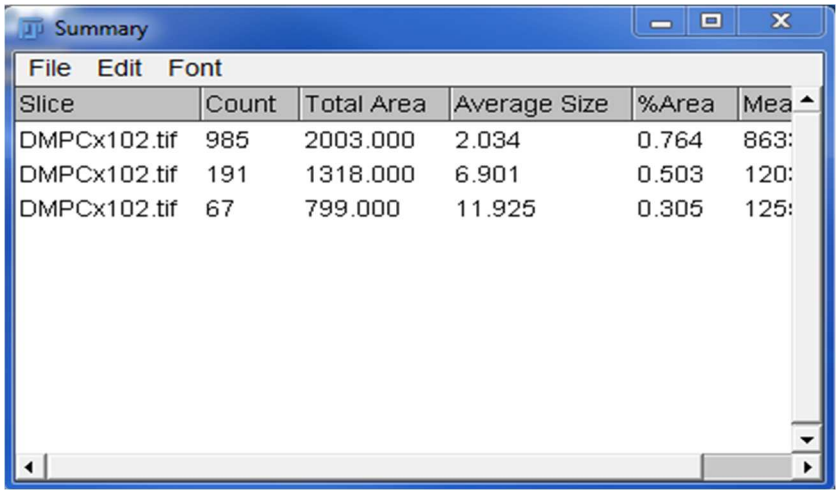

10 image files, each containing 20-30 particles, for Control (no AuNPs), 5nm, 10nm, 20nm, 30nm size AuNPs were analyzed. The results summarized by ImageJ were processed further in Excel to provide the mean circularity values and the distribution of circularity for liposomes in specific ranges, which is tabulated below.

3.4 Results

Table 3.1: Mean circularity values of AuNP induced DMPC vesicles analyzed by ImageJ from an average of about 250 particles per AuNP size. Lipid vesicles not treated with AuNPs (control) presented the highest mean circularity value of 0.92 and vesicles treated with 10nm AuNPs showed the lowest mean circularity value of 0.77, indicating that 10nm AuNPs induced a major change in circularity of the DMPC vesicles.

Size of AuNPs	Mean circularity
Control	0.92
5nm	0.90
10nm	0.77
20nm	0.88
30nm	0.82

Table 3.2: Range of circularity distribution for AuNP induced DMPC vesicles analyzed by ImageJ from an average of about 250 particles per AuNP size. Lipid vesicles treated with 10nm AuNPs showed 21% having a low circularity range 0-0.5, followed by 30nm AuNP. This is another way to show that 10nm AuNPs induced the highest circularity changes in DMPC vesicles.

Range	Control (%)	5 nm (%)	10 nm (%)	20 nm (%)	30 nm (%)
0 - 0.5	2	3	21	6	17
0.5 - 0.8	12	14	18	18	14
0.8 - 1	86	83	61	76	69

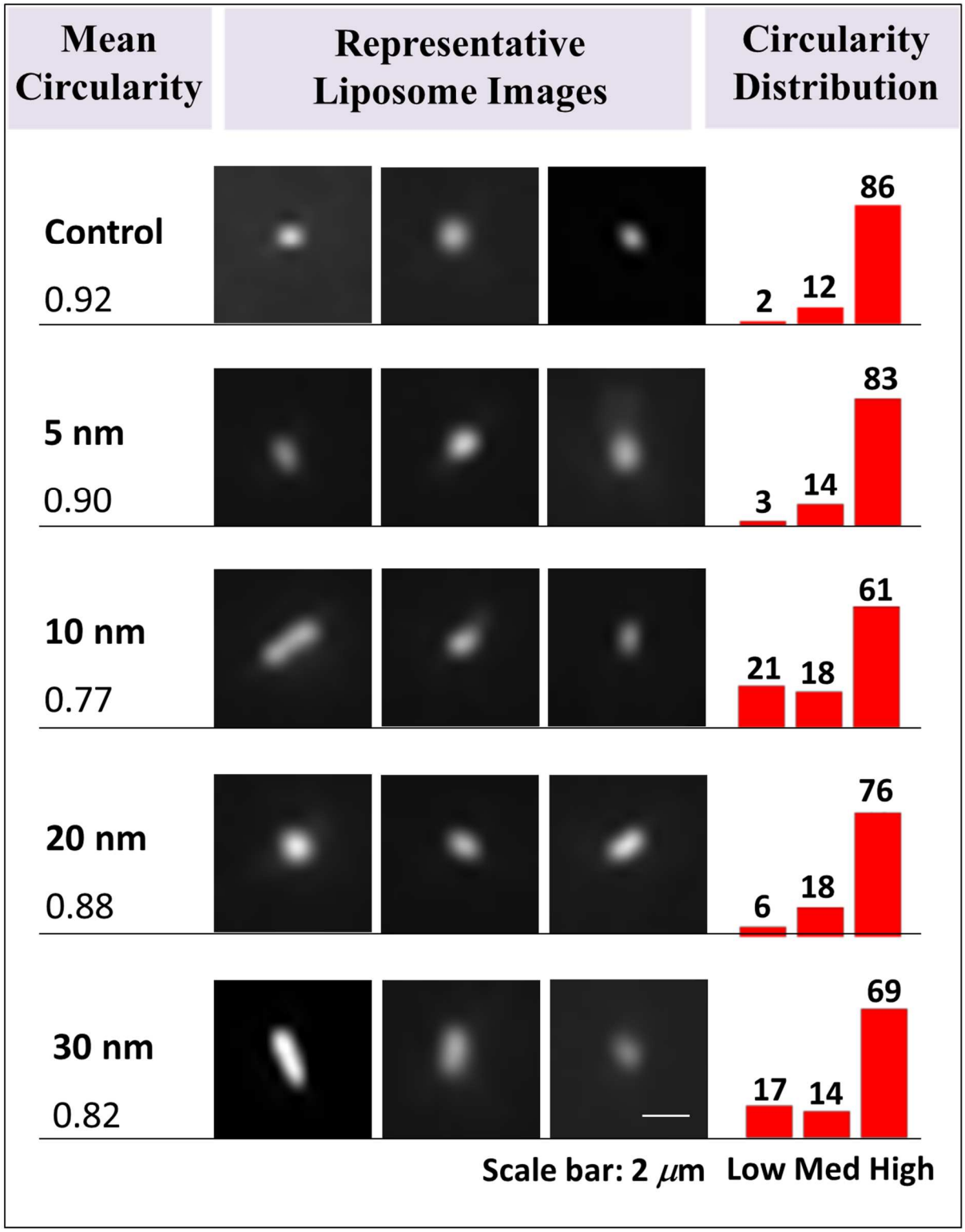

Figure 3.2: Representative fluorescence images of laurdan labeled DMPC vesicles under various AuNP treatments (center). The mean values of circularity (left). The histograms of percent populations for low (0-0.5), medium (0.5-0.8), and high (0.8-1) circularities (right).

3.5 Conclusion

Figure 3.2 shows the representative fluorescence images of laurdan-labeled DMPC vesicles treated with different size AuNPs juxtaposed with the histograms of percent populations for liposomes of low (0-0.5), medium (0.5-0.8), and high (0.8-1) circularities. The vesicles without AuNPs have 86% high-circularity population, the greatest among all analyzed. Rod-like lipid vesicles were found frequently with 10 and 30-nm AuNP treatment, as evidenced by much greater low-circularity population of 21% and 17% respectively. Consequently, the mean circularities from 10 and 30-nm AuNPs registered the lowest values of 0.77 and 0.82. In Figure 2.11 at 100 μL, 10 and 30-nm AuNPs induced greatest negative %GP changes of −22% and −20%, followed by 20-nm AuNPs of −14% and 5-nm of −13%. The mean circularities followed the exact same order of %GP changes with 10, 30, 20, 5-nm AuNPs and control, corresponding to 0.77, 0.82, 0.88, 0.90, and 0.92 respectively.

It has been observed that AuNPs from 5 to 30 nm generally increase the fluidity of as-prepared DMPC vesicles as found in fluorescence shifts of laurdan. The increased fluidity leads to an increased surface area, which results in vesicle shape changes from circular to less circular, as confirmed in fluorescence images. The total agreement between %GP changes and mean circularities supports the aforementioned hypothesis that AuNP-induced membrane fluidization leads to less circular lipid vesicles.

CHAPTER IV

PORE FORMATION ON LIPID VESICLES INDUCED BY GOLD NANOPARTICLES

The nonspecific adsorption of charged nanoparticles onto the single-component phospholipid bilayer and the disruption of lipid bilayers have been observed previously [86]. Theoretical and experimental studies have shown that negatively charged AuNPs can disrupt zwitterionic membranes and form nanoscale "holes" or "pores" on lipid bilayers [87-89]. The formation of pores in supported lipid bilayers was previously observed for various macromolecules such as peptides, proteins, and nanoparticles including polymers, AuNPs, and silica nanoparticles [90-91]. By means of the atomic force microscopy (AFM) techniques, the surface topography of the bilayer lipid membranes composed of DMPC with incorporated AuNPs was studied. The basic principle of this method is to indent the lipid bilayer with an AFM tip of selected geometry and measure the applied force from the bending of the AFM cantilever. Fitting the force-indentation curve to the Hertz model for the corresponding tip geometry can give quantitative measurements of mechanical properties of the sample.

The AuNPs used in this work were prepared by citrate reduction of chloroauric acid (HAuCl4) and stabilized in 0.1mM PBS [92]. The citrate capped AuNPs carry negative surface charges as shown in Figure 4.1.

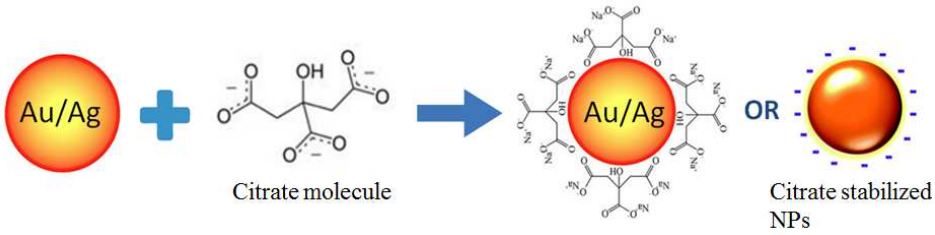

Figure 4.1: Negative surface charges on citrate stabilized AuNPs [92]

4.1 AFM principle

The AFM is a kind of scanning probe microscope which is designed to measure local properties of the sample such as height, deformation, and elasticity. AFMs operate by measuring the force between a probe and the sample. Normally, an AFM senses the surface with a cantilever which has a very sharp tip (15-40nm end radius) to scan over a sample surface. As the tip approaches the surface, the close-range, attractive force between the surface and the tip cause the cantilever to deflect towards the surface. However, as the cantilever is brought even closer to the surface, such that the tip makes contact with it, increasingly repulsive force takes over and causes the cantilever to deflect away from the surface.

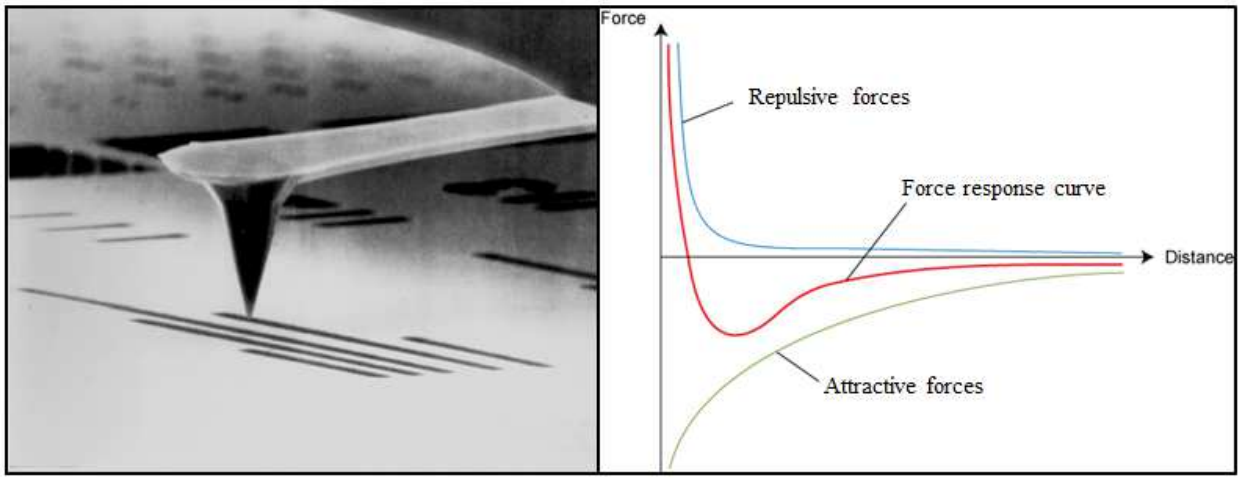

Figure 4.2: AFM Cantilever Tip (left) and Force Curve (right). An AFM uses a cantilever with a very sharp tip to scan over a sample surface. As the tip approaches the surface, the close-range, attractive forces between the surface and the tip cause the cantilever to deflect towards the surface. However, as the cantilever is brought even closer to the surface, until the tip makes contact with it, increasingly repulsive forces takes over and causes the cantilever to deflect away from the surface [93].

The deflections of the cantilever, either towards or away from the surface, can be detected by using an optical lever. The optical lever operates by reflecting a laser beam off the flat top of the cantilever. Any cantilever deflection will cause slight changes in the direction of the reflected beam. A position-sensitive photo diode (PSPD) can be used to track these changes. The differences in signals between the segments of the photodetector indicate the position of the

laser spot on the detector and thus the angular deflections of the cantilever. Thus, if an AFM tip passes over a raised surface feature, the resulting cantilever deflection and the subsequent change in direction of reflected beam is recorded by the PSPD.

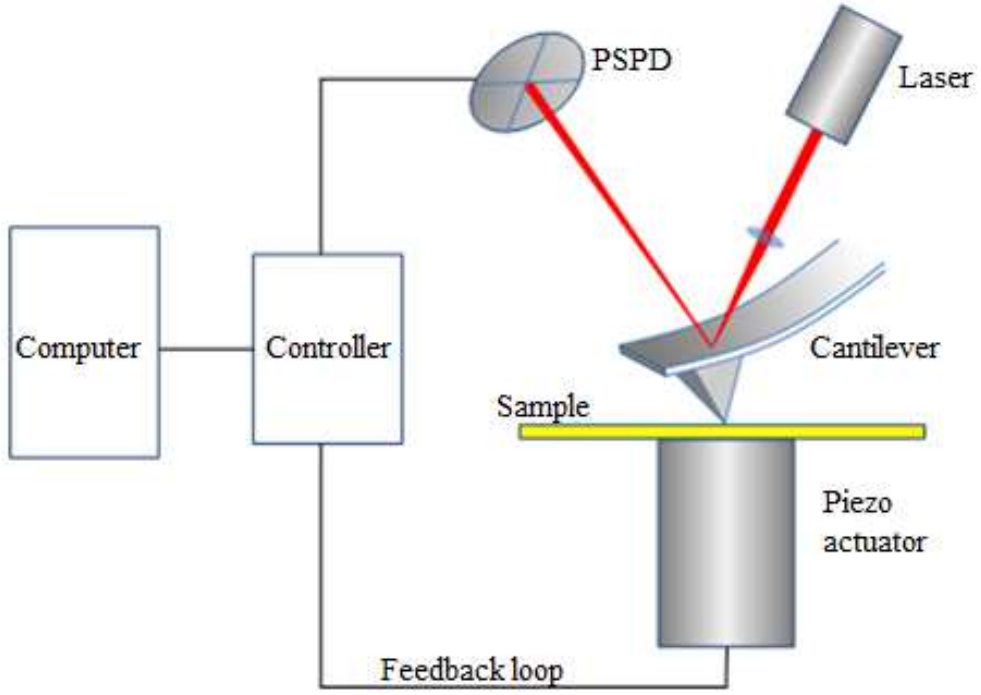

Figure 4.3: Basic schematic of AFM

Illustrated in Figure 4.3 is the schematic of AFM. An AFM images the topography of a sample surface by scanning the cantilever over a region of interest wherein the raised and lowered features on the sample surface influence the deflection of the cantilever, which is monitored by the PSPD. AFM has a feedback loop using the laser deflection to control the force and tip position. As the tip interacts with the surface, the laser position on the photodetector is used in the feedback loop to track the surface for imaging and measuring. By using a feedback loop to control the height of the cantilever tip above the surface thus maintaining a constant laser position, the AFM can generate an accurate topographic map of the surface features [94].

4.2 AFM sample preparation

A multimode AFM (Bruker, CA) was used to image supported lipid bilayers in 1x PBS incubated with AuNPs in a fluid cell. To ensure the formation of single-layer lipid bilayers, as-prepared DMPC liposomes were extruded (Avanti Polar Lipids, Inc.) by passing through a polycarbonate membrane (pore size 0.1 μm) for 11 repeats to remove GUVs. The extruded liposomes enriched in LUVs were then dropped on the freshly cleaved mica to form supported bilayer patches through LUV fusion in 1x PBS. Thereafter, mica surface deposited with DMPC bilayers was carefully mounted in a fluid cell and filled with 1x PBS to ensure that AFM cantilever probes lipid bilayers in liquid. A mixture of AuNPs of various diameters (5 to 50 nm) was later added to the supported bilayers. After 20 minutes of incubation, multimode AFM scans were performed. In determining the mechanical properties, the peak force quantitative nanomechanical (PF-QNM) mode [95-97], which allows for multi-parametric characterizations of bilayer property including thickness, deformation, and Young's modulus, was performed using soft calibrated MSCT cantilever at varying force levels spanning bilayer break-through strength. AuNPs were used for internal tip shape characterization. Multiple force curves were recorded on various spots of lipid bilayers to determine the elastic limit, and the Young's modulus was derived from the Hertz model.

4.2.1 The Hertz model

The Hertz model approximates the sample as an isotropic and linear elastic solid occupying an infinitely extending space. Furthermore, it is assumed that the cantilever tip is not deformable and there are no additional interactions between the tip and the sample.

$$F = \frac{4}{3}\frac{E}{(1-\upsilon^2)}\sqrt{R}\delta^{\frac{3}{2}} \qquad (4.1)$$

The Hertz model is stated in equation 4.1 where F is the force applied by the AFM tip, E is the Young's modulus, ν is the Poisson's ratio of the sample, R is the radius of the tip curvature (5 nm nominal in the experiment), and δ is the indentation generated on the soft sample. For biological samples, Poisson's ratio is generally set to 0.5 (incompressible material like rubber). The data obtained by indentation measurements (force spectroscopy mode) is fit into the Hertz model to determine the Young's modulus.

4.3 Results

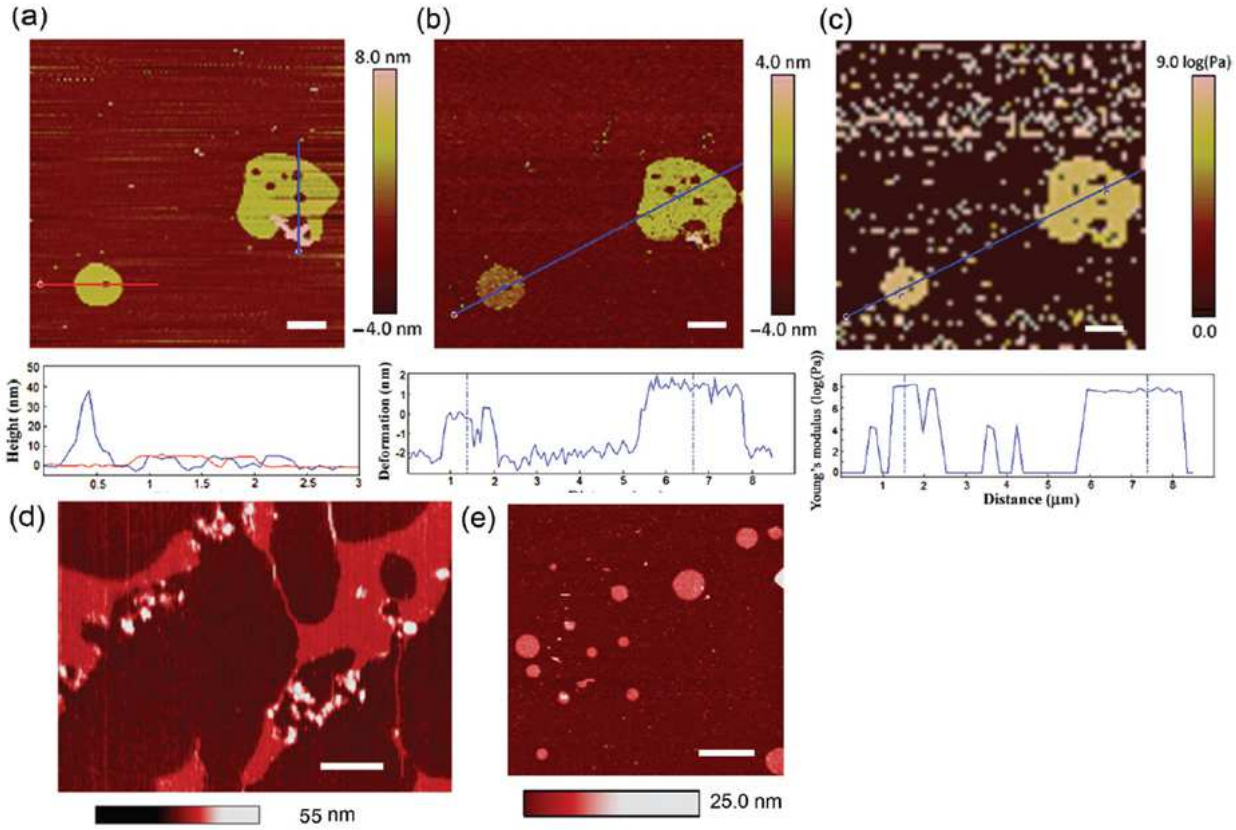

Figure 4.4: (a) The AFM height image of supported DMPC bilayers incubated with AuNPs and imaged at low QNM force of 3.3 nN. The height profiles along two section lines across the big (blue) and small (red) bilayer patches respectively are shown below. (b) The AFM mapping of bilayer deformation at medium QNM force of 6.6 nN and the deformation profile along the section line. (c) Strain-dependent elastic modulus map and the section profile at low QNM force at 0.33–1.5 nN. (d) AFM topographic images of DMPC bilayer disruption by high concentration of AuNPs. (e) AFM topographic image of the DMPC bilayer with a low concentration of AuNPs. Scale bars: 1 μm

4.4 Conclusion

In Figure 4.4(a), the AFM height image of supported DMPC bilayers shows similar AuNP-induced pores. As many as five pores can be seen on the large lipid patch, whereas only one pore is found on the small patch. The diameters of the pores range approximately from 170 to 310 nm. A sizable aggregate of AuNPs in pinkish hue can be found adjoining the lower part of the large lipid patch. These features are confirmed with the height profiles (Figure 4.4(a)): the tall peak at 40 nm features AuNP aggregates; the single lipid bilayer has an average thickness of 6 nm; the pores level with the substrate. In Figure 4.4(b), an average of 3.5-nm deformation was generated on the large lipid patch while approximately 2 nm of deformation was generated on the small lipid patch. The greater indentation generated on the large patch than on the small one is likely a result from a higher density of AuNPs on the large patch (Figure 4.4(a)). This is yet another confirmation that AuNPs make lipid bilayer more fluidic or more elastic. Similar conclusion can be drawn from the Young's modulus image and the section profile in Figure 4.4(c), where the Young's modulus of the large lipid patch is $\sim 10^{7.6}$ Pa versus $\sim 10^{8.0}$ Pa for the small patch. In other words, the stiffness of the small lipid patch is 2.5 times that of the large patch. Higher density of AuNPs has softened the large lipid patch. When the concentration of AuNPs is high, multiple ruptures are found on lipid bilayers (Figure 4.4(d)); when the concentration of AuNPs is low, the lipid bilayers are circular and continuous without holes or ruptures (Figure 4.4(e)). This comparison further confirms the effect of pore formation induced by AuNPs on lipid bilayers.

The adsorbed negatively charged AuNPs have been previously reported to stiffen phosphatidylcholine lipid bilayers at molecular length scale and restructure the bound lipid molecules into a raft-like phase [86]. Combining this and the results above, we hypothesize a localized stiffening and long-range fluidization model, illustrated in Figure 4.5.

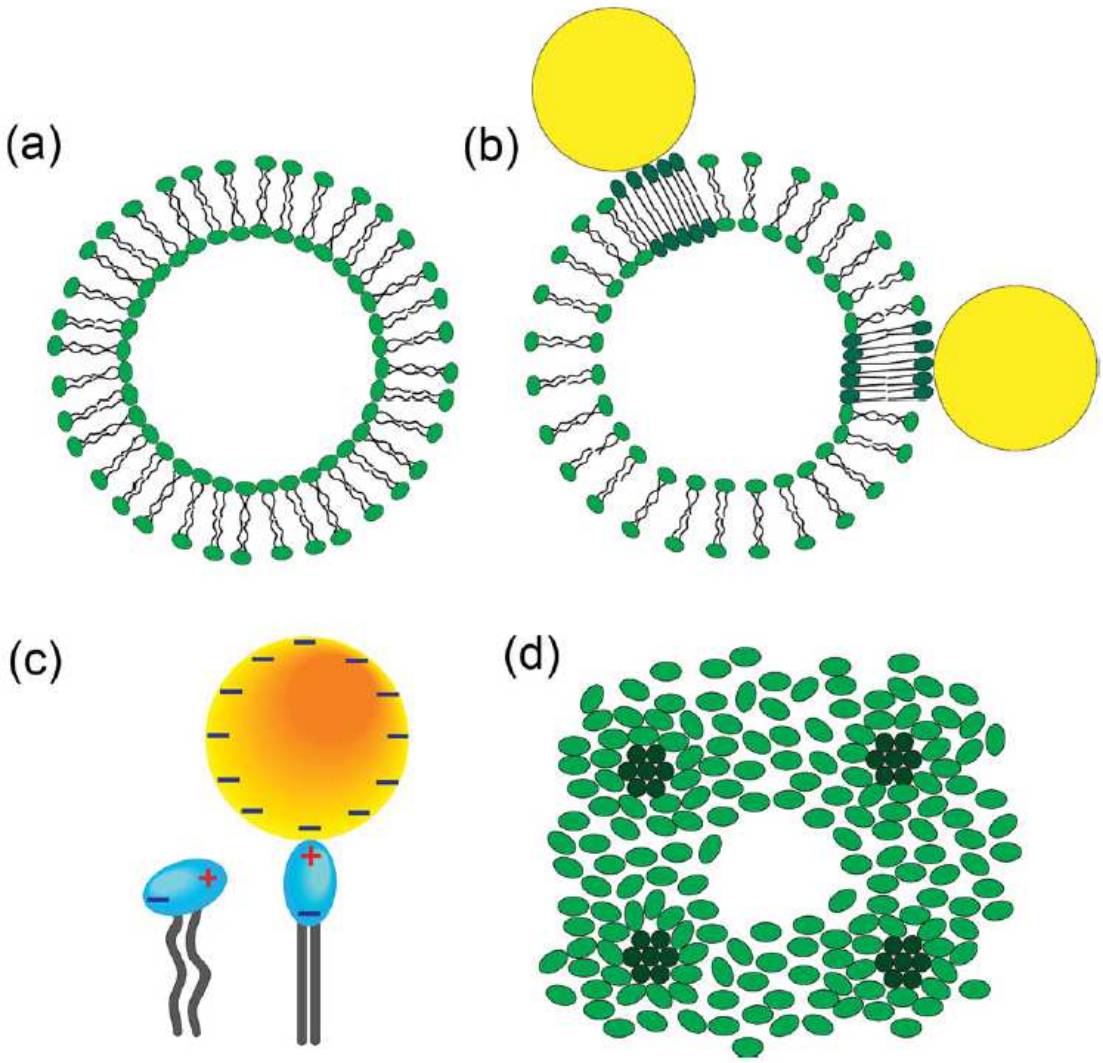

Figure 4.5: The electrostatic forces between lipid head groups and charged AuNPs draw otherwise loosely packed lipid molecules (a) to tightly pack around the binding sites and forming raft-like domains (b). (c) The head group of a DMPC molecule switch from the leaning to the stand-up position under the dipole-charge interaction with a citrate-capped AuNP. (d) A possible top-view of lipid head group arrangement of a pore formed by multiple AuNP adsorptions. Note that the ordered domains (in dark shade) are stressed regions with AuNPs sitting on top but removed for viewing convenience.

First, AuNPs adsorb onto vesicle surfaces through attractive Coulomb potential (Figures 4.5(a) and 4.5(b)). Upon adsorption, the phosphocholine (PC) head group (Figure 2.7) switch from a leaning position to a stand-up position due to dipole-charge interaction (Figure 4.5(c)). The electrostatic forces draw otherwise loosely packed lipid molecules to tightly pack around the

AuNP binding sites, thereby forming raft-like domains (Figure 4.5(b)). As the distance of lipids from adsorbed AuNPs increases, the attractive force decreases. When the lipids are far from the adsorbed AuNPs, the Coulomb attraction is negligible. However, a perturbation arising from stiffened AuNP-adsorbed lipids affects the lipid packing far away. As these lipids have to cover more surface area vacated by AuNP-adsorbed lipids, the lipid-lipid spacing increases, and therefore fluidity increases as observed in %GP and AFM studies.

The raft-like domains of AuNP-bound lipids, on the other hand, should increase the GP value. However, this contribution is rather small and only partially cancels out the GP decrease due to the long-range lipid fluidization. Assuming 100% AuNP adsorption (the actual binding is lower), the ratio of DMPC pairs per AuNP (Table 2.2) ranges from 4×10^3 (5 nm at 100 µl) to 5×10^6 (30 nm at 25 µl), translating into area of unbound lipid bilayer thousands to millions times that of the raft-like AuNP-adsorbed patches. The actual binding determined by adsorption isotherm will be lower than 100%. Therefore, fluidization dominates gelation, leading to an overall increased fluidity as observed. However, when liposomes are more densely adsorbed with AuNPs, more rigidified lipid domains contribute to GP increase, therefore more likely counteracting the long-range GP decrease. That explains one exception of increased GP observed for 5-nm AuNP at 75 µl, the second highest density of AuNP coverage among all tested. Given the variations in AuNP binding and lipid vesicle size distribution from preparation to preparation, it is acceptable that the experiment did not follow exactly the calculation-based trend. Another consequence induced by adsorbed AuNPs is the membrane pore formation, which we consider as a secondary effect of altered lipid packing. We argue that the pores are ruptures resulting from the lateral pressure induced by multiple AuNP adsorptions, [89] rather than from the insertion of AuNPs. A simulation has suggested that a hole is transiently formed before

AuNP entry and closed after AuNP translocation. Also, the insertion of charged AuNPs in this study is not energetically favorable because of the hydrophobic lipid tails. In addition, the pore sizes found on the AFM image (Figure 4.4(a)) range from 170 to 310 nm, much larger than individual AuNPs, making penetration-caused pore formation by single AuNPs unlikely but possible if AuNP concentration is high enough. Figure 4.5(d) illustrates a possible top-view lipid head group arrangement of pore formation. Note that the ordered domains are stressed regions induced by bound AuNPs; however, AuNPs are removed for viewing purpose.

CHAPTER V

HYPERSPECTRAL ANALYSIS BASED ON DARK FIELD MICROSCOPY TO STUDY INTERACTION OF NANOPARTICLES AND LIPID VESICLES

When nanoparticles are exposed to a biological medium, proteins interact with the NP surface creating a layer around it. This layer is called corona and confers to the NPs a new biological identity, which determines the subsequent cellular/tissue response. The composition of the lipid membrane and the type of nanomaterials are important factors, which influence the interaction of NPs with the membrane. Cholesterol is the dominant sterol component in mammal cell membranes regulating the fluidity of the latter. It is known to broaden the main transition between the gel and the liquid crystal phases of lipid bilayers, thereby increasing the order in the high-temperature liquid crystalline phase [98]. The adsorption of nanomaterials on the surface of the membrane modifies the physicochemical properties of the membrane [99]. In a similar way, biomolecules are adsorbed on nanomaterials and result in the formation of a complex such as a protein corona [100]. In this chapter, AuNPs were coated with a protein corona of 10% bovine serum albumin (BSA) to form a complex AuNP-PC. A hyperspectral analysis based on dark-field microscopy was then utilized to assess how AuNPs, AgNPs, AuNP_PC and BSA influence membrane modifications and responses of GUVs characterized by different molar concentration of cholesterol.

5.1 GUVs

Giant unilamellar vesicles (GUVs) have become an intensively used model system because they provide a cell-sized confined volume for the study of biochemical reactions as well as self-assembly processes that occur in the lipid membrane. The size of GUVs, which ranges from 1-

100 µm is one to three orders of magnitude greater than that of SUVs, thus GUVs are well distinguished by commonly used optical methods such as light and fluorescence microscopy. The simplest GUV consists of a spherical lipid bilayer enclosing a buffer. This membrane bound entity mimics three important features of a cell, namely: compartmentalization, finite surface area and bending elasticity of the cellular membranes. GUVs allow optical measurements at the single-vesicle level while tracking membrane integrity, therefore GUVs have been successfully used as a model system to study fundamental membrane thermodynamics, membrane domains and mechanical properties such as membrane curvature, membrane morphology and shape changes [101].

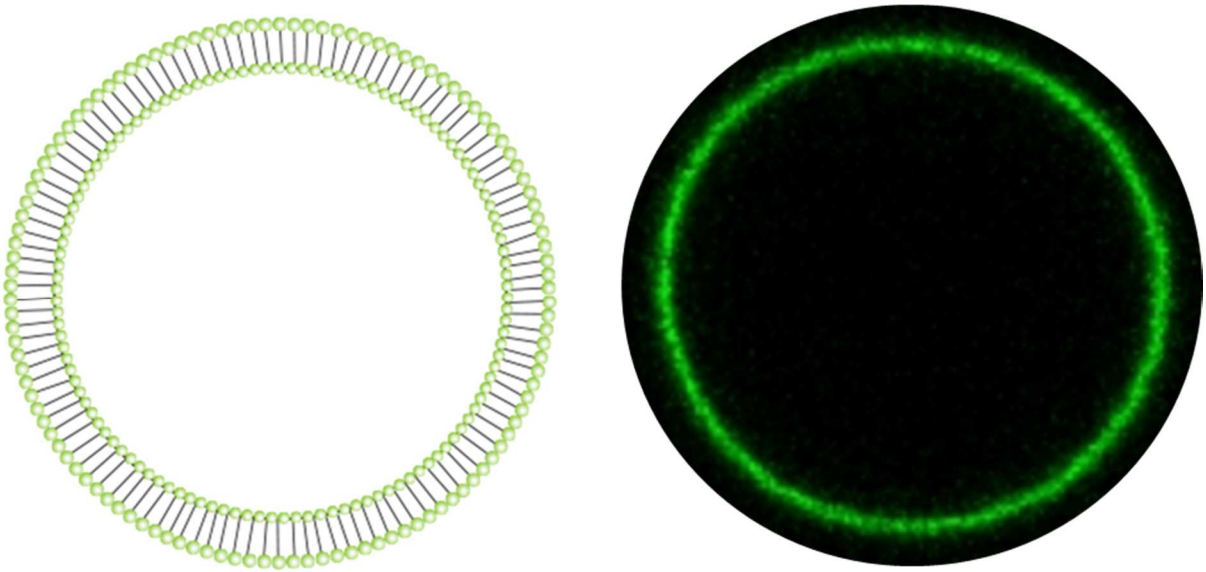

Figure 5.1: Schematic of GUV as a spherical lipid bilayer (left). Confocal image of a GUV (right) [102]

5.1.1 GUV fabrication

Fabrication of GUV involves application of an external electric field for the process of lipid swelling and vesicle formation and this technique is called electroformation. Attempt initiated by application of static (DC) electric field was reported for the first time by Angelova

and Dimitrov (1986) [103]. As found in subsequent experiments, the range of lipid types that form GUVs in DC electric field was rather narrow, perhaps because the static field exerts only an "ordering" effect on lipid molecules. This limitation was overcome by a new experimental approach in which an alternating (AC) electric field was used in GUV formation [104]. The AC field, due to the permanent (usually sinusoidal) change of both direction and magnitude of the field intensity, apart from ordering effect also forces molecules to move, what might help lipids to spontaneously adopt bilayer packing and to form unilamellar structures. This new method enabled the formation of giant vesicles using a variety of lipid mixtures and the study of different properties of their membranes. A few of the underlying mechanisms for the effects of the external electric field on the process of lipid swelling and vesicle formation are mentioned below:

i) Direct electrostatic interactions between electrode and bilayers due to injection of charges from electrodes
ii) Electro osmotically induced mechanical stresses
iii) Electrochemical reactions
iv) Redistribution of double layer counter ions between bilayers
v) Reorientation and lateral redistribution of lipid molecules

Electroformation of GUVs is the method allowing the reproducible production of giant lipid vesicles and therefore is quite often used in laboratories performing studies on model bilayers. In this method lipids solubilized in organic solvents, e.g., a mixture of chloroform and methanol, are deposited on the electrode, dried, and then exposed to an AC field in the presence of a hydrating solvent. It was proposed that mechanical stress induced by the AC field plays a role in separating and destabilizing the membranes to form giant lipid vesicles. The

predominating mechanism of electroformation is the electro-osmotic periodic movement of the water medium at the water electrode interface. These vibrations are directed perpendicular to the electrode surface, where the initial lipid film is deposited, thus pulling lipid lamellae off the electrode and separating them from each other as they grow like “mushrooms”. Vesicles grow in size continuously up to 20 μm. At that stage “mushrooms” start laterally connecting with each other. The zone of contact increases and at a certain moment the AC induced vibrations cause the contact zone to be destabilized, making neighboring “mushrooms” fuse together into a giant one. It takes a few minutes for the resulting “mushroom” to get spherical, close the neck and eventually separate from the electrode. The electro-osmotic vibrations are manifested as mechanical vibrations like those in the sonication of lipid/water dispersions. However, the electro-osmotic agitation is gentler, fine and can be controlled precisely. GUVs used in this researched were prepared with the Vesicle Prep Pro (Nanion Technologies, Germany) apparatus [105].

Figure 5.2: Vesicle Prep Pro apparatus for fabrication of GUVs [105]

The Vesicle Prep Pro is an automated device for preparation of GUVs ranging from 1 – 30 μm in diameter. They are formed by means of electro-swelling (hydration of dry lipid film in an oscillating electric field). The Vesicle Prep Pro offers a standardized and robust way to reliably and reproducibly generate GUVs of homogeneous size distribution with high yields.

The chamber used for vesicle formation consists of two glass cover slides. The slides are coated with indium tin oxide (ITO) turning them into electrodes. This leaves the chamber transparent so that vesicle formation and growth can be monitored throughout the entire process. Integrated features, including flexible protocol design and temperature control, allow generation of GUVs from lipids with high charge or high melting temperature.

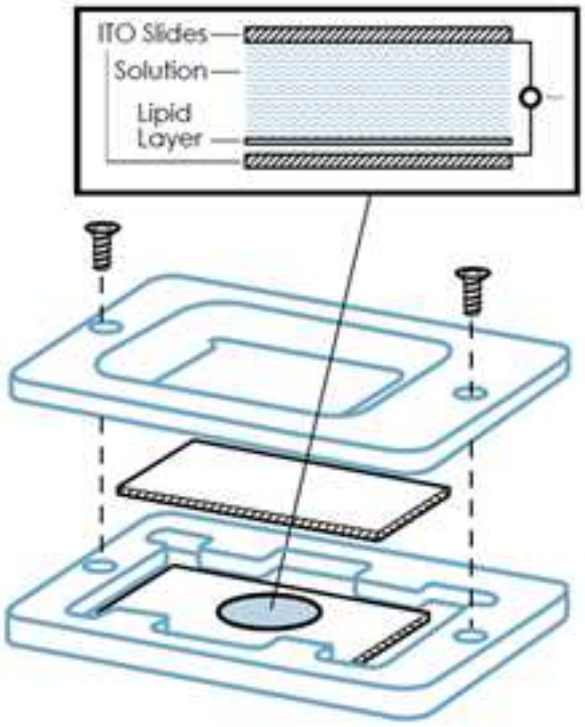

Figure 5.3: Diagram illustrating the setup for GUV fabrication [105]

Approximately 20 μL of the lipid stock solution was placed on the ITO glass surface of the Vesicle Prep Pro station and allowed to dry overnight in a vacuum chamber. Next, 18mm O-ring

was greased and placed around the dry lipid film. The lipid film was hydrated with 250 µL 0.5 M sorbitol placed inside the ring and the second ITO slide with the conducting side facing down was used to cover the O-ring. The vesicles were formed by electro-swelling under the influence of an AC electric field of 5 V_{p-p} amplitude and 10 Hz frequency for 2 hours at 36°C. GUVs formed (Figure 5.4) were suspended and collected in a vial.

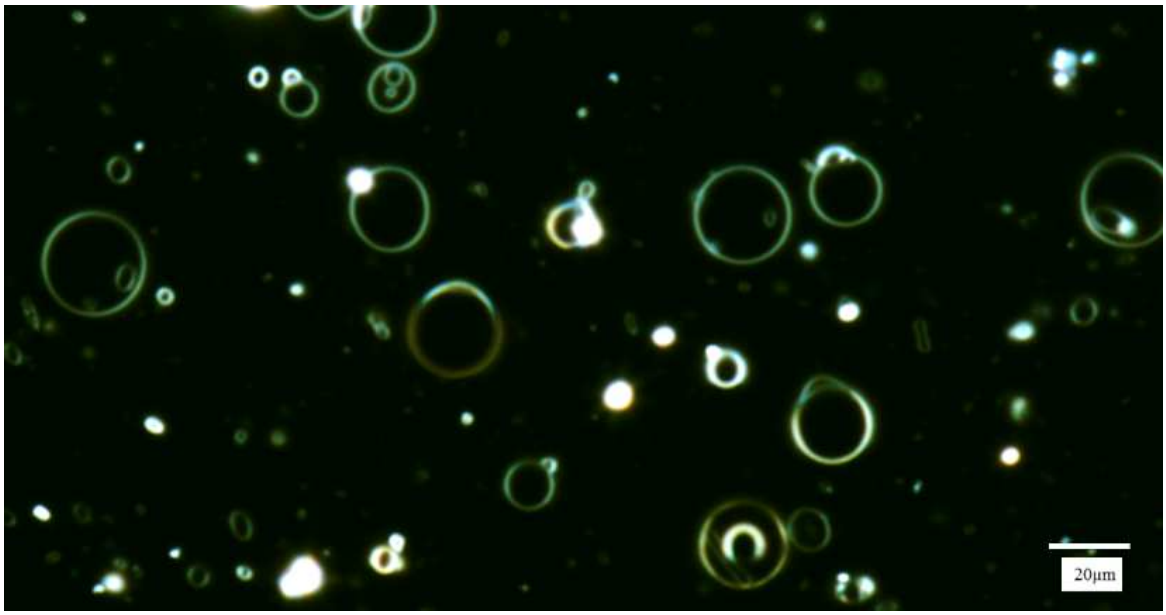

Figure 5.4: Image of GUVs formed after the electroformation process. The GUVs were around 20µm in diameter

5.2 Dark field microscopy

Dark field microscopy is an illumination technique to enhance the contrast in unstained samples causing them to appear brightly lit against a dark, almost black background. It works by illuminating the specimen with light that will not be collected by the objective lens and thus will not form part of the image. This produces the classic appearance of a dark almost black background with bright objects on it. Standard bright field microscopy relies upon gathering illuminating light by the condenser and focusing it at the plane of the specimen in the form of a

filled cone of light. Light rays passing through the specimen interfere with each other producing contrast and thereby build an image. To visualize the specimen, the specimen must have inherent high contrast caused by the refractive indices or be artificially stained. It is not possible to visualize transparent materials or thin unstained specimens with a bright field microscope. In a dark field microscope, the condenser is rather designed to form a hollow cone of light. The light at the apex of the cone is focused at the plane of the specimen. The image is made only by those rays scattered by the sample and captured in the objective lens. This method excludes the unscattered beam from the image. As a result the field around the specimen, where there is no specimen to scatter the beam, is generally dark. Sample contrast in dark field illumination arises from light scattered by the sample versus absorbance of light in the sample in bright field illumination [106-107].

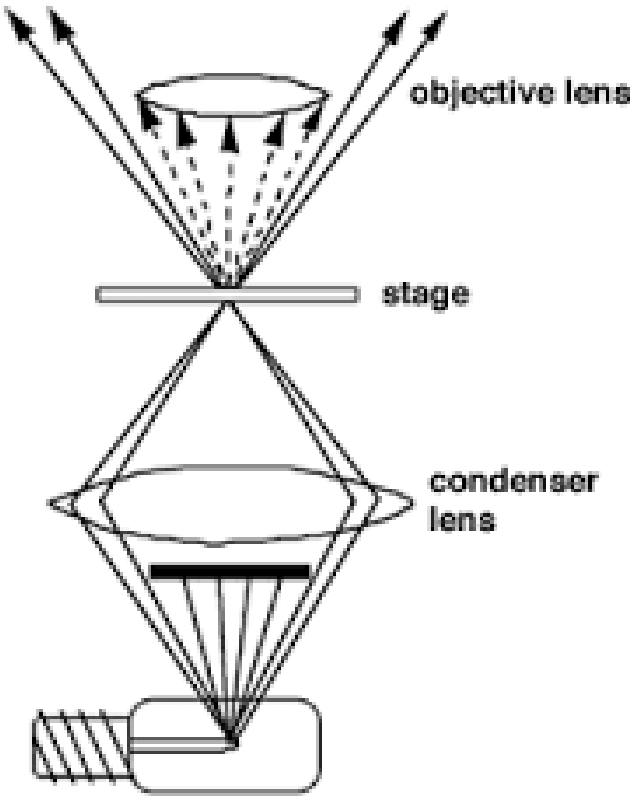

Figure 5.5: Ray diagram of a dark-field optical microscope [107]

5.3 Hyperspectral Imaging

Hyperspectral imaging (HSI) is a complex, highly multidisciplinary field that can be defined as the simultaneous acquisition of spatial images in many spectrally contiguous bands [108]. In this technique, a complete spectrum or some spectral information is collected at every location on the image plane and processed. The spectral images are often represented as an image cube, which is a form of data cube. Three dimensional hyperspectral cube is assembled by stacking two dimensional spatial-spectral scan lines as shown in Figure 5.6. Hyperspectral images appear very similar to a traditional optical image but with one important difference. Each pixel of a hyperspectral image provides the complete reflectance spectral response of that pixel's spatial area within the visible near infrared (VNIR) or short wave infrared (SWIR) spectral range (Figure 5.7). This enables nondestructive spectral measurements of nanoscale elements in the full spatial context of the sample image.

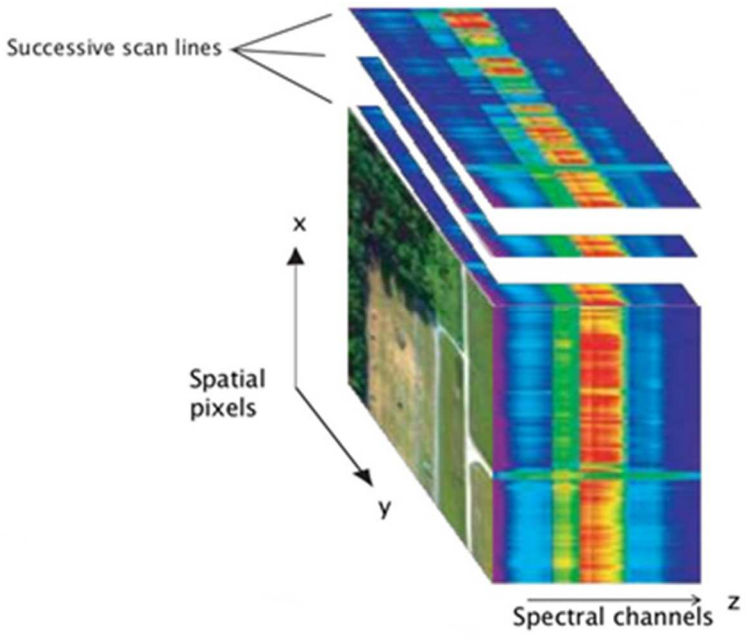

Figure 5.6: Representation of a hyperspectral image cube with two spatial dimensions and one spectral dimension [109]

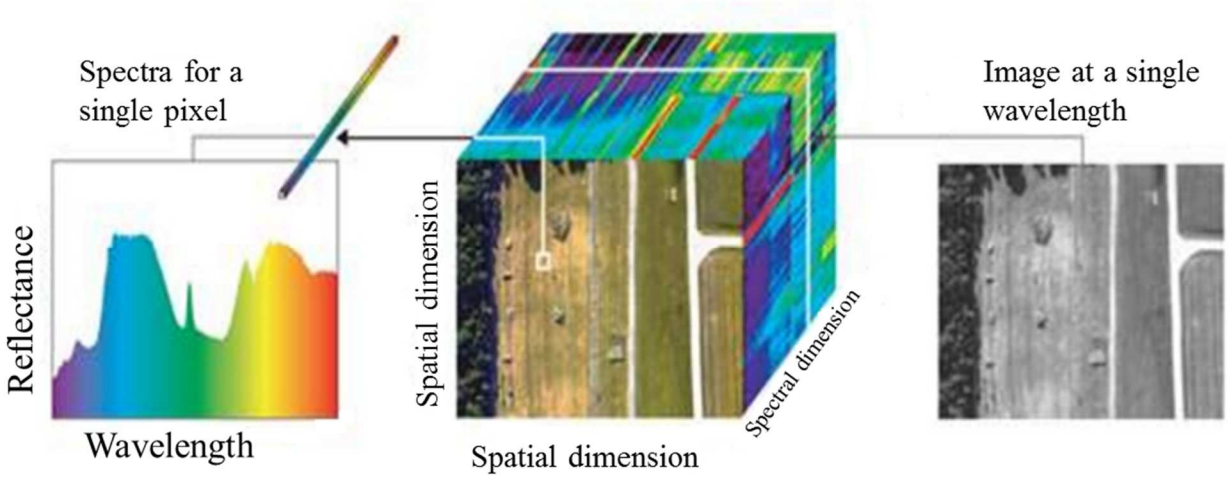

Figure 5.7: Distinction between hyperspectral image and traditional optical image [109]

The strong driving force behind the development of hyperspectral imaging is the integration of spectroscopy and digital imaging techniques. Hyperspectral images are produced by instruments called imaging spectrophotometers. Spectrophotometers provide much more detailed information about an image than a normal color camera, which only acquires three different spectral channels corresponding to the visual primary colors red, green and blue. Since hyperspectral imaging deals with the imaging of narrow spectral bands over a continuous spectral range and produces the spectra of all pixels in the scene, this imaging technique leads to a vastly improved ability to classify the objects in the image based on their spectral properties. An array of detectors collects this information as a set of images. These images are then combined and formed into a 3-D hyperspectral data cube for processing and analysis [109].

Hyperspectral imaging system combines a hyperspectral microscope and a program to analyze or process the images. Open source software such as HyperSpy and Gerbll or commercial ones as ENVI, MIA Toolbox, Scyllarus, and Opticks are a few that can be utilized to analyze the images

The following goals for analytical hyperspectral microscopy have to be met

i) Capture the spectrum of each point in a field of view

ii) Use classical spectroscopic methods to identify the spectra

iii) Sort and classify spectra and insert spectral classes into a reference library

iv) Use library spectra to locate objects and detect target conditions or processes

v) Generate a hyperspectral image or spectral topographical map

In terms of spectral acquisition

vi) All wavelength data points between a certain range must be acquired simultaneously

vii) Spectral acquisitions must be independent. The spectrum should not depend on past or future acquisitions

5.3.1 Principle of operation of hyperspectral imaging

The camera images the scene onto a slit, which only passes light from a narrow line in the scene. After collimation, a dispersive element such as a diffraction grating separates the different wavelengths, and the light is then focused onto a detector array. The net effect of the optics is that for each pixel interval along the line defined by the slit, a corresponding spectrum is projected on a column of detectors on the array. The data readout from the array thus contains a slice of a hyperspectral image, with spectral information in one direction and spatial information in the other. By scanning over the scene, the camera collects slices from adjacent lines, forming a hyperspectral image cube with two spatial dimensions and one spectral dimension. The acquisition techniques employed for hyperspectral imaging could be spatial scanning, spectral scanning or spatio-spectral scanning [110].

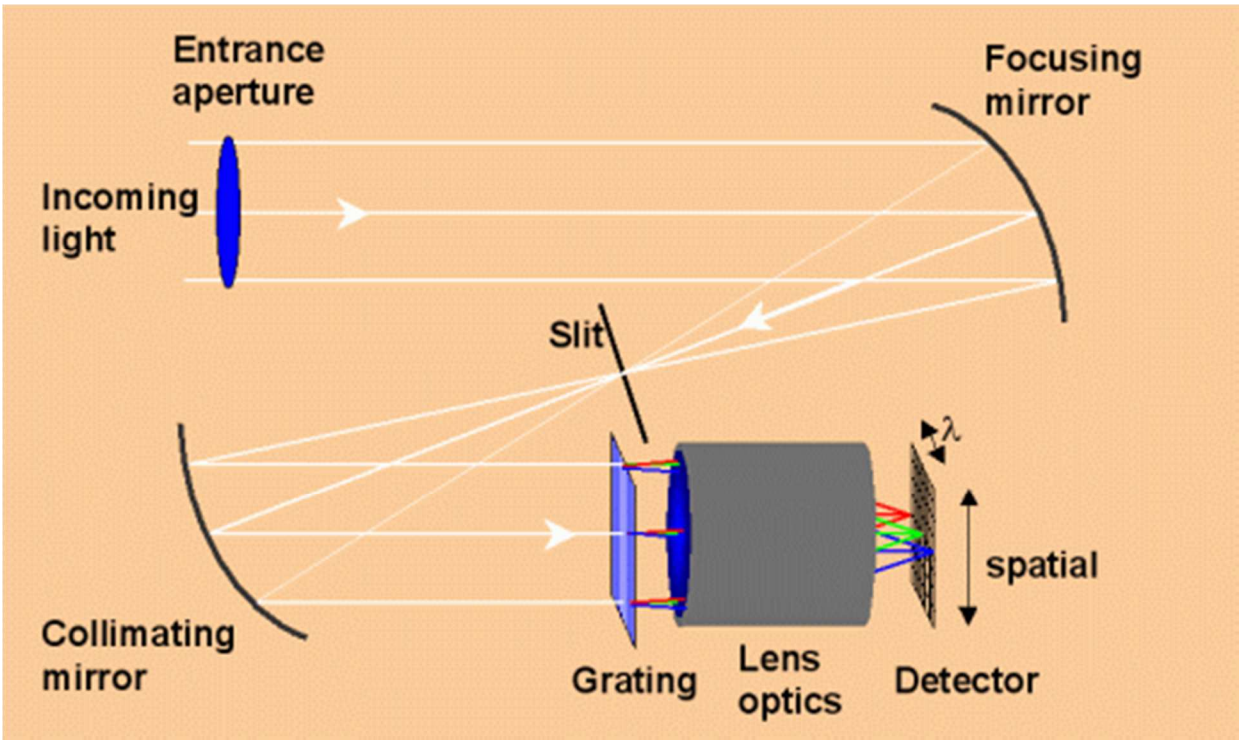

Figure 5.8: Schematic of a basic hyperspectral imaging system [110]

Enhanced hyperspectral darkfield microscope (CytoViva, Auburn, AL) was utilized for conducting this research. CytoViva is specifically designed to provide optical observation and spectral characterization of a wide range of nanomaterials such as noble metal nanoparticles, carbon nanotubes, quantum dots and polymeric particles [111]. Biologicals including bacteria, fungi and certain intracellular materials also can be optically imaged and spectrally characterized. Cytoviva combines a high signal-to-noise ratio (SNR) optical microscope with an integrated hyperspectral imaging system. The optical illumination system replaces the standard condenser on a research grade microscope. This system serves to perfect the alignment and focus of oblique angle illumination also known as dark field. The signal-to-noise enhancement improves detection as much as 80 times to standard dark field microscopy. Integrating hyperspectral imaging with the CytoViva equipped microscope enables spectral characterization

of nanoscale materials and biologicals. This characterization is accomplished by capturing visible near infrared (VNIR) reflectance spectrum from the sample at very high spectral resolution. The spectrophotometer has an integrated CCD, which collects the sample reflectance spectrum from every pixel of the scanned image to create a hyper spectral image. The automated microscope stage pushes the sample across the spectrophotometer field of view. The spectral file is the opened in the image analysis software ENVI. These spectral files appear as an RGB image which is virtually identical to the optical image observed in the microscope eyepiece. CytoViva hyperspectral microscope can be used to confirm the presence and location of the nanoscale element as they interact with other materials such as GUVs. This confirmation requires that the nanomaterial of interest is first scanned. The reference spectra of the material is collected and stored in the spectral library of ENVI. Then the nanomaterial can be spectrally characterized and mapped in the newly scanned sample.

5.3.2 ENVI

ENVI (ENvironment for Visualizing Images) is an image-processing program, which provides comprehensive data visualization and analysis for images of any size or type [112]. Its approach to image processing involves combining file based and band based techniques with interactive functions. When a data input file is opened, its bands are stored in a list, where they can be accessed by all system functions. ENVI displays these bands in 8- or 24- bit displays windows. ENVI's display window groups consist of a main Image window, a Zoom window, and a Scroll window, all of which are re-sizeable. ENVI provides its users with many unique interactive analysis capabilities, accessed from within these windows. The Available Bands List is the main control panel for accessing ENVI image files and the individual image bands within those files. The Available Bands List appears in its own dialog whenever an image file is opened,

contains a list of all of the available image bands for all of the open files and any memory items. ENVI's multiple dynamic overlay capabilities allow easy comparison of images in multiple displays. Real-time extraction and linked spatial/spectral profiling from multiband and hyperspectral data give users new ways of looking at high-dimensional data. ENVI's strong visual interface is complemented by its comprehensive library of processing algorithms. ENVI includes the basic image processing functions within an interactive point-and-click graphical user interface (GUI). Some of these functions include data transforms, filtering, spectral analysis tools, classification color mapping, region of interest definition and processing. ENVI provides a full suite of tools for processing hyperspectral data, including special mapping tools that use either image or library endmembers for linear spectral un-mixing and matched filtering. ENVI routines can be used to access spectral libraries and compare library spectra to image spectra. The software includes essential tools required for image processing across multiple disciplines, and has the flexibility to allow the user to implement user defined analysis strategies [112].

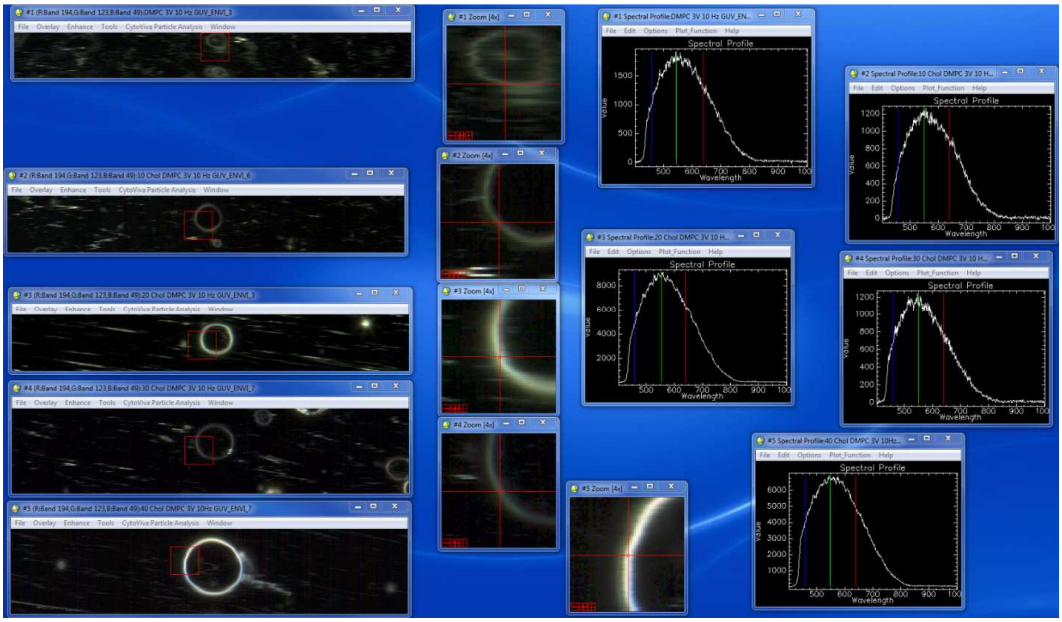

Figure 5.9: Illustration for determining spectral profile of GUVs

The spectral profile helps in characterizing the sample by displaying the intensity values in a selected wavelength range of a pixel of interest. The samples shown in Figure 5.9 are the GUVs made with DMPC and varying percent molar concentration of cholesterol. Hyperspectral images can be opened in ENVI and the spectral profile determined at a point of interest from the Zoom window as shown in the figure with a red cross-bar.

Enhanced dark field microscopy along with hyperspectral imaging enables

i) Observation of label free nanomaterials interacting with labeled biological and other matrices

ii) Spectrally identify and characterize nanomaterials

iii) Spectrally map nanomaterials in biological and other environments

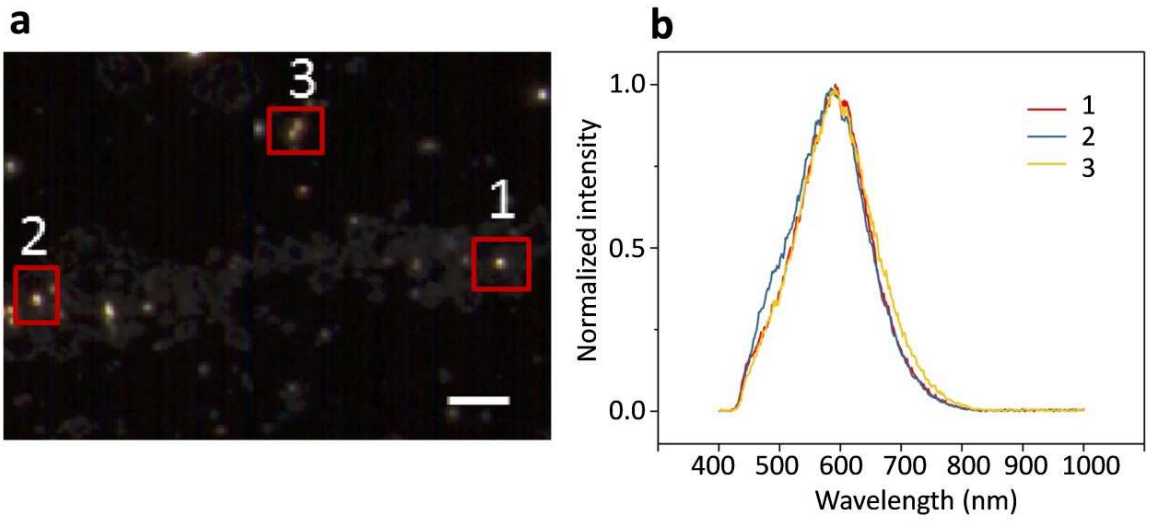

Figure 5.10: (a) Hyperspectral image (b) Spectral profile of AuNPs showing a peak around 600 nm

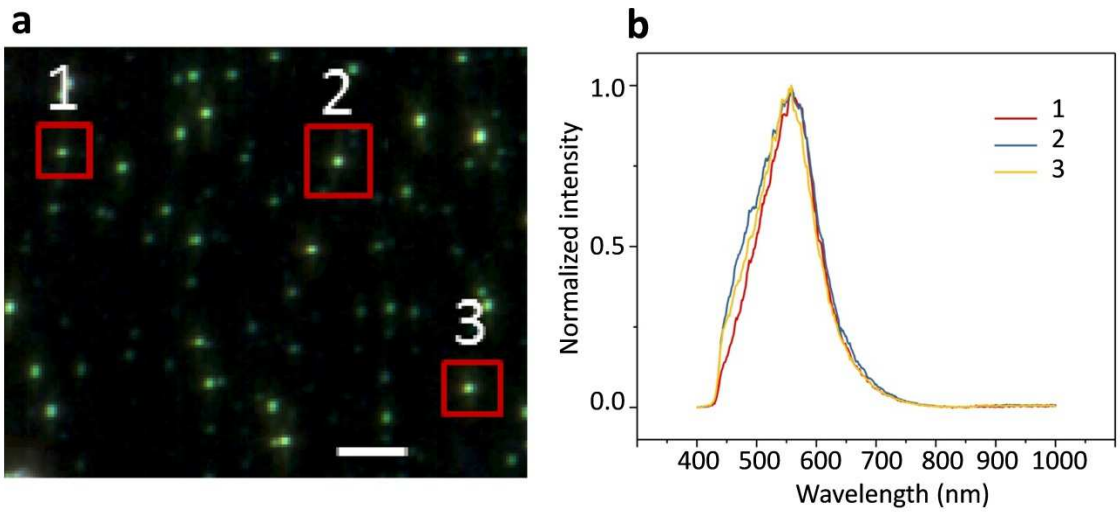

Figure 5.11: (a) Hyperspectral image (b) Spectral profile of AgNPs showing peak around 550-570 nm

Figure 5.10 and Figure 5.11 illustrate the dark field hyperspectral images and spectral profiles for AuNPs and AgNPs. The spectral profile for AuNPs shows a peak around 600 nm in the profile, which is distinct from AgNP spectral peak at 550-570 nm. The spectral profile is characteristic of the NPs and depends on the size and types of NPs.

5.4 Cholesterol

Cholesterol is a lipid with a steroid skeleton. The steroid skeleton is built from four linked hydrocarbon rings. The steroid skeleton is hydrophobic in nature. A hydrocarbon tail is linked to the steroid at one end, and a hydroxyl group is attached at the other end. The hydrocarbon tail adds to the hydrophobicity of the steroid skeleton. In membranes, the cholesterol molecule is oriented parallel to the fatty acid chains of the phospholipids. The hydroxyl group forms a hydrogen bond with the phosphate of the nearby phospholipid head group. The hydrophobic steroid skeleton of cholesterol shows Van der Waals attraction to the phospholipid acyl tails as shown in Figure 5.12. Interdigitating the cholesterol molecules in between the phospholipid

molecule increase the stability and rigidity of the membrane as well as decrease the membrane entropy. The tails of the phospholipid are held tighter in their place because the cholesterol is stabilizing them, which mean that the tails of the phospholipid are not free to flop around as much. So, the membrane becomes rigid with increasing concentration of cholesterol [113-115].

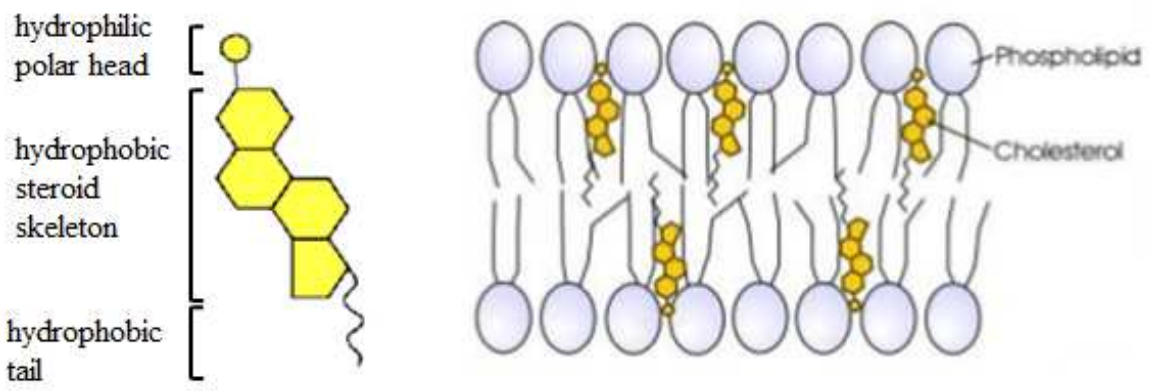

Figure 5.12: Cholesterol molecules interdigitated between phospholipid molecules [113]

5.5 Bovine serum albumin (BSA)

BSA is a stable non-reactive globular protein (~ 66,000 Da) that is generally used as a blocking agent to prevent nonspecific binding of antigens and antibodies. It is used in numerous biochemical reactions due to its stability and lack of interference within biological reactions. BSA is normally used to enhance the biocompatibility of NPs. When NPs are exposed to BSA, a protein corona is formed on the NP surface (NP_PC) that influences bio distribution, targeting and reduces the toxicity of bare NPs [116]. The formation of the protein corona is strongly dependent on the physiological conditions of the environment and the concentration and time

scale of exposure of NPs to proteins. Illustrated in Figure 5.13 is the ribbon model of BSA and protein corona of BSA on NP surface, which is formed when BSA interacts with NPs.

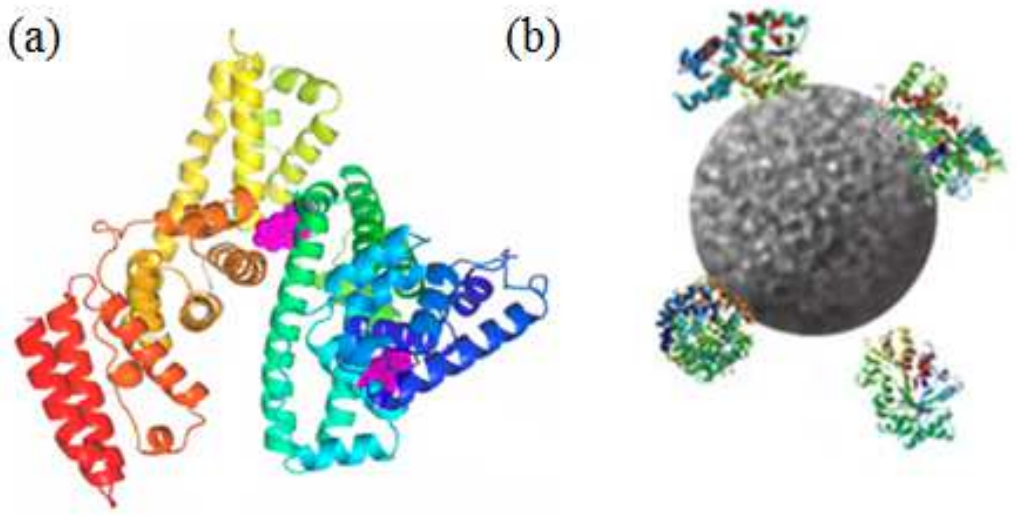

Figure 5.13: (a) Ribbon model of BSA. (b) Adsorption of BSA on NP surface resulting in the formation of NP_PC [117]

5.6 Experimentation

Following procedures were followed to make 10% BSA and AuNP-PC.

i) 10 % BSA: 20 mg of BSA powder was dusted over 180 µL of PBS in a vial, covered and stored in the refrigerator for 20 minutes.

ii) AuNP-PC: 20 mg of BSA powder was dusted over 180 µL of 10 nm AuNP in a vial, covered and stored in the refrigerator for 20 minutes.

Preparation of molar % cholesterol: DMPC at various concentrations

A stock solution of phospholipid DMPC (1,2-dimyristoyl-sn-glycero-3-phosphocholine, Sigma-Aldrich) dissolved in chloroform ($CHCl_3$) at 6 mg/mL was prepared. In the case of GUVs at various molar concentration of cholesterol (Chol) vs. DMPC, a stock solution of Chol/$CHCl_3$ at

10 mg/mL was mixed into the stock solution of DMPC/ $CHCl_3$ at 10, 20, 30, 40 molar percent (mol%) of Chol:DMPC. The amount of chol / $CHCl_3$ to achieve the required molar cholesterol concentration in DMPC is shown in Table 5.1

Table 5.1: Amount of cholesterol / $CHCl_3$ that needs to be added to 0.5 mL of DMPC/$CHCl_3$ to obtain a specific ratio of molar % cholesterol to DMPC

% molar chol : DMPC	**Amount of chol / $CHCl_3$ (µL)**
5	9
10	19
20	43
30	73
40	114

The Vesicle Prep Pro apparatus (Nanion Technologies, Germany) was used for the electroformation of GUVs. Approximately 20 µL of stock solution was dropped on the conducting side of an ITO-coated slide followed by the vacuum evaporation of solvent. A greased O-ring (diameter 28 mm) was then placed around the dried film and filled with 500 µL sorbitol (0.5 M). A second ITO slide with conductive side facing down was placed on top of the O-ring to sandwich the soaked film. The ITO slide set was thereafter fit in the electrode chamber of the Vesicle Prep Pro apparatus. Then an alternating voltage of 5 V (p-p) at 10 Hz was applied to the slide set at 36^{o}C. After two hours of running the electricity, GUVs are formed and collected in a vial for future use.

GUVs (20 µL) of varied composition of cholesterol were incubated with 5 µL of each of (a) 10nm AuNP, (b) 10nm AgNP, (c) AuNP_PC and (d) BSA for two hours prior to microscopy

experiments. To prepare for a sample slide, a drop of 0.5-1.5 µL incubated mixture was streaked on the slide and a cover slip was carefully flapped on the sample to minimize bubbles. The sample slide was then mounted on the dark-field microscope (CytoViva, Inc., Auburn, AL) for both optical and hyperspectral imaging. The hyperspectral images were collected and analyzed with ENVI.

5.7 Results and discussion

5.7.1 Hyperspectral images of GUVs containing varying molar cholesterol concentration

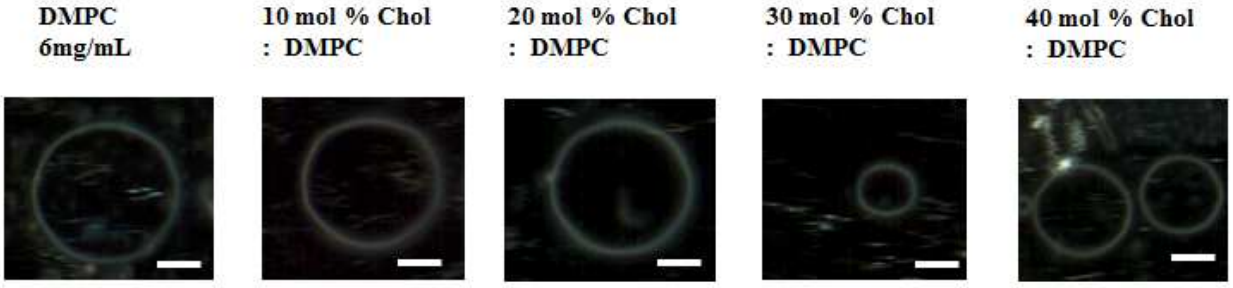

Figure 5.14: Hyperspectral images of GUVs containing varying molar cholesterol concentration made with electroformation voltage amplitude 5V and frequency 10 Hz. Scale bar 5µm

GUVs fabricated with parameters; Amplitude: 5V, Frequency: 10 Hz, Temperature: 36 ° C, Time: 128 minutes, had a higher yield than GUVs made with parameters; Amplitude: 3V, Frequency: 10 Hz, Temperature: 36 ° C, Time: 128 minutes. The GUVs were also consistent in shape and size. Figure 5.14 represents the hyperspectral images of GUVs made with varying molar cholesterol concentration as indicated. Qualitative analysis showed that DMPC GUVs without cholesterol exhibit significant thermal shape fluctuations. The firmness and integrity of the GUVs increases with increased molar concentration of cholesterol indicating increase in the bending rigidity. GUVs containing 20 mol% or more of molar concentration of cholesterol tend to agglomerate. GUVs comprising varying cholesterol concentrations were treated with

AuNPs/AgNPs and the interaction was analyzed with dark field hyperspectral imaging to understand the interaction of AuNPs and AgNPs with GUVs, which is discussed in section 5.7.2.

5.7.2 Hyperspectral images of AuNPs and AgNPs interacting with GUVs

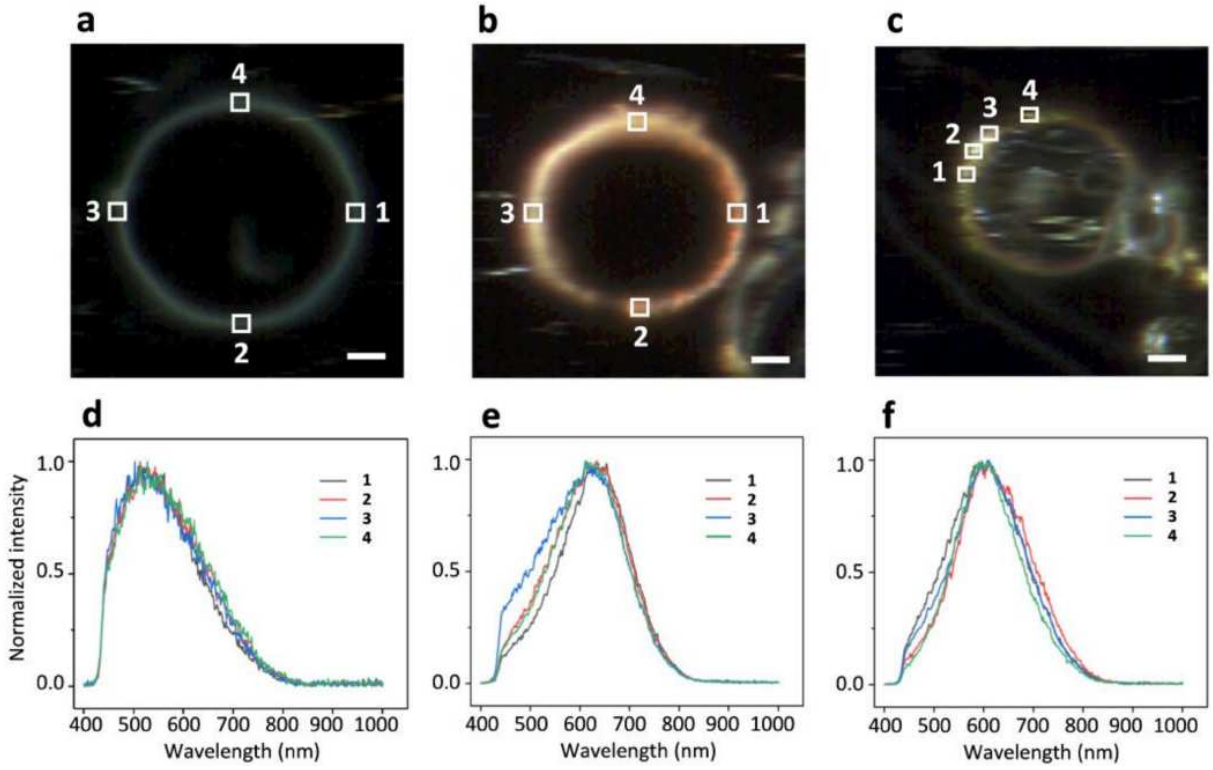

Figure 5.15: Hyperspectral images and reflectance spectral profiles of (a) GUVs at 20 mol% Chol: DMPC, (b) AuNPs and GUVs at 20 mol% Chol:DMPC, and (c) AgNPs and GUVs made of DMPC only. Scale bar 5µm

Figure 5.15 displays the representative hyperspectral images of GUVs alone and GUVs interacting with AuNPs/AgNPs. The corresponding reflectance spectral profiles from selected pixels on the lipid bilayers are shown below. The spectral profile of the lipid bilayer of GUVs peaks around 550 nm, much broader in shape as compared to that of AuNPs or AgNPs as shown in Figure 5.10 and Figure 5.11 respectively. Upon NP adsorption on GUVs, the spectral profiles collected at the NP adsorbed lipid bilayers are much broadened as compared to those of AuNPs or AgNPs alone (Figures 5.10 and 5.11) or GUV alone (Figure 5.15a).

Red shifts of spectral profiles occurred for AuNPs and AgNPs when adsorbed on lipid membranes. In the case of AuNPs, most peaks shifted approximately from 600 nm to 630 nm when adsorbed on GUVs (Figure 5.10 vs. Figure 5.15b). In the case of AgNPs, some peaks shifted approximately from 560 nm to 610 nm with most peaks sticking around 560 nm (Figure 5.11 vs. Figure 5.15c), close to both the peaks of GUV alone (Figure 5.15a) or AgNPs alone (Figure 5.11). The difference in the peak shifts between AuNP- vs. AgNP-adsorbed GUVs is also reflected in the hyperspectral images. When AuNPs interact with GUVs, they tend to form a continuous coverage on the vesicle, with rarely distinguishable isolated NPs. whereas when AgNPs interact with GUVs, they tend to anchor on the lipid vesicle surface with much distinguishable isolated NPs. This morphological difference in NP-membrane interactions explains why the AuNP-adsorbed vesicle surface showed a consistent peak shifts while the peak shifts for AgNP-adsorbed vesicles were much dispersed.

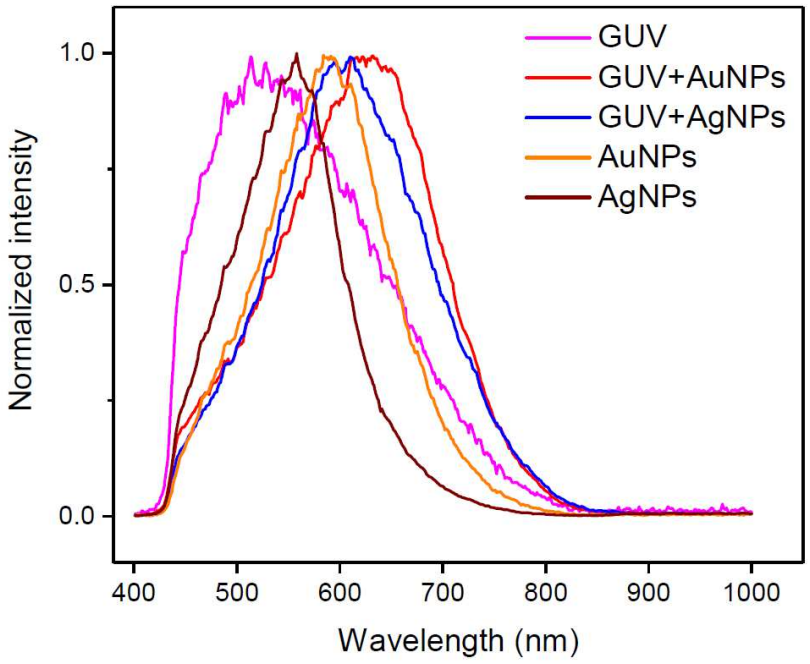

Figure 5.16: Red shift of spectral profiles for GUVs treated with AgNPs and AuNPs

Figure 5.16 consists of the normalized spectral profiles averaged from plots of AuNPs, AgNPs, GUVs, GUV+AuNPs, and GUV+AgNPs, respectively. The GUVs shown in this graph were made of 20 mol% CHOL: DMPC. The red shifts occur for both AuNPs and AgNPs upon interactions with GUVs. The spectral broadening also occurs for both AuNPs and AgNPs upon interactions with GUVs. The spectral profile of GUV alone is more asymmetric than the other four, leaning toward blue and tapering off toward red. The spectral profiles of AgNPs and GUVs are both asymmetric yet result in a symmetric profile upon interactions of AgNPs and GUVs. The spectral profile of AuNPs is relatively symmetric yet results in a slightly asymmetric profile upon interacting with GUVs. From the difference of spectral shifts between AuNP-GUV and AgNP-GUV (Figure 5.16), we hypothesize that there exists a difference in the mechanism of interactions between AuNPs/AgNPs and GUVs. AuNPs are more likely integrated in the lipid bilayer. If AuNPs were simply adsorbed on the lipid bilayer (or co-localization physically), the resulting spectral profile should have been the overlap of those of AuNPs and GUVs alone. Since the observed peaks of GUVs or AuNPs alone were 550 nm and 600 nm, respectively, the expected spectral peak of the overlap should be between 550 and 600 nm. However, the observed spectral peak of the complex had an overall red shift to 630 nm, the wavelength is even longer than from AuNPs alone. When it comes to AgNPs, they mostly are adsorbed on the lipid bilayer as individual NPs. The spectral profiles appear broadened because of the AgNP-GUV interaction. However, the spectral peaks of the complex in some cases had blue shifts to around 520 nm while in other cases had red shifts to 620 nm with respect to 560 nm for AgNPs alone. The interactions between AgNPs and GUVs are more varied than between AuNPs and GUVs. Integration and adsorption are equally likely for AgNP-GUV interaction, while integration is more prevalent for AuNP-GUV interaction.

The attractive forces between AuNPs and AgNPs and the bilayer will initially be electrostatic given the cationic amine and anionic phosphate groups in the outer vesicle region and the negatively charged citrate layer around both NPs. However, for AgNPs, the citrate anions in the particle solvation sphere are loosely bound relative to AuNPs. Au has a higher effective nuclear charge relative to Ag, so the ability of cations to disrupt the outer layer and cause aggregation might occur largely for AuNPs than for AgNPs. The + and - charges on the surface of DMPC would cause greater surface aggregation of AuNP than for AgNP suggesting that AuNP might interact more with other AuNP particles (in the cationic amine region of DMPC) while AgNP is free to interact more with the membrane as a result of the lesser effect of surface citrate charge neutralization and resulting particle aggregation.

Figure 5.17 displays an array of hyperspectral images showing interactions between AuNP/AgNP and GUVs. GUVs of varied composition including DMPC alone and 10, 20, 30, and 40 mol% Chol: DMPC were tested for the interactions and imaged.

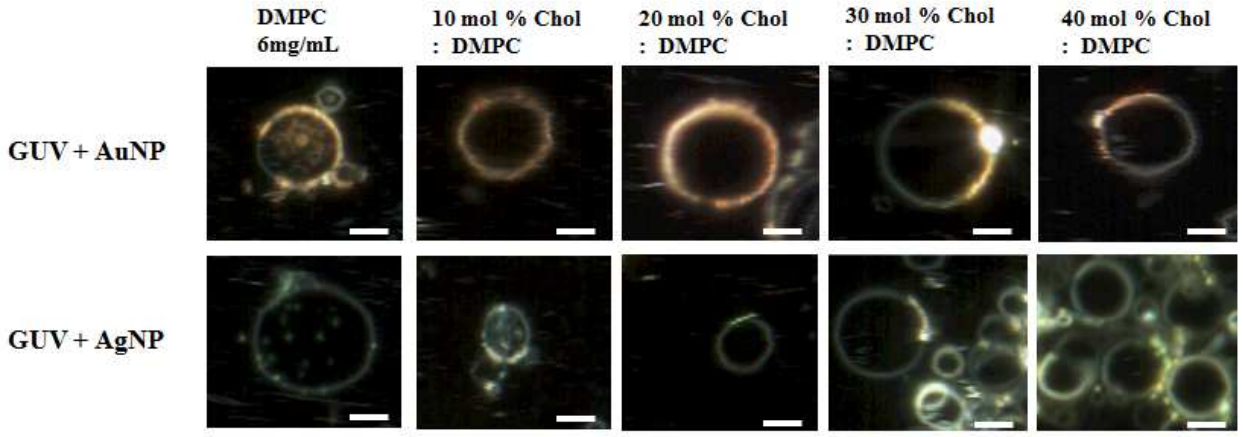

Figure 5.17: Hyperspectral images of GUVs with different cholesterol concentration interacting with AuNPs and AgNPs. Scale bar 5μm

The hyperspectral images (Figure 5.17) show that nanoparticles are adsorbed on the periphery of the GUVs. The extent of adsorption depends on the type of nanoparticles. AuNPs form a continuous coverage on the vesicle compared with AgNPs. Also observed is the aggregation of individual GUVs at increased cholesterol concentration. AuNPs/AgNPs play a negligible role in agglomerating GUVs. AgNPs have been observed to cause pearling on vesicles though the effect is more pronounced with AuNPs along with clustering. The difference between AuNP-GUV and AgNP-GUV interactions as previously analyzed in section 5.7.2 was consistently observed in Figure 5.17. That is, when AuNPs interact with AuNPs, they tend to form a continuous coverage on the vesicle, with rarely distinguishable isolated NPs. While AgNPs tend to anchor on the lipid vesicle surface with much distinguishable isolated NPs.

It is also noticed that GUVs made up of DMPC alone are most permeable, allowing the translocation of significant amount of AuNPs or AgNPs. However, AuNPs found inside the vesicles are fuzzy, bulky and agglomerated whereas AgNPs found inside the vesicles are well defined, isolated and dispersed. By comparing the NPs inside the vesicles in the image array of Figure 5.17, it can be concluded that the permeability of GUVs decreases with increasing molar concentration of cholesterol. This could happen because the addition of cholesterol in GUVs stiffens the bilayer and shifts the lipid toward gel phase. AgNPs are more capable of penetrating across the lipid membrane than AuNPs. Because AgNPs were still spotted inside GUVs when the concentration of cholesterol increased to 10 mol%, but this leakage was not observed for AuNPs for any cholesterol-doped GUVs.

The peak wavelength and FWHM (full width at half maximum) (Figure 5.18) were determined from spectral profiles collected from a wide range of samples including AuNPs alone, AgNPs alone, GUVs alone, GUV+AuNPs, and GUV+AgNPs. GUVs tested were of varied

composition ranging from DMPC alone to 10, 20, 30, 40 mol% of CHOL: DMPC. For each sample analysis, approximately 15 different regions were selected from respective hyperspectral images. In each region of interest, approximately 10 points were selected to produce the average spectral profile. The peak wavelength and FWHM were then determined from the exported spectral data by finding the wavelength corresponding to the maximum intensity and spectral width at half of the maximum intensity. The determination of peak wavelength and FWHM was performed for all 15 regions of interest for each sample. Then the data of peak wavelength and FWHM were averaged to produce the mean and the standard deviation for each sample.

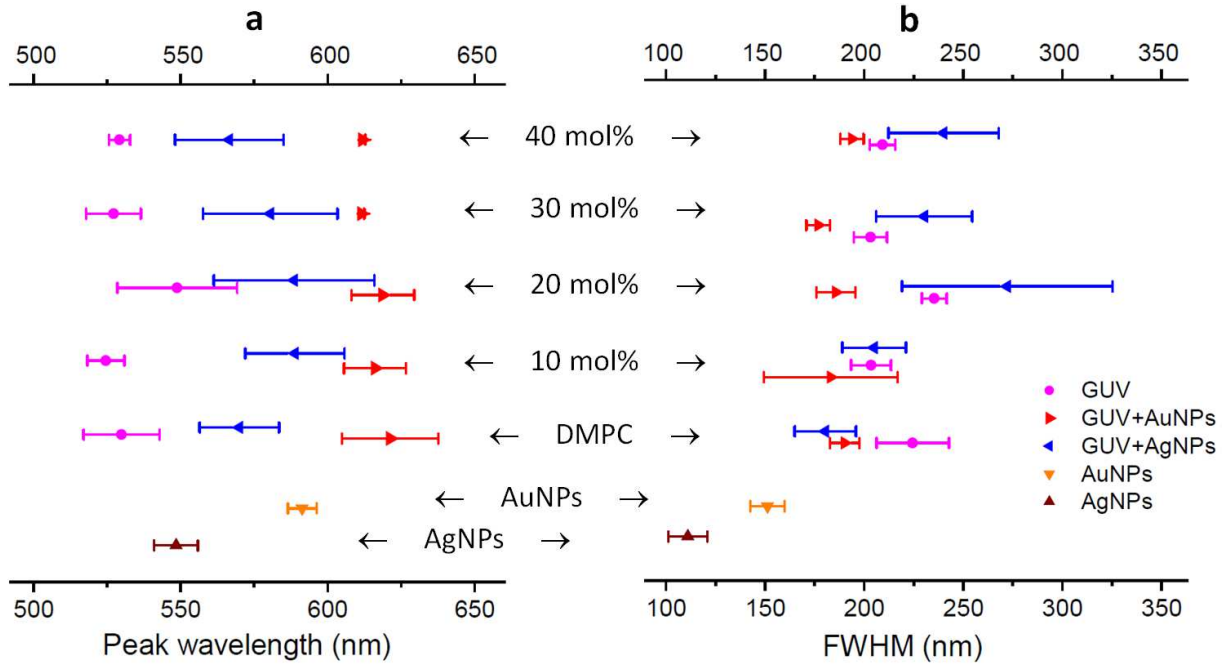

Figure 5.18: (a) The peak wavelengths and (b) the FWHM of the spectral profiles from AuNPs alone, AgNPs alone, GUVs alone, GUV+AuNPs, and GUV+AgNPs. The GUV composition was varied from DMPC only to 10, 20, 30 and 40 mol% CHOL: DMPC. The error bars are based on the standard deviations calculated from 15 regions of interest for each sample.

Figure 5.18 displays the peak wavelengths and FWHM (full width at half maximum) analyzed from spectral profiles collected from samples including AuNPs alone, AgNPs alone, GUVs alone, GUV+AuNPs, and GUV+AgNPs, noting that GUVs used were of varied composition including DMPC alone and 10, 20, 30, 40 mol% of CHOL:DMPC. Each data point in the graph is the mean and the standard deviation calculated from the spectral profiles of 15 regions of interest selected from that sample. It is found in Figure 5.18a that the mean peak wavelength of AuNPs is 591 nm and the mean peak wavelength of AgNPs is 548 nm. The peak wavelengths for GUVs of varied composition are around 528 nm except for GUVs of 20 mol% CHOL:DMPC which peaks at 549 nm, coinciding with the peak wavelength of AgNPs. The red shifts of peak wavelength are observed for all cases of GUV+AuNPs and GUV+AgNPs from those of NPs alone. The peak wavelength of GUV+AuNPs shifts to ~616 nm from 591 nm for AuNPs alone, an increase of 25 nm. The peak wavelength of GUV+AgNPs shifts to ~579 nm from 548 nm for AgNPs alone, an increase of 31 nm. In general, the peak wavelengths of AuNPs and AgNPs are both of small errors, as expected from the uniformity of particles in size and shape. However, even smaller errors are found for GUVs alone at 40 mol% CHOL:DMPC and GUV+AuNPs at 30 and 40 mol% CHOL:DMPC, suggesting a very stable peak wavelength for high concentration of CHOL especially when interacting with AuNPs. In contrast, much greater errors are noticed for peak wavelengths of GUV+AgNPs for all different compositions of GUVs, indicating that the peak wavelengths shift widely when GUVs interact with AgNPs. This stark contrast in peak wavelength shifts between AuNPs and AgNPs upon interacting with GUVs may suggest a fundamental difference of the underlying mechanism governing the NP-membrane interaction. Also worth noting is that GUV composition of 20 mol% CHOL:DMPC, which not

only sees the greatest peak wavelength among all GUV compositions but also the greatest errors for GUVs only and GUV+AgNPs.

It is found in Figure 5.18b that the mean FWHM of AuNPs is 151 nm and the mean FWHM of AgNPs is 111 nm. The FWHM for GUVs of varied composition are around 210 nm except for GUVs of 20 mol% CHOL:DMPC whose FWHM is 235 nm. The broadening of FWHM are observed for all cases of GUV+AuNPs and GUV+AgNPs from those of NPs alone. The FWHM of GUV+AuNPs increases to ~186 nm from 151 nm for AuNPs alone, a broadening of 35 nm. The FWHM of GUV+AgNPs increases to ~226 nm from 111 nm for AgNPs alone, an astounding broadening of 115 nm, more than doubled. This stark contrast in FWHM broadening between AuNPs and AgNPs upon interacting with GUVs further suggests a difference underlying NP-membrane interactions. Again, at GUV composition of 20 mol% CHOL:DMPC, the greatest error is observed for GUV+AgNPs as is the case for peak wavelength of GUV+AgNPs at this GUV composition. GUV+AgNPs at GUV composition of 20 mol% CHOL:DMPC is the most interesting case among all plotted.

Another noticeable general trend observed in Figure 5.18b is that the mean FWHM of GUVs of all different compositions is ~215 nm, 29 nm broader than that of GUV+AuNPs with FWHM at ~186 nm whereas 11 nm narrower than that of GUV+AgNPs with FWHM at ~226 nm. It is somewhat counterintuitive that AuNPs decrease the spectral width of GUVs upon NP-membrane interactions whereas AgNPs increase the spectral width of GUVs upon NP-membrane interactions.

The interaction of protein BSA and protein corona of BSA coated on 10nm AuNP, with GUVs characterized with different amount of cholesterol concentration was quantified using dark field microscopy whose images are shown in Figure 5.19

5.7.3 Hyperspectral images of GUVs with different cholesterol concentration interacting with AuNP_PC and BSA

Figure 5.19 displays an array of hyperspectral images showing interactions between GUVs and AuNP_PC/ BSA. GUVs of varied composition including DMPC alone and 10, 20, 30, and 40 mol% Chol: DMPC were tested for the interactions and imaged.

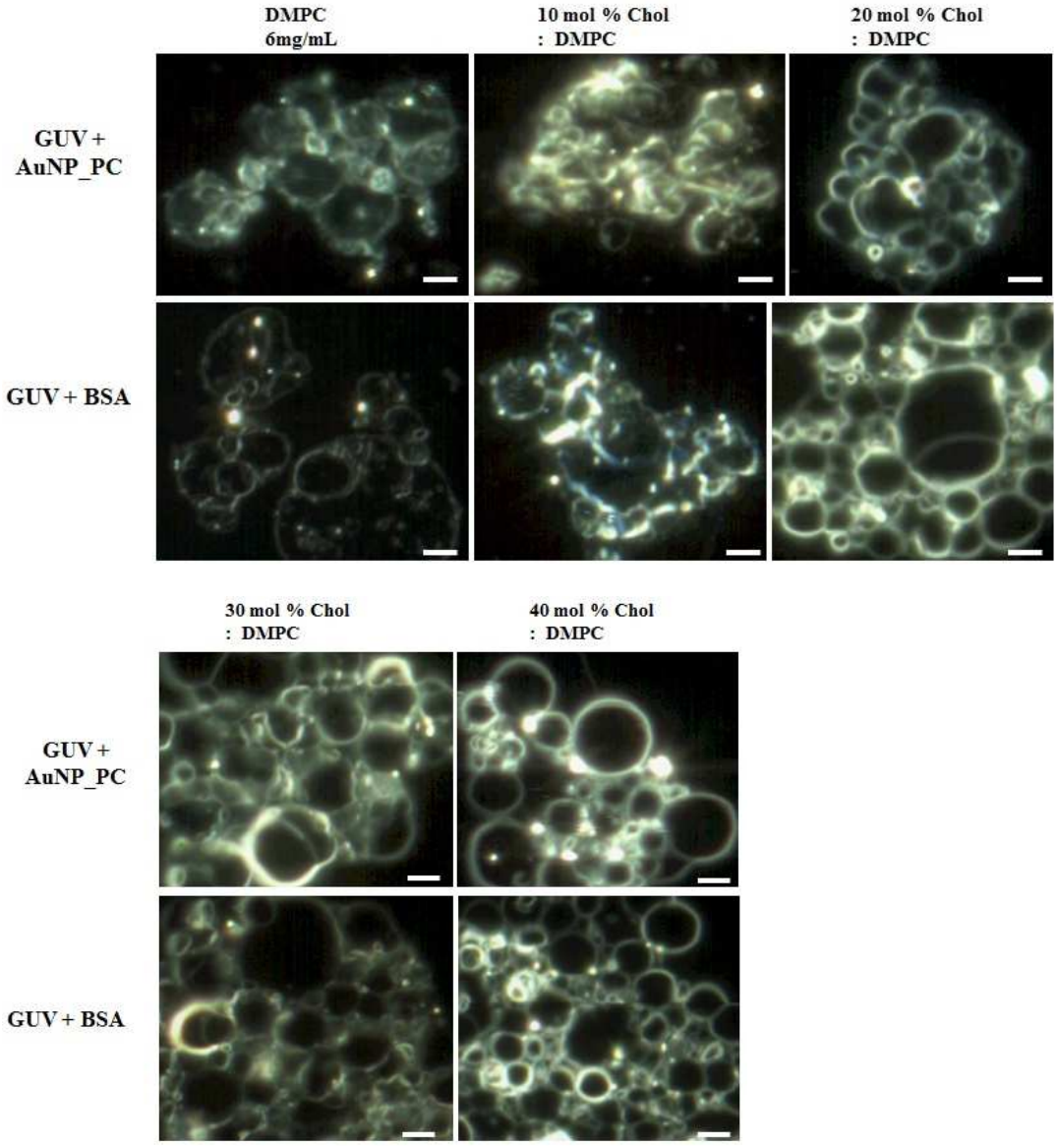

Figure 5.19: Hyperspectral images of GUV with different cholesterol concentration interacting with AuNP_PC and BSA. Scale bar 5µm

It is observed in Figure 5.19 that AuNPs coated with PC (protein corona) are hardly distinguishable as isolated NPs. It was observed that BSA and AuNP_PC change the morphology of the GUVs. AuNP_PC particles adhere generously to the GUVs compared to BSA particles at lower cholesterol concentration. AuNP_PC and BSA tend to aggregate GUVs even for pure DMPC composition. For Chol: DMPC GUVs, AuNP_PC and BSA lead to clustering effect and loss of GUV circularity. Phase changes start to emerge at 20 molar % cholesterol concentration GUVs for BSA as well as AuNP_PC treated GUVs. GUVs with 40 molar % cholesterol concentrations tend to maintain circular shapes better although they are assembled in a cluster for BSA as well as AuNP_PC treatments.

CHAPTER VI

CONCLUSION AND FUTURE WORK

6.1 Conclusion

In summary, citrate stabilized AuNPs from 5 to 30 nm generally increase the fluidity of as-prepared DMPC lipid vesicles as found in fluorescence shifts of laurdan and AFM nanomechanical characterization. The increased fluidity leads to an increased surface area, which results in lipid vesicle shape changes from circular to less circular, as confirmed in fluorescence images. The localized stress in lipids induced by electrostatically adsorbed AuNPs was hypothesized to cause the dominant long-range effect of fluidization of unbound lipid membranes. A secondary effect of the AuNP induced lateral pressure is the membrane rupture or pore formation, as observed in multi-mode AFM under fluid. What we found in this study supports the supposition in an earlier article that "nanoparticle- induced reconstruction of the phase state offers a new mechanism to modulate stiffness". The rigid patches on cell membranes, or lipid rafts, are traditionally held as liquid-ordered domains stiffened by enrichment of cholesterol and sphingolipids [118]. In this study, the adsorption of AuNPs was found to offer an alternative approach of modulating membrane packing: they stiffen the lipids bound to them whereas fluidize lipids far from the binding sites.

Darkfield microscopic study of the interaction between Au/AgNPs and GUVs reveals that NPs bind to the GUV surface. AuNPs are more likely integrated into the bilayer, whereas AgNPs tend to interact with GUVs as isolated particles with comparable possibilities of adsorption and integration. Considering the factors of biocompatibility and adsorption, AuNPs and AgNPs have thus been a favorable choice as targeted delivery vehicles in

nanomedicine. Incorporation of increasing levels of cholesterol increases the degree of order of orientation and reduces the rate of motion of the phospholipid hydrocarbon chains leading to a laterally more condensed membrane, with increased packing density of the phospholipids. This increases the mechanical strength and decreases the permeability of the membrane. The curvature related effects on vesicles due to the proteins in BSA and the protein corona were observed. The interaction of lipids with BSA and AuNP_PC brought about an aggregation of the vesicles with the protein corona and BSA modulating the lipid bilayer, but a specific correlation between the protein corona on AuNPs and the cholesterol concentration in the vesicles could not be established. Understanding the factors that modulate lipid packing is important for the discovery of alternative therapeutic methods for diseases that are linked to membrane integrity such as high blood pressure and cancer metastasis.

6.2 Future work

6.2.1 Experimental

The %GP changes for AuNP treated extruded DMPC vesicles showed positive changes compared with negative changes for non- extruded DMPC vesicles. Extruded DMPC vesicles are characterized with diameters of around 1μm, indicating that %GP changes depend on the size and curvature of vesicles. An experiment to study the curvature related effects of AuNP treated extruded vesicles thus could be carried out.

Phase separation in lipid vesicles is an important phenomenon, which arises in a binary or tertiary mixture of lipids. In current research, the lipid formulation was limited to DMPC and cholesterol. Future experiments could include studying the %GP changes of NP treated lipid vesicles that consist of a mixture of lipids such as DMPC, DMPG (1,2-dimyristoyl-sn-

glycero-3-phosphoglycerol), POPC (1-palmitoyl-2-oleoyl-sn-glycero-3-phosphocholine) and POPG (1-palmitoyl-2-oleoyl-sn-glycero-3-phosphoglycerol). Such mixtures would possibly show enhanced phase separation in the vesicles, which may influence the %GP changes.

Membrane leakage is one of the key events associated with cytotoxicity and more generally with the interaction of engineered nanoparticles with living systems in the environment. Determination of the physical changes in lipid vesicles, such as fluidity changes, circularity changes, lipid packing modulation and pore formation, induced by AuNPs was accomplished in this research. In addition to a large number of factors, the efficiency of NP interaction depends on the diffusion properties of the cell membrane. The molecular trafficking through the GUV-NP structures can be investigated by fluorescence correlation spectroscopy (FCS) [119]. FCS allows determination of both, the diffusion coefficient (the hydrodynamic size) and the concentration of fluorescent probes in a selected region of the sample. Tracking the diffusion of a fluorescent lipid probe on the GUV surface can provide information on the variation of lipid translational mobility within the GUV bilayer upon interaction with NPs, which is relevant for nanomedicine and nanotoxicology.

6.2.2 Simulation

Molecular dynamics simulations have evolved into a mature technique that can be used effectively to understand macromolecular structure-to-function relationships. The lipid vesicle curvature aided by protein structures was observed in our research for DMPC GUVs using darkfield microscopy with hyperspectral imaging. With present simulation times close to biologically relevant ones, molecular dynamics simulation of GUV-NP_PC system can provide atomistic details of the conformational changes in protein, which induce the curvature in lipid vesicles. Molecular dynamics simulation can also be used to study lipid-

lipid, lipid-protein, protein-protein interactions which are difficult to probe at the single molecule level. Next generation spectroscopic techniques and computational modeling are nearing overlap in resolution, spatially and temporally, making future avenues of research and collaboration possible.

REFERENCES

[1] M. P. Monopoli, C. Aberg, A. Salvati & K. A. Dawson, Biomolecular coronas provide the biological identity of nanosized materials, Nature Nanotechnology, (2012), 779-786

[2] Z. W. Lai, Y. Yan, F. Caruso & E. C. Nice, Emerging Techniques in Proteomics for Probing Nano-Bio Interactions, ACS Nano, (2012), 10438-10448

[3] N. Lewinski, V. Colvin & R. Drezek, Cytotoxicity of Nanoparticles, Small, (2008), 26-49.

[4] S. J. Klaine, P. J. J. Alvarez, G. E. Batley, T. F. Fernandes, R. D. Handy, D. Y. Lyon, S. Mahendra, M. J. McLaughlin & J. R. Lead, Nanomaterials in the environment: Behavior, fate, bioavailability, and effects, Environmental Toxicology and Chemistry, (2008), 1825-1851

[5] H.-m. Ding & Y.-q. Ma, Theoretical and Computational Investigations of Nanoparticle-Biomembrane Interactions in Cellular Delivery, Small, (2015), 1055-1071.

[6] E. Nel, L. Mädler, D. Velegol, T. Xia, E. M. V. Hoek, P. Somasundaran, F. Klaessig, V. Castranova & M. Thompson, Understanding biophysicochemical interactions at the nano-bio interface, Nature Materials, (2009), 543-557

[7] P. J. J. Alvarez, V. Colvin, J. Lead & V. Stone, Research Priorities to Advance Eco-Responsible Nanotechnology, ACS Nano, (2009), 1616-1619

[8] S. Li & N. Malmstadt, Deformation and poration of lipid bilayer membranes by cationic nanoparticles, Soft Matter (2013), 4969-4976

[9] T. H. F. Thake, J. R. Webb, A. Nash, J. Z. Rappoport & R. Notman, Permeation of polystyrene nanoparticles across model lipid bilayer membranes, Soft Matter, (2013), 10265-10274

[10] S. Zhang, A. Nelson & P. A. Beales, Freezing or Wrapping: The Role of Particle Size in the Mechanism of Nanoparticle - Biomembrane Interaction, Langmuir, (2012), 12831-12837

[11] K. W. Nägeli & K. E. Cramer, Pflanzenphysiologische Untersuchungen, , (1855-58), vol (4)-1

[12] H. Davson & J. F. Danielli, The Permeability of Natural Membranes. Second Edition, Soil Science, (1953)

[13] J. Robertson, The ultrastructure of cell membranes and their derivatives, (1959),

[14] M. Luckey, Membrane Structural Biology: With Biochemical and Biophysical Foundations, (2008),

[15] G. Lee, Biological membranes: the importance of molecular detail, Trends in Biochemical Sciences, (2011), 493-500

[16] S. J. Singer, Some Early History of Membrane Molecular Biology, Annual Review of Physiology, (2004), 1-27

[17] S. J. Singer & G. L. Nicolson, The Fluid Mosaic Model of the Structure of Cell Membranes, Science, (1972), 720-731

[18] R. Lipowsky & E. Sackmann, Structure and Dynamics of Membranes From Cells to Vesicles, Handbook of Biological Physics, (1995), 1-1020

[19] E. Sackmann, Biological Membranes, Academic Press, London, (1984),

[20] B. Alberts, A. Johnson, J. Lewis, M. Raff, K. Roberts & P. Walter, Molecular biology of the cell, Garland Science, (2002),

[21] H. Wiegandt, Glycolipids, Volume 10, New Comprehensive Biochemistry, (1985), 313

[22] Shevchenko & K. Simons, Lipidomics: coming to grips with lipid diversity, Nat Rev Mol Cell Biology, (2010), 593-8

[23] J. N. Kanfer & S.-I. Hakomori, Handbook of Lipid Research Vol. 3, Sphingolipid Biochemistry, (1983), 1-165

[24] H. Ohvo-Rekila, B. Ramstedt, P. Leppimaki & J. Slotte, Cholesterol interactions with phospholipids in membranes., Prog Lipid Res, (2002), 66-97

[25] J. Lundbaek, A. Maer & O. Andersen, Lipid bilayer electrostatic energy, curvature stress, and assembly of gramicidin channels., Biochemistry, (1997), 5695-701

[26] T. Kimura, W. Jennings & R. M. Epand, Roles of specific lipid species in the cell and their molecular mechanism, Progress in Lipid Research, (2016), 75 - 92

[27] C. Koshy & C. Ziegler, Structural insights into functional lipid-protein interactions in secondary transporters, Biochimica et Biophysica Acta (BBA) - General Subjects, (2015), 476 - 487

[28] M. Kranenburg, C. Laforge & B. Smit, Mesoscopic simulations of phase transitions in lipid bilayers, Phys. Chem. Chem. Phys., (2004), 4531-4534

[29] V. Kiessling, J. Crane & L. K. Tamm, Transbilayer effects of raft-like lipid domains in asymmetric planar bilayers measured by single molecule tracking., Biophys J, (2006), 3313–3326

[30] S. Veatch, I. Polozov, K. Gawrisch & S. L. Keller, Liquid domains in vesicles investigated by NMR and fluorescence microscopy., Biophys J, (2004), 2910-22

[31] G. Chapman, D & Benga, Biomembrane fluidity - studies of model and natural membranes, Biological Membranes, London [u.a.] : Acad. Press, (1984), 1-56

[32] E. Sackmann, Supported membranes: scientific and practical applications., Science, (1996), 43-48

[33] M. Jensen & O. Mouritsen, Lipids do influence protein function-the hydrophobic matching hypothesis revisited., Biochim Biophys Acta, (2004), 205-26

[34] E. Sezgin & P. Schwille, Model membrane platforms to study protein-membrane interactions., Mol Membr Biol, (2012), 144-54

[35] A.-S. Cans, N. Wittenberg, R. Karlsson, L. Sombers, M. Karlsson, O. Orwar & A. Ewing, Artificial cells: Unique insights into exocytosis using liposomes and lipid nanotubes, Proc Natl Acad Sci U S A, (2003), 400–404

[36] S. Aimon, J. Manzi, D. Schmidt, J. A. P. Larrosa, P. Bassereau & G. E. S. Toombes, Functional Reconstitution of a Voltage-Gated Potassium Channel in Giant Unilamellar Vesicles, PLOS ONE, (2011),

[37] D. Tareste, J. Shen, T. J. Melia & J. E. Rothman, SNAREpin/Munc18 promotes adhesion and fusion of large vesicles to giant membranes, Proc Natl Acad Sci U S A, (2008), 2380–2385

[38] G. Maiorano, S. Sabella, B. Sorce, V. Brunetti, M. Malvindi, R. Cingolani & P. P. Pompa, Effects of cell culture media on the dynamic formation of protein-nanoparticle complexes and influence on the cellular response., ACS Nano, (2010), 7481-91

[39] V. Mody, M. Nounou & B. Malavosklish, Novel nanomedicine-based MRI contrast agents for gynecological malignancies., Adv Drug Deliv Rev, (2009), 795-807

[40] M. E. Ali, U. Hashim, S. Mustafa, Y. B. Che Man & K. N. Islam, Gold Nanoparticle Sensor for the Visual Detection of Pork Adulteration in Meatball Formulation, Journal of Nanomaterials, (2012), 7

[41] J. Dobson, Gene therapy progress and prospects: magnetic nanoparticle-based gene delivery., Gene Ther, (2006), 283-7

[42] P. Sharma, S. Brown, G. Walter, S. Santra & B. Moudgil, Nanoparticles for bioimaging, Advances in Colloid and Interface Science, (2006), 471 - 485

[43] N. Praetorius & T. Mandal, Engineered nanoparticles in cancer therapy., Recent Pat Drug Deliv Formul, (2007), 37-51

[44] V. E. Henrich & P. A. Cox, The surface science of metal oxides, Cambridge University Press, Cambridge, U.K., (1994), 464

[45] J. A. Rodríguez & M. Fernández-García, Synthesis, Properties, and Applications of Oxide Nanomaterials, John Wiley & Sons, Inc., (2006), 1-717

[46] C. Burda, X. Chen, R. Narayanan & M. A. El-Sayed, Chemistry and Properties of Nanocrystals of Different Shapes, Chem. Rev., (2005), 1025-1102

[47] M.-C. Daniel & D. Astruc, Gold Nanoparticles: Assembly, Supramolecular Chemistry, Quantum-Size-Related Properties, and Applications toward Biology, Catalysis, and Nanotechnology, Chem. Rev., (2004), 293-346

[48] L. Monticelli, E. Salonen, P. C. Ke & I. Vattulainen, Effects of carbon nanoparticles on lipid membranes: a molecular simulation perspective, Soft Matter, (2009), 4433-4445

[49] G. Rossi & L. Monticelli, Modeling the effect of nano-sized polymer particles on the properties of lipid membranes, Journal of Physics: Condensed Matter, (2014), 503101

[50] R. Chen, P. Choudhary, R. Schurr, P. Bhattacharya, J. M. Brown & P. Ke, Interaction of lipid vesicle with silver nanoparticle-serum albumin protein corona, Applied Physics Letters, (2012), 013703

[51] D. M. Jameson, J. C. Croney & P. D. Moens, Fluorescence: Basic concepts, practical aspects, and some anecdotes, , (2003), 1 – 43

[52] Jablonski, Efficiency of Anti-Stokes Fluorescence in Dyes, Nature, (1933), 839

[53] S. Bradbury & P. Evennett, Contrast Techniques in Light Microscopy (Microscopy Handbooks), Bios Scientific Publishers, (1996), 118

[54] J. R. Lakowicz, Principles of Fluorescence Spectroscopy (Analytical Chemistry), Springer US, (2006), 954

[55] S. Coolidge, H. M. James & R. D. Present, A Study of the Franck-Condon Principle, The Journal of Chemical Physics, (1936), 193-211

[56] P. W. Atkins & R. S. Friedman, Molecular Quantum Mechanics, Oxford University Press, (2010), 592

[57] A. Rondi, Y. Rodriguez, T. Feurer & A. Cannizzo, Solvation-Driven Charge Transfer and Localization in Metal Complexes, Accounts of Chemical Research, (2015), 1432-1440

[58] Y. Shim & H. J. Kim, Vibrational energy relaxation of a diatomic molecule in a room-temperature ionic liquid., J Chem Phys, (2006), 24507

[59] G. Weber & F. J. Farris, Synthesis and spectral properties of a hydrophobic fluorescent probe: 6-propionyl-2-(dimethylamino)naphthalene, Biochemistry, (1979), 3075-3078

[60] S. Sanchez, M. Tricerri, G. Ossato & E. Gratton, Lipid packing determines protein-membrane interactions: challenges for apolipoprotein A-I and high density lipoproteins., Biochim Biophys Acta, (2010), 798(7):1399-408

[61] S. A. Sanchez, M. A. Tricerri & E. Gratton, Laurdan generalized polarization fluctuations measures membrane packing micro-heterogeneity in vivo, Proceedings of the National Academy of Sciences, (2012), 7314-7319

[62] T. Parasassi, G. De Stasio, A. D'Ubaldo & E. Gratton , Phase fluctuation in phospholipid membranes revealed by Laurdan fluorescence., Biophys J, (1990), 1179–1186

[63] E. Sezgin, T. Sadowski & K. Simons, Measuring Lipid Packing of Model and Cellular Membranes with Environment Sensitive Probes, Langmuir, (2014), 8160-8166

[64] T. Parasassi, E. Gratton, W. M. Yu, P. Wilson & M. Levi, Two-photon fluorescence microscopy of laurdan generalized polarization domains in model and natural membranes., Biophys J, (1997), 2413–2429

[65] W. Yu, P. T. So, T. French & E. Gratton, Fluorescence generalized polarization of cell membranes: a two-photon scanning microscopy approach., Biophys J., (1996), 626–636

[66] T. Parasassi & E. Gratton, Membrane lipid domains and dynamics as detected by Laurdan fluorescence, Journal of Fluorescence, (1995), 59-69

[67] J. Sabin, G. Prieto, J. Ruso, P. V. Messina, F. J. Salgado, M. Nogueira, M. Costas & F. Sarmiento, Interactions between DMPC liposomes and the serum blood proteins HSA and IgG., J Phys Chem B, (2009), 1655-61

[68] K. Akabori & J. F. Nagle, Structure of the DMPC lipid bilayer ripple phase, Soft Matter, (2015), 918–926

[69] A. Bangham, M. Standish & J. Watkins, Diffusion of univalent ions across the lamellae of swollen phospholipids. J Mol Biol., (1965), 238-52

[70] S. Matsumoto, M. Kohda & S.-I. Murata, Preparation of lipid vesicles on the basis of a technique for providing W/O/W emulsions, Journal of Colloid and Interface Science, (1977), 149 - 157

[71] Polar Lipids: Preparation of Liposomes, [Brochure], Avanti Polar Lipids, (2016)

[72] Spectrofluorometer: a guide to selecting spectrofluorometer, [Brochure], SLM instruments (1986).

[73] ISS K2 Spectrofluorometer, [Brochure], ISS, Inc. Champaign, IL

[74] A.D. Bangham, Properties and uses of lipid vesicles: an overview., Ann N Y Acad Sci., (1978), 2-7

[75] M. Janiak, D. M. Small & G. G. Shipley, Temperature and compositional dependence of the structure of hydrated dimyristoyl lecithin., J Biol Chem, (1979), 6068-78

[76] R. Lipowsky, The morphology of lipid membranes., Curr Opin Struct Biol., (1995), 531-40

[77] T. Heimburg, Thermal Biophysics of Membranes, (2007)

[78] V. Borenstain & Y. Barenholz, Characterization of liposomes and other lipid assemblies by multiprobe fluorescence polarization., Chem Phys Lipids., (1993), 117-27

[79] L. A. Bagatolli, To see or not to see: Lateral organization of biological membranes and fluorescence microscopy, Biochimica et Biophysica Acta (BBA) - Biomembranes, (2006), 1541 – 1556

[80] E. Perochon, A. Lopez & J. F. Tocanne, Polarity of lipid bilayers. A fluorescence investigation, Biochemistry, (1992), 7672-7682

[81] K. Arnold, A. Lösche & K. Gawrisch, 31P-NMR investigations of phase separation in phosphatidylcholine/phosphatidylethanolamine mixtures, Biochimica et Biophysica Acta (BBA) - Biomembranes, (1981), 143 - 148

[82] E. Carpenter, L. Kamentsky & K. W. Eliceiri, A call for bioimaging software usability, Nature Methods, (2012), 666

[83] C.A. Schneider, W.S. Rasband & K. W. Eliceiri, NIH Image to ImageJ: 25 years of image analysis., Nat Methods, (2012), 671-5

[84] S. J, Arganda-Carreras, E. Frise, V. Kaynig, M. Longair, T. Pietzsch, S. Preibisch, C. Rueden, S. Saalfeld, B. Schmid, J.-Y. Tinevez, D. J. White, V. Hartenstein, K. Eliceiri, P. Tomancak & A. Cardona, Fiji: an open-source platform for biological-image analysis., Nat Methods, (2012), 676-82

[85] K. Eliceiri, M.R. Berthold, I. G. Goldberg, L. Ibanez, B. S. Manjunath, M. E. Martone, R. F. Murphy, H. Peng, A. L. Plant, B. Roysam, N. Stuurman, J. R. Swedlow, P. Tomancak & A. E. Carpenter, Biological imaging software tools., Nat Methods, (2012), 697-710

[86] B. Wang, L. Zhang, S. C. Bae & S. Granick, Nanoparticle-induced surface reconstruction of phospholipid membranes, Proceedings of the National Academy of Sciences, (2008), 18171--18175

[87] P. Leroueil, S. Hong, A. Mecke, J. James, R. Baker, B. G. Orr & M. M. Banaszak Holl, Nanoparticle interaction with biological membranes: does nanotechnology present a Janus face?, Acc Chem Res, (2007), 335-42

[88] P. Leroueil, S. Berry, K. Duthie, G. Han, V. M. Rotello, D. Q. McNerny, J. R. J. Baker, B. G. Orr & M. M. B. Holl, Wide varieties of cationic nanoparticles induce defects in supported lipid bilayers., Nano Lett, (2008), 420-4

[89] Y. Moghadam, W.-C. Hou, C. Corredor, P. Westerhoff & J. D. Posner, Role of Nanoparticle Surface Functionality in the Disruption of Model Cell Membranes, Langmuir, (2012), 16318-16326

[90] Montis, D. Maiolo, I. Alessandri, P. Bergese & D. Berti, Interaction of nanoparticles with lipid membranes: a multiscale perspective, Nanoscale, (2014), 6452-6457

[91] H. E. Toma, V. M. Zamarion, S. H. Toma & K. Araki, The coordination chemistry at gold nanoparticles, Journal of the Brazilian Chemical Society, (2010), 1158 - 1176

[92] D. Ghosh & N. Chattopadhyay, Gold Nanoparticles: Acceptors for Efficient Energy Transfer from the Photoexcited Fluorophores, Optics and Photonics Journal, (2013), 9

[93] Atomic Force Microscope, [Brochure], Bruker Nano

[94] H.-S. Liao, J. Lin, Y. Liu, P. Huang, A. Jin & X. Chen, Self-assembly mechanisms of nanofibers from peptide amphiphiles in solution and on substrate surfaces, Nanoscale, (2016), 14814-14820

[95] K. E. Kirat, S. Morandat & Y. F. Dufrêne, Nanoscale analysis of supported lipid bilayers using atomic force microscopy, Biochimica et Biophysica Acta (BBA) - Biomembranes, (2010), 750 - 765

[96] M.-C. Giocondi, D. Yamamoto, E. Lesniewska, P.-E. Milhiet, T. Ando & C. L. Grimellec, Surface topography of membrane domains, Biochimica et Biophysica Acta (BBA) - Biomembranes, (2010), 703 - 718

[97] J. Lin & A. Alexander-Katz, Cell Membranes Open Doors for Cationic Nanoparticles/Biomolecules: Insights into Uptake Kinetics, ACS Nano, (2013), 10799-10808

[98] F. de Meyer & B. Smit, Effect of cholesterol on the structure of a phospholipid bilayer, Proc Natl Acad Sci U S A, (2009), 3654–3658

[99] A. Kurtz-Chalot, J.-P. Klein, J. Pourchez, D. Boudard, V. Bin, G. B. Alcantara, M. Martini, M. Cottier & V. Forest, Adsorption at cell surface and cellular uptake of silica nanoparticles with different surface chemical functionalizations: impact on cytotoxicity, Journal of Nanoparticle Research, (2014), 2738

[100] D. Walkey, J. B. Olsen, F. Song, R. Liu, H. Guo, D. W. H. Olsen, Y. Cohen, A. Emili & W. C. W. Chan, Protein Corona Fingerprinting Predicts the Cellular Interaction of Gold and Silver Nanoparticles, ACS Nano, (2014), 2439-2455

[101] S. Fenz & K. Sengupta, Giant vesicles as cell models., Integr Biol (Camb), (2012), 982-95

[102] S. Aimon, M. J, D. Schmidt, J. A. Poveda Larrosa, P. Bassereau & G. E. Toombes, Functional reconstitution of a voltage-gated potassium channel in giant unilamellar vesicles., PLoS One, (2011), e25529

[103] M. I. Angelova & D. S. Dimitrov, Liposome electroformation, Faraday Discuss. Chem. Soc., (1986), 303-311

[104] M. I. Angelova, S. Soléau, P. Méléard, F. Faucon & P. Bothorel, Preparation of giant vesicles by external AC electric fields. Kinetics and applications, Progress in Colloid & Polymer Science, (1992), 127-131

[105] Vesicle Prep Pro: First product on the market for automated preparation of solvent free giant unilamellar vesicles, [Brochure], Nanion Technologies

[106] M. Hu, C. Novo, A. Funston, H. Wang, H. Staleva, S. Zou, P. Mulvaney, Y. Xia & G. Hartland, Dark-field microscopy studies of single metal nanoparticles: understanding

the factors that influence the linewidth of the localized surface plasmon resonance., J Mater Chem, (2008), 1949-1960

[107] K. Holthoff & O. Witte, Intrinsic optical signals in rat neocortical slices measured with near-infrared dark-field microscopy reveal changes in extracellular space., J Neurosci, (1996), 2740-9

[108] P. W. Yuen, M.A. Richardson, Introduction to hyperspectral imaging and its application for security, surveillance and target acquisition, Imaging Science Journal, Vol 58, (2010)

[109] E. Gamal & S. Da-Wen, Principles of Hyperspectral Imaging Technology, Hyperspectral Imaging for Food Quality Analysis and Control, (2010), 3 - 43

[110] A. Iqbal, D.W. Sun & P. Allen, An overview on principle, techniques and application of hyperspectral imaging with special reference to ham quality evaluation and control, Food Control, (2014), 242 - 254

[111] Hyperspectral User Manual, [Brochure], CytoViva, (2011)

[112] ENVI: Image analysis software of choice for image scientists, [Brochure], Harris Geospatial, (2016)

[113] E. Smith, W. Wang & P. K. Dea, Effects of cholesterol on phospholipid membranes: inhibition of the interdigitated gel phase of F-DPPC and F-DPPC/DPPC., Chem Phys Lipids, (2012), 151-9

[114] B. Olsen, A. Bielska, T. Lee, M. D. Daily, D. F. Covey, P. H. Schlesinger, N. A. Baker & D. S. Ory, The structural basis of cholesterol accessibility in membranes., Biophys J., (2013), 1838-47

[115] S. Yesylevskyy & A.P. Demchenko, Cholesterol behavior in asymmetric lipid bilayers: insights from molecular dynamics simulations., Methods Mol Biol., (2015), 291-306

[116] F. Tavanti, A. Pedone & M. C. Menziani, Competitive Binding of Proteins to Gold Nanoparticles Disclosed by Molecular Dynamics Simulations, The Journal of Physical Chemistry C, (2015), 22172-22180

[117] N. Duran, C. Silveira, M. Duràn & D. Martinez, Silver nanoparticle protein corona and toxicity: A mini-review, Journal of Nanobiotechnology, (2015), s12951-015-0114-4

[118] K. Simons & E. Ikonen, Functional rafts in cell membranes., Nature, (1997), 569-72

[119] C. Montis, D. Maiolo, I. Alessandri, P. Bergese & D. Berti, Interaction of Nanoparticles with Lipid Membranes: A Multiscale Perspective, Nanoscale, (2014), 6, 6452–6457